

國立交通大學

機械工程學系

博士論文

質子交換膜燃料電池中傳輸現象效應對性能影響之研究

Investigation of the Effects of Transport Phenomena on the
Performance of Proton Exchange Membrane Fuel Cells



研究生：江木勝
指導教授：陳俊勳教授
 曲新生教授

中華民國九十六年五月

質子交換膜燃料電池中傳輸現象效應對性能影響之研究

Investigation of the Effects of Transport Phenomena on the Performance of Proton Exchange Membrane Fuel Cells

研究生：江木勝

Student : Mu-Sheng Chiang

指導教授：陳俊勳教授

Advisor : Chiun-Hsun Chen

曲新生教授

Hsin-Seng Chu

國立交通大學

機械工程學系

博士論文

A Thesis

Submitted to Department of Mechanical Engineering
College of Engineering
National Chiao Tung University
in partial Fulfillment of the Requirements
for the Degree of
Doctor of Philosophy
in

Mechanical Engineering

May 2006

Hsinchu, Taiwan, Republic of China

中華民國九十六年五月

質子交換膜燃料電池中傳輸現象效應對性能影響之研究

學生：江木勝

指導教授：陳俊勳 曲新生

國立交通大學

機械工程系

摘要

本論文探討質子交換膜燃料電池於各種傳輸元件設計與水熱操作模式下的傳輸現象與性能影響。研究中首先建置描述質子交換膜燃料電池內部各種傳輸及電化學現象之數學模式，其中以質量、物種、動量與電流守恆方程式做為模式主要架構。在電化學反應部份以 Butler-Volmer 方程式加以描述，方程式使用活化過電位聯繫觸媒層中電子相與質子相電位，為反應的主要驅動力。為考慮電化學反應所產生熱能，模式中同時納入系統能量守恆方程式，其中焓值源項考慮電流焦耳熱、過電位以及水之相變化潛熱。本研究中含蓋三個質子交換膜燃料電池傳輸現象與電化學反應之主要議題，分別為溫溼度梯度、傳輸元件效應以及新型陰極流道設計對性能影響之研究。

在探討各式加濕與溫度梯度的影響時，數值計算結果以極化曲線與局部性質分佈說明各種加濕與溫度梯度效應。結果顯示陰陽極加溼溫度變化對電池性能產生不同效果。而在溫度梯度效應方面，依據梯度大小與梯度方向亦有不同的現象表現。在任一較高的邊界溫度下，由於觸媒反應速率及薄膜導電度的提升，電池性能隨另一邊界溫度之增加而提升。從局部氣體濃度及液態水分佈情況繪圖中，顯示出其與溫度及加濕梯度具有密切關係，進而對電池性能產生影響。

於傳輸元件設計效應之研究中，藉由改變各種流道高寬比與氣體擴散層厚度的分析結果顯示，細高型的流道設計適合於中電流密度的電池操作情況，而寬扁型的流道則於高電流密度下有較佳的性能輸出。經由特定位置橫向氧氣濃度與

相電位圖形顯示在燃料電池中的氧氣傳輸與電子傳導對局部電化學反應呈現競爭效應，其相對強度與操作條件與位置有關係。於電池極化曲線中顯示最佳氣體擴散層厚度隨操作電壓減少而增大；然而在最小的考慮電壓 0.14V 時，由於液態水的累積與傳輸路徑增長而逆轉此一趨勢。

本論文第三部份針對一具新型陰極流道燃料電池之電化學反應與性能進行探討。藉由流道出口寬度改變，而考量漸擴、直管與漸縮等三種外型流道的效應。研究結果顯示漸縮型流道於中電池電壓情況下，由於其具有增進電子傳輸之效果而有較佳性能表現。反之，當電池操作電壓下降反應速率提升時，漸擴型流道因為可以提供較高濃度氧氣至觸媒層反應位址，致使其產生較大電流輸出。藉由檢視觸媒層中局部電流密度與氧氣及各項電位分佈情形，可以獲得燃料電池中內部電化學反應的變化趨勢。此一結果可以使我們從一般所熟知的整體性能曲線變化機制中，進一步了解電池內部由於各種物種傳輸現象特性差異，所產生反應主導機制不同的原因，對於研發者及工程師具有重要幫助。

Investigation of the Effects of Transport Phenomena on the Performance of Proton Exchange Membrane Fuel Cells

**Student: Mu-Sheng Chiang Advisor: Chiun-Hsun Chen
Hsin-Seng Chu**

**Department of Mechanical Engineering
National Chiao Tung University**

ABSTRACT

This dissertation presents a numerical investigation of the transport phenomena and performance of proton exchange membrane fuel cell (PEMFCs) with various transport component design parameters as well as water and thermal management schemes. A three-dimensional fuel cell model, incorporating conservations of species, momentum, as well as current transport, is developed at first. The Butler-Volmer equation that describes the electrochemical reaction in the catalyst layer is adopted with the activation overpotential as the connection between the solid phase potential and that of the electrolyte phase. To ensure the conservation of enthalpy, the energy equation is employed to the model domain with three sources of enthalpy generation: ohmic heating, activation overpotential as well as phase change of water harnessed in modeling. Three major topics concerning the transport phenomena as well as electrochemical reaction in PEMFCs are presented in this dissertation. This includes the water and thermal management, transport component design effect as well as a novel cathode channel shape effect.

In the investigation of cell temperature and humidification effects, numerical prediction results are presented using polarization curves and contour plots. Findings show that humidification level perturbation on the anode or cathode side creates an individual effect. Mechanisms influencing performance variation tendencies are interpreted. Also, modeling results with existing temperature gradient exhibit different

trends on the overpotentials according to the slop and magnitude. At a higher boundary temperature on either side, cell performance increases according to the temperature increase on the other side because the reaction kinetic and ionic phase conductivity is promoted. Contour plots of local concentration and saturation level show the close relation between the existence of both temperature and humidification gradients and the local properties variations.

Through cell performance simulation with various channel aspect ratios and gas diffusion layer (GDL) thicknesses, a slender channel is found suitable for cells operating at moderate reaction rate, and a flat channel produces more current at low cell voltage. Plots of transverse oxygen concentration and phase potential variation indicate that these oppositely affect the local current density pattern. The relative strengths of these two factors depend on the transport component position and geometry, as well as on the cell operating conditions. Consequently, the curves of cell output current density demonstrate that the optimal GDL thickness increases as the cell voltage decreases. However, at the lowest considered cell voltage of 0.14V, optimal thickness decreases as that of a thick GDL the oxygen deficiency caused by long traveling length and clogging effect of liquid water reverses this relationship.

The electrochemical reaction and performance of PEMFCs with a novel cathode channel shape is proposed in the third part of this dissertation. This channel geometry has a characteristic of continuous variation of shoulder/channel ratio along the main stream direction. Three types of channel configurations: convergent, straight and divergent channels are investigated. The calculation results demonstrate the effects of the channel configuration on the transport phenomena and cell reaction. As the cell operates at a medium cell voltage, the convergent channel behaves better because the electrons transport is enhanced and the corresponding ohmic overpotential is small.

On the contrary, the divergent shape channel performs better at higher reaction rate as it is able to deliver sufficient oxygen concentration to the reaction sites. Through the distribution inspections of the local current density, oxygen concentration and potential fields in the catalyst layer, variation trend of the electrochemical reaction in the fuel cell is available. With the knowledge of the well comprehended determining reasons of global performance variation, these results can further offer the explanations, which are of great important to the researchers and engineers, of the different dominant mechanisms resulting from the characteristic differentials of transport phenomena for the various species inside the fuel cell.



致 謝

本論文得以完成，首先感謝指導老師曲新生教授與陳俊勳教授悉心指導，兩位老師嚴謹治學態度與諄諄教誨使學生在專業領域、學術論文寫作與問題釋疑方面，獲得莫大的助益。同時也感謝台南成功大學陳朝光國家講座教授多年來的教導，陳老師高瞻遠矚，學術淵博，對於學生循循善誘，暮鼓晨鐘，猶似醍醐灌頂，如沐春風。

感謝口試委員翁政義校長、陳發林教授、林清發教授與顏維謀校長於審閱論文時所提指正與寶貴建議，以及諸位老師獨到見解，使得本論文更臻完備。同時感謝電物所簡贖瑞博士在研究方向與文稿撰寫上的協助。

在學期間，熱物理研究室的成員，特別是旭昉、世國、鵬樟、建興、時明、孝彥、建評、純怡、清益以及諸多畢業學長與碩班學弟們在課業切磋與研究生活上也提供了許多幫助。

最後，對於撫育我的父母親、關心我之所有親友，特別是岳母的祝福與愛妻遊兒多年來無怨無悔始終如一的付出，予宛諭、宛庭及家庭無微不至的照顧，使研究生生活無後顧之憂，致上最高的敬意與謝意，謹將此這份的來不易的成果與榮耀與大家一起分享。

TABLE OF CONTENTS

ABSTRACT (in Chinese)	i
ABSTRACT (in English)	iii
ACKNOWLEDGEMENT	vi
TABLE OF CONTENTS	vii
LIST OF TABLES	xi
LIST OF FIGURES	xii
NOMENCLATURE	xix
CHAPTER 1 INTRODUCTION	1
1.1 Background.....	1
1.1.1 Operating Principles of PEMFCs.....	1
1.1.2 Transport Phenomena and Cell Reaction in PEMFCs.....	2
1.2 Literature Survey.....	4
1.2.1 Modeling Development and Water/Thermal Management Investigation.....	4
1.2.2 Investigation of Cell Component Design.....	5
1.2.3 Numerical Method Development.....	9
1.3 Objectives.....	10
1.4 Outlines.....	10
CHAPTER 2 MATHEMATICAL MODELING	16
2.1 Model Description.....	17
2.2 Basic Assumptions.....	17
2.3 Governing Equations.....	18
2.3.1 Continuity Equation.....	19
2.3.2 Momentum Equation.....	19

2.3.3	Mass Transport.....	20
2.3.4	Electrochemical Reaction.....	21
2.3.5	Potential Fields.....	22
2.3.6	Liquid Water Transport.....	24
2.3.7	Energy Equation.....	26
2.4	Boundary Conditions.....	27
2.4.1	Flow Field Boundary Conditions.....	27
2.4.2	Potential Field Boundary Conditions.....	27
2.5	Method of Solution.....	29
2.4.3	Calculation Procedure.....	29
2.4.4	Model Validation.....	29

CHAPTER 3 EFFECTS OF TEMPERATURE AND HUMIDIFICATION LEVELS ON THE PERFORMANCE OF PROTON EXCHANGE MEMBRANE FUEL CELLS.....

3.1	Introduction.....	37
3.2	Effects of Humidification Scheme.....	38
3.2.1	Enhanced Humidification Scenario.....	38
3.2.2	Reduced Humidification Scenario.....	40
3.2.3	Combined Enhanced and Reduced Humidification Scenario.....	41
3.3	Effects of Cell Temperature Gradient.....	42
3.3.1	Cell Performance at Higher Cathode Temperature.....	42
3.3.2	Cell Performance at Higher Anode Temperature.....	43
3.3.3	Cell Performance at Lower Anode Temperature.....	43
3.4	Local Distribution of Model Variables.....	44

3.4.1	Temperature Field.....	45
3.4.2	Oxygen Concentration Distribution.....	45
3.4.3	Water Saturation Level.....	46
3.5	Tendency Comparisons between Predicted and Other Experimental Results.....	46
3.6	Summary.....	48
 CHAPTER 4 TRANSPORT COMPONENT DESIGN EFFECTS ON PROTON EXCHANGE MEMBRANE FUEL CELL PERFORAMNCE		
		66
4.1	Introduction.....	66
4.2	Cell Performance Subjected to Transport Component Design.....	66
4.2.1	Effect of Channel Aspect Ratio.....	67
4.2.2	Effect of Diffusion Layer Thickness.....	67
4.3	Local Properties Variations in Transverse Direction.....	69
4.3.1	Membrane Conductivity and Potential.....	69
4.3.2	Solid Phase Potential and Activation Overpotential.....	71
4.3.3	Water Saturation Level.....	73
4.3.4	Oxygen Concentration and Current Density.....	74
4.4	Vertical Distribution of Velocity and Oxygen Concentration.....	79
4.5	Effect of Operating Temperature.....	80
4.6	Tendency Comparisons with Previous Works from Literature.....	82
4.7	Summary.....	83
 CHAPTER 5 ELECTROCHEMICAL REACTION AND PERFORMANCE OF PROTON EXCHANGE MEMBRANE FUEL CELLS WITH NOVEL CATHODE		

FLOW CHANNEL SHAPE.....	112
5.1 Introduction.....	112
5.2 Model Properties Distributions.....	114
5.2.1 Oxygen Concentration.....	114
5.2.2 Water Saturation Level.....	115
5.2.3 Potential Fields and Activation Overpotential.....	116
5.3 Local Catalyst Reaction Rate.....	119
5.4 Cell Performance for Channel Design with Various S/C Ratios.....	122
5.5 Effect of Reactant Stoichiometry on Cell Performance.....	123
5.6 Summary.....	124
CHAPTER 6 CONCLUSIONS AND FUTURE PERSPECTIVES	146
6.1 Concluding Remarks.....	146
6.2 Future Perspectives.....	150
REFERENCES.....	152
APPENDIX A.....	158



LIST OF TABLES

Table 2.1 Cell geometries and operating conditions of base model.....	31
Table 2.2 Electrochemical parameters and transport properties.....	32
Table 2.3 Results of three computation grid systems based on the parameters in Table 2.1 and Table 2.2.....	33
Table 4.1 Channel and shoulder geometries for various ARs (unit: mm).....	86
Table 5.1 Main cell parameters, properties and operating conditions.....	127
Table 5.2 Simulation cases for various channel configurations used in this study.....	128



LIST OF FIGURES

Fig. 1.1. Operating principle of a single PEMFC.....	12
Fig. 1.2. Basic components of a single PEMFC.....	13
Fig. 1.3. The dominant mechanisms of cell performance.....	14
Fig. 1.4. Various overpotentials and available potential in fuel cells.....	15
Fig. 2.1. Physical and computational domains considered in this study.....	34
Fig. 2.2. Numerical flow chart of current study.....	35
Fig. 2.3 Comparison of current model results with Wang <i>et al.</i> at 323K and 343K.....	36
Fig. 3.1. Effect of anode enhanced humidification scheme with 10K of anode humidification level greater than cell temperature for cell temperatures 333K, 343K and 353K.....	50
Fig. 3.2. Effect of cathode enhanced humidification scheme with 10K of cathode humidification level greater than cell temperature for cell temperatures 333K, 343K and 353K.....	51
Fig. 3.3. Effect of anode reduced humidification scheme with 10K of anode humidification level smaller than cell temperature for cell temperatures 333K, 343K and 353K.....	52
Fig. 3.4. Effect of cathode reduced humidification scheme with 10K of cathode humidification level smaller than cell temperature for cell temperatures 333K, 343K and 353K.....	53
Fig. 3.5. Effect of humidification gradient that combines anode reduced and cathode enhanced schemes for cell temperatures 333K, 343K and	

353K.....	54
Fig. 3.6. Cell performance at various total overpotentials with 353K cathode temperatures and anode temperatures varied from 333K to 353K.....	55
Fig. 3.7. Ionic Phase conductivity along central channel direction on membrane middle section for cases in Fig. 3.6.....	56
Fig. 3.8. Cell performance at various total overpotentials with 353K anode temperatures and cathode temperatures varied from 333K to 353K.....	57
Fig. 3.9. Cell performance at various total overpotentials with 333K anode temperatures and cathode temperatures varied from 333K to 353K	55
Fig. 3.10(a). Ionic phase conductivity along central channel direction on membrane middle section for cases in Fig. 3.9 at total cell overpotential of 0.6V.....	59
Fig. 3.10(b). Ionic phase conductivity along central channel direction on membrane middle section for cases in Fig. 3.9 at total cell overpotential of 0.98V.....	60
Fig. 3.11. Local temperature contours in cathode GDL at section of $x=0.025m$ with 353K anode temperatures and cathode temperatures (a) 343K (b) 333K.....	61
Fig. 3.12. Local oxygen mass fractions in cathode GDL at section of $x=0.025m$ with 353K anode temperatures and cathode temperatures (a) 343K (b) 333K.....	62
Fig. 3.13. Local water saturation in cathode GDL at section of $x=0.025m$	

with 353K anode temperatures and cathode temperatures (a) 343K (b) 333K.....	63
Fig. 3.14 Experimental results of Wang <i>et al.</i> (2003) on the effects of cathode humidification schemes. The cell temperature is set at 343K and the cathode humidification temperatures varied from 313K to 353K.....	64
Fig. 3.15 Experimental results of Lee <i>et al.</i> (1999b) on the effects of anode and cathode enhanced humidification schemes. The cathode humidification temperatures vary from 348K to 358K while the anode humidification temperatures vary from 358K to 368K.....	65
Fig. 4.1(a) Current density distribution at various cell voltages as function of AR.....	87
Fig. 4.1(b) Current density distribution at various cell voltages as function of GDL thickness.....	88
Fig. 4.2(a) Distributions of potential and conductivity of membrane in the transverse direction of the middle X-Y plane for three values of AR at cell voltages of 0.62V.....	89
Fig. 4.2(b) Distributions of potential and conductivity of membrane in the transverse direction of the middle X-Y plane for three values of AR at cell voltages of 0.14V.....	90
Fig. 4.3(a). Distributions of potential and conductivity of membrane in the transverse direction of the middle X-Y plane for three values of GDL thickness at cell voltage of 0.62V.....	91
Fig. 4.3(b). Distributions of potential and conductivity of membrane in the transverse direction of the middle X-Y plane for three values of	

GDL thickness at cell voltage of 0.14V	92
Fig. 4.4 (a). Transverse distributions of solid phase potential and activation overpotential at the interface between the cathode catalyst layer and the GDL for three values of AR at cell voltage of 0.62V	93
Fig. 4.4 (b). Transverse distributions of solid phase potential and activation overpotential at the interface between the cathode catalyst layer and the GDL for three values of AR at cell voltage of 0.14V	94
Fig. 4.5 (a). Transverse distributions of solid phase potential and activation overpotential at the interface between the cathode catalyst layer and the GDL for three GDL thicknesses at cell voltage of 0.62V	95
Fig. 4.5(b). Transverse distributions of solid phase potential and activation overpotential at the interface between the cathode catalyst layer and the GDL for three GDL thicknesses at cell voltage of 0.14V	96
Fig. 4.6(a). Effect of channel aspect ratio on transverse water saturation of the cathode GDL along channel direction at cell voltage of 0.62V	97
Fig. 4.6(b). Effect of channel aspect ratio on transverse water saturation of the cathode GDL along channel direction at cell voltage of 0.14V	98
Fig. 4.7(a). Effect of GDL thickness on transverse water saturation of the cathode GDL along channel direction at cell voltage of 0.62V	99
Fig. 4.7(b). Effect of GDL thickness on transverse water saturation of the cathode GDL along channel direction at cell voltage of 0.14V	100
Fig. 4.8(a). Transverse distributions of oxygen mass fraction and local current density at the interface between the cathode catalyst layer and the GDL for three values of AR at cell voltage of 0.62V	101
Fig. 4.8(b). Transverse distributions of oxygen mass fraction and local current	

density at the interface between the cathode catalyst layer and the GDL for three values of AR at cell voltage of 0.14V.....	102
Fig. 4.9(a). Transverse distributions of oxygen mass fraction and current density at the interface between the cathode catalyst layer and the GDL for three GDL thicknesses at cell voltage of 0.62V.....	103
Fig. 4.9(b). Transverse distributions of oxygen mass fraction and current density at the interface between the cathode catalyst layer and the GDL for three GDL thicknesses at cell voltage of 0.14V.....	104
Fig. 4.10(a). Vertical distributions of fluid velocity and oxygen mass fraction in cathode channel and GDL for AR value of 0.5.....	105
Fig. 4.10(b). Vertical distributions of fluid velocity and oxygen mass fraction in cathode channel and GDL for AR value of 1.5.....	106
Fig. 4.11(a). Vertical distributions of fluid velocity and oxygen mass fraction in cathode channel and GDL for GDL thickness of 152 micro m....	107
Fig. 4.11(b). Vertical distributions of fluid velocity and oxygen mass fraction in cathode channel and GDL for GDL thickness of 356 micro m....	108
Fig. 4.12. Effects of operating temperature on cell performance at various values of AR.....	109
Fig. 4.13 Effects of operating temperature on cell performance at various values of GDL thickness.....	110
Fig. 4.14 Experimental results of Lee et. al. (1999a) on the effect of compression force on cell performance.....	111
Figure 5.1 (a) Computational Domain (b) Cathode Channel Configuration.....	129
Figure 5.2 (a) Oxygen mass fraction contours at cell voltage of 0.62V for outlet port S/C values of 0.67, 1 and 1.5.....	130

Figure 5.2 (b) Oxygen mass fraction contours at cell voltage of 0.22V for outlet port S/C values of 0.67, 1 and 1.5.....	131
Figure 5.3 (a) Liquid water saturation contours at cell voltage of 0.62V for outlet port S/C values of 0.67, 1 and 1.5.....	132
Figure 5.3 (b) Liquid water saturation contours at cell voltage of (a) 0.62V (b) 0.22V for outlet port S/C values of 0.67, 1 and 1.5.....	133
Figure 5.4 (a) Solid and membrane phase potential contours at cell voltage of 0.62V for straight channel.....	134
Figure 5.4 (b) Solid and membrane phase potential contours at cell voltage of 0.22V for straight channel.....	135
Figure 5.5 (a) Activation overpotential contours at cell voltage of 0.62V for outlet port S/C values of 0.67, 1 and 1.5.....	136
Figure 5.5 (b) Activation overpotential contours at cell voltage of 0.22V for outlet port S/C values of 0.67, 1 and 1.5.....	137
Figure 5.6 (a) Current density contours at cell voltage of 0.62V for outlet port S/C values of 0.67, 1 and 1.5.....	138
Figure 5.6 (b) Current density contours at cell voltage of 0.22V for outlet port S/C values of 0.67, 1 and 1.5.....	139
Figure 5.7 (a) Transverse oxygen mass fraction and current density at $x=0.012\text{m}$ of CL middle plane with cell voltage of 0.62V and S/C values of 0.67, 1.50.....	140
Figure 5.7 (b) Transverse oxygen mass fraction and current density at $x=0.048\text{m}$ of CL middle plane with cell voltage of 0.62V and S/C values of 0.67, 1.50.....	141
Figure 5.8 (a) Transverse oxygen mass fraction and current density at	

<p>x=0.012m of CL middle plane with cell voltage of 0.22V and S/C values of 0.67, 1.50.....</p> <p>Figure 5.8 (b) Transverse oxygen mass fraction and current density at x=0.048m of CL middle plane with cell voltage of 0.22V and S/C values of 0.67, 1.50.....</p> <p>Figure 5.9 Comparison of cell performance for various cathode channel geometry designs.....</p> <p>Figure 5.10 Effect of reactant stoichiometry on cell current density at operating voltages of 0.22V and 0.62V for three cathode channel configurations.....</p>	<p>142</p> <p>143</p> <p>144</p> <p>145</p>
---	---



NOMENCLATURE

C	form drag constant
c	molar concentration, mole m ⁻³
D	diffusivity, m ² sec ⁻¹
F	Faraday constant, 96500 C mole ⁻¹
g	gravitational acceleration, m sec ⁻²
H	height, m
i	current density, A m ⁻²
K	permeability, m ²
k	relative permeability
L	length, m
M	molecular weight, kg mol ⁻¹
m	catalyst loading, mg m ⁻²
n	number of species
P	pressure, Pa
q	number of electron transferred
r	rate constant
R	universal constant, 8.314 J mole ⁻¹ K ⁻¹
s	saturation level
S	source term
T	temperature, K
U	vector form of mixture velocity, m sec ⁻¹
u	scalar form of mixture velocity, m sec ⁻¹
V	Voltage, V
v	pore volume of porous medium, m ³



w mass fraction of species
W width of domain, m
x molar fraction
y switching function

Greek symbols

β transfer coefficient
 δ tortuosity
 ε dry porosity
 ϕ potential, V
 φ concentration dependence
 η overpotential, V
 μ dynamic viscosity, N sec m⁻²
 ν kinematic viscosity, m² sec⁻¹
 γ water content in membrane
 θ contact angle
 σ electric conductivity, S m⁻¹
 ζ surface tension, N m⁻¹
 ξ stoichiometry of hydrogen or oxygen



Superscripts

eff effective value

c capillary

Subscripts

a anodic

c cathodic

cat catalyst

cel cell

cha channel

con condensation

eva evaporation

F Forchheimer term

g gaseous phase

j volumetric transfer current density

k anode or cathode

l liquid phase

m momentum

mas per unit mass of carbon supported catalyst particle

mem membrane phase

p index for phases

plt platinum

s species

sat saturation

sol solid phase

v per unit volume



- w water
- x x component
- y y component
- z z component
- α index for species



CHAPTER 1

INTRODUCTION

1.1 Background

Fuel cell system directly converts chemical energy of fuel into electrical power. Unlike the traditional internal combustion engine, it releases the energy through an electrochemical reaction with the advantages of quietness, high efficiency, low emission, and simplicity. Given these characteristics, it is likely to substitute current power transformation methods which are facing the series problems of fossil oil shortage and global climate change. The proton exchange membrane fuel cells (PEMFCs), using solid polymers as working ions passages, have recently received much attention and intensive study as a promising candidate on the applications of vehicles, 3C equipments and other movable or stationary power systems. (Spiegel *et al.*, 1999; Barbir, 2005; Sammes, 2006).

1.1.1 Operating Principles of PEMFCs

During the fuel cell power conversion process, chemical energy stored in the bounded atom electronic orbits is liberated and converged into electrical energy through electro-catalytic activity of catalysts in the electrodes. Catalysts

macroscopically liberate electrons of hydrogen molecules which are converted into protons simultaneously at the anode. As shown in Fig. 1.1, these two charged species are transported through individual gateways by electric field functions and other mechanisms. The electrons move along the external circuit and release electrical energy through potential drop on the loading. Protons transport is driven by a set of more complicated factors. The proton exchange membrane must be hydrated for ion movement facilitation. It uses polytetrafluoroethylene (PTFE) as the structure backbone and sulfonic acid side chains for the ion conduction purpose. Although proton movement in the membrane is not well understood, suitable membrane water content is beneficial (Nguyen and White, 1993). Additionally, with polar molecular property, water is also carried by protons and moved from the anode to cathode during cell operation. Concentration and pressure gradients through the membrane also have a degree of influences on water transport. Water is produced in the cathode catalyst layer due to cell reaction and, with the aforementioned effects, may lead to a flooding problem and dramatically reduce cell performance at high current density. A typical unit cell structure is drawn in Fig. 1.2.

1.1.2 Transport Phenomena and Cell Reaction in PEMFCs

PEMFC performance is dictated by factors such as transport component geometry and morphology, and operating conditions. The energy conversion

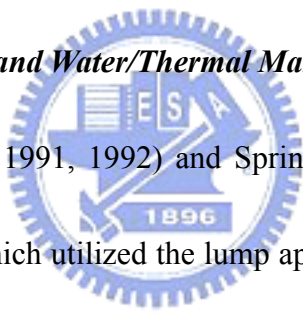
processes in the PEMFC involve multiphase, multi-component flow, and heat and mass transfer in porous media with electrochemical reactions. Reactants are delivered and distributed evenly by grooved flow channels on bipolar plates. Despite the simple geometry of flow channels, the actual flow field is intrinsically three-dimensional that contains longitudinal, transverse, and through plane directions. The cathode catalyst layer serves as oxygen sink as well as water source. The most challenging aspect of modeling the fuel cell transport phenomena is that these processes are coupled with complex electrochemical reactions.

When fuel cell delivering current and electrical energy, the associate energy losses, or sometimes called overpotentials are unavoidable and require further investigation. There are three main sources of energy losses; they are electrode kinetics loss, ohmic loss and mass transport loss. When the reaction rate is slow, the polarization curve is dominated by the electrode kinetics loss. However, as the current density increases, the dominant mechanism of cell performance shifts from ohmic loss to mass concentration loss as shown in Fig. 1.3. From another viewpoint, the ohmic losses are mainly originated from the currents of electron and proton at their individual passages, as depicted in Fig. 1.4. The difference between the two phase potentials in catalyst layer is called activation overpotential, which is the driving force of the electrode reaction. The available cell potential is then the net value of open

circuit voltage minus the summation of these losses. Therefore, when the total overpotential in the cell domain increases, the driving force for fuel cell reaction also increases and more electric current is produced. However, the remaining cell voltage to drive outer electric loading decreases. To obtain a high performance characteristic of the PEMFCs, the quest of the involved correlation among various design parameter as well as operating conditions has long been the major subject of the researchers.

1.2 Literature Survey

1.2.1 Modeling Development and Water/Thermal Management Investigation



Bernardi *et al.* (1990, 1991, 1992) and Springer *et al.* (1991) pioneered the study of PEMFC modeling which utilized the lump approach and conservation theory to develop unidirectional models through electrodes and membrane assuming isothermal condition. The Bernardi's model (1990) suggested reactant gas humidification tuning to accommodate changing cell demands for water. Fuller *et al.* (1993) considered a two-dimensional membrane-electrode assembly and examined the water, thermal management in PEMFC. Membrane water concentration and gas channel temperature were calculated for different heat transfer coefficients. Findings showed that a lower heat transfer coefficient is responsible for membrane dehydration, and substantial cell performance decrease. Yi *et al.* (1998) developed an

along-the-channel, two-dimensional model including various thermal management schemes. Their model results showed that the heat exchanger design with counter flow is more effective than co-flow and constant bulk temperature schemes. Besides these works, the Row *et al.* model (2001) included variable membrane hydration and water phase change in the electrodes. Baschuk *et al.* (2000) investigated variable degree effect of water flooding in the cathode catalyst layer and/or cathode electrode backing region on cell performance. Simpalee *et al.* (2000) formulated a comprehensive three-dimensional model to predict temperature distribution inside a straight channel PEMFC, and presented a group of source terms facilitating commercial software application. Djilali *et al.* (2000) analyzed transport phenomena in a PEMFC assessing non-isothermal and non-isobaric effects. Furthermore, numerical results of Ju *et al.* (2005) with a single-phase and non-isothermal model revealed that temperature rise within the cell could be as high as 13.75K at medium reaction rate under certain conditions. The recent study of Wang *et al.* (2006) revealed that a new heat removal mechanism resembling the heat pipe exists in the electrode.

1.2.2 Investigation of Cell Component Design

On the studied of the component designs, Giorgi *et al.* (1998) investigated diffusion layer porosity influence on effective catalyst activity for the cathode reduction reaction. Thickness and diffusion layer structure effects on low Pt-loading

electrode performance for PEMFC were also conducted experimentally. An optimal thickness of diffusion layer was found due to its lower electrical resistance. Decreased performance with the thickest diffusion layer was attributed to a long reactant transport passage and to the flooding problem. Jordan *et al.* (2000) reported the carbon support and electrode loading effects on PEMFC performance. Various parameter impacts, such as diffusion layer thickness, PTFE content and morphology, as well as operating temperature and humidification condition on cell performance were addressed. Lee *et al.* (1999a) asserted from experimental results that an optimal bore torque was obtained for a soft commercial diffusion layer because of porosity and electrical contact resistance changes. Their results also revealed that a cell with high bore torque corresponding to a thin diffusion layer generates more current at a moderate reaction rate, and a moderate bore torque performs better at a high reaction rate for this kind of diffusion layer.

Several elaborate mathematical models were developed to provide qualitative insights into the transport phenomena in a PEMFC, besides the experimental works. He *et al.* (2000) presented a two-dimensional, two-phase, multi-component transport model investigating gas and liquid water hydrodynamic effects on PEMFC performance employing an inter-digitated flow field. Parametric study on electrode thickness effect indicated that within an electrode finite thickness, average current

density increases monotonically with electrode thickness increase, no matter what the operating voltage. Furthermore, beyond this finite thickness, cell performance decreases. This phenomenon was explained by reactant transport and liquid water removal viewpoints. The effects of channel and shoulder width ratio (C/S ratio) revealed that cell performance enhances with a greater C/S ratio. Natarajan *et al.* (2001) proposed a half-cell, transient model for the cathode using the conventional flow field to evaluate design parameter influences on fuel cell transport processes. Contrary to He *et al.* (2000), they found, as diffusion layer thickness decreases at lower cathode overpotential, the reactant transport is not affected by the liquid water and at some diffusion layer thickness, current density loss at the shoulder region outweighs channel region gain, leading to an optimum diffusion layer thickness. However, a thinner diffusion layer thickness results in better performance and an optimum thickness does not exist at a higher reaction rate.

In the two-dimensional half-cell model performed by West *et al.* (1996), effects of rib sizing and geometry of GDL on current and water distributions within the cell were reported. Special attention was given to the relation between rib width and water content in the membrane. Kulikovsky *et al.* (1999) conducted the parametric studies with high and low values of solid phase electrode conductivity elucidating the possibility of locally reducing catalyst loading in the catalyst layer.

Their study concluded that at low solid phase conductivity, cell reaction concentrates mainly at the rib region catalyst layer and the catalyst can be removed from the channel region catalyst layer with little impact on total cell performance. Simplified descriptions of the kinetic and mass transport model developed from Jeng *et al.* (2004) concluded that GDL effectiveness decreases with reaction rate and increases with flow channel width. Also, when GDL porosity is low, cell performance decreases with an increase in GDL thickness. Sun *et al.* (2005a, 2005b) conducted a series of investigations on catalyst layer structural parameter influences with an improved cross-the-channel model. Various design and operating factors such as C/S ratio, orthotropic GDL conductivity, and electrode compression effects were investigated in the model while charge transfer and oxygen diffusion were simultaneously taken into account. Gas and electron transport plays an essential role in cathode performance in that both electric conductivity and GDL thickness could be vital parameters for transport component optimal design, as conclusions indicated.

Recently, Yan and co-workers (Yan *et al.* 2004; 2005; Liu *et al.* 2005; 2006) investigated various vital issues of the PEMFCs, including the water and thermal management in PEM, transient behaviors of reactant transport, baffle-blocked channel and channel design with tapered configuration. The conclusions in the study of flow channel design effects on steady or dynamic behaviors showed that a faster dynamic

response and better performance can be reached by a larger channel depth ratio. Moreover, a new flow field with baffles in the tandem array was proposed to enhance the reactant transport and cell performance. The beneficial effects of the presence of baffles are notable with the increase of width and/or number of baffles in the tandem array. The simulation work of a tapered flow channel design revealed that the cell performance can be noticeably promoted with the fuel channel tapered at a higher reaction rate. Meanwhile, under this operating condition, the influence of liquid water on the cell performance is significant.

1.2.3 Numerical Method Development

With the fast development of the hardware and software of microcomputers, most groups researching cell performance simulation have recently begun to apply commercial computational fluid dynamics (CFD) algorithms in their study with integration of several conjugate problems such as potential fields, electrochemical reaction and two-phase flow. Hence, a more rigorous three-dimensional simulation has been made possible for investigating the complex transport phenomena. The species and properties in the physical domain can be described in greater detail, and the numerical results are more reliable than one- or two-dimensional models (Dutta *et al.*, 2000; Dutta *et al.*, 2001; Berning *et al.*, 2002; Berning *et al.*, 2003; Wang *et al.*, 2003; Um *et al.*, 2004).

1.3 Objectives

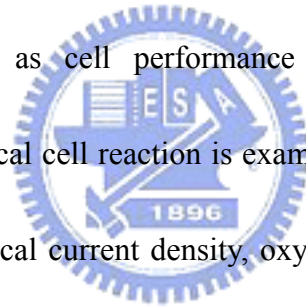
The above literature review shows that there is still much necessity to investigate the complex electrochemical and transport phenomena in the PEMFCs. Also, the relations between local cell reaction and physical properties are still not well understood. In this study, a multi-component, multi-phase, three-dimensional model of the PEMFCs is developed and numerically solved to enhance the understanding of the underlying characteristics of the cell reactions as well as various important factors that dominate the polarization curves of the PEMFCs.



1.4 Outlines

This dissertation is organized as follows. Chapter 2 introduces the model development and numerical method for solving the transport phenomenon and electrochemical reaction of the PEMFCs. Basic assumptions employed in the modeling process are also presented. Chapter 3 addresses the effects of existing temperature and humidification level gradients on cell boundaries are explored by the developed model. Polarization curves are presented for various scenarios of these water and thermal management schemes. The mechanisms that cause the variation of the performance curves are discussed. Also, the interrelations among the physical properties and cell performance are elucidated. The influences of transport component

design on the local physical properties as well as cell performance are described in Chapter 4. Two important design parameters, channel aspect ratio and gas diffusion layer thickness are examined in great detail. Transverse distributions of various model variables as well as local reaction rate are plotted and discussed. Chapter 5 introduces the investigation of the electrochemical reaction and performance of PEMFCs with a novel cathode flow channel shape. Through the assignment of various values of shoulder/channel (S/C) ratio at cathode outlet port, the channel configurations can be classified as convergent, straight and divergent shapes. Variations of various model transport variables as well as cell performance are proposed and discussed. Mechanism that dominates local cell reaction is examined through the comparison of the variation trends among local current density, oxygen concentration and potential fields. In Chapter 6, the conclusions of this investigation are drawn and suggestions for future study are proposed.



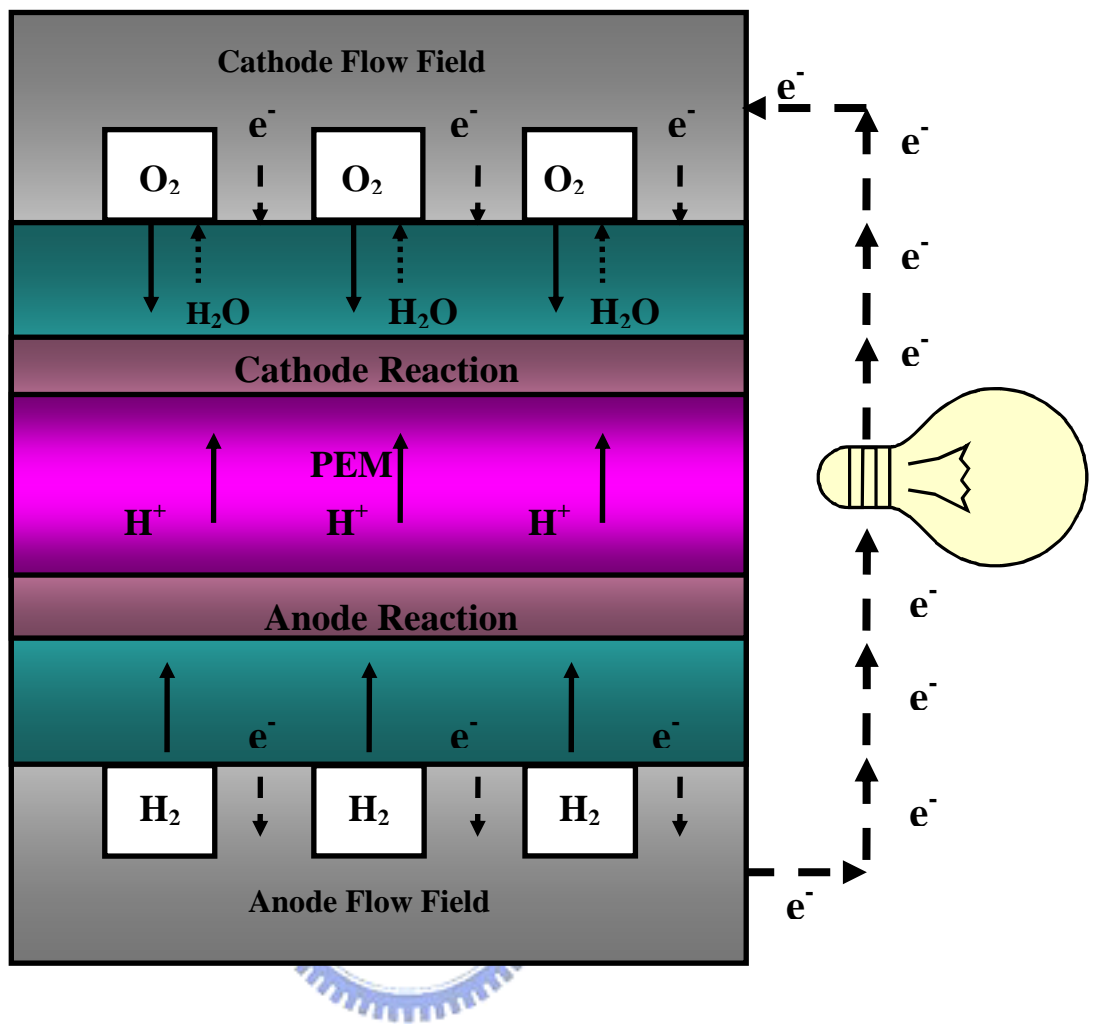


Fig. 1.1 Operating principle of a single PEMFC

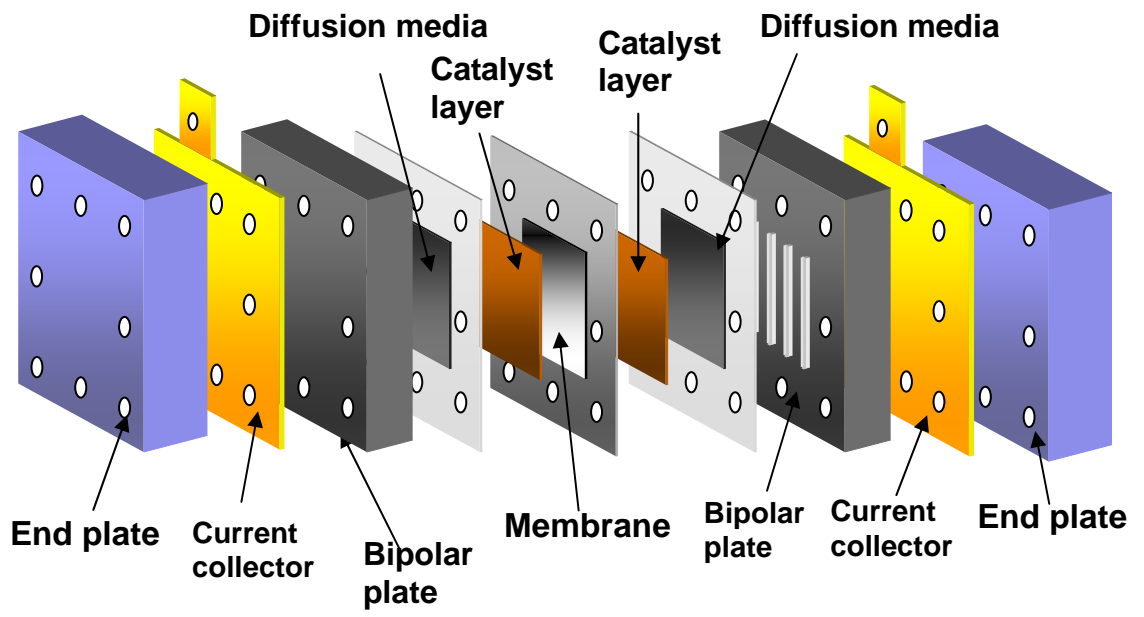


Fig. 1.2 Basic components of a single PEMFC



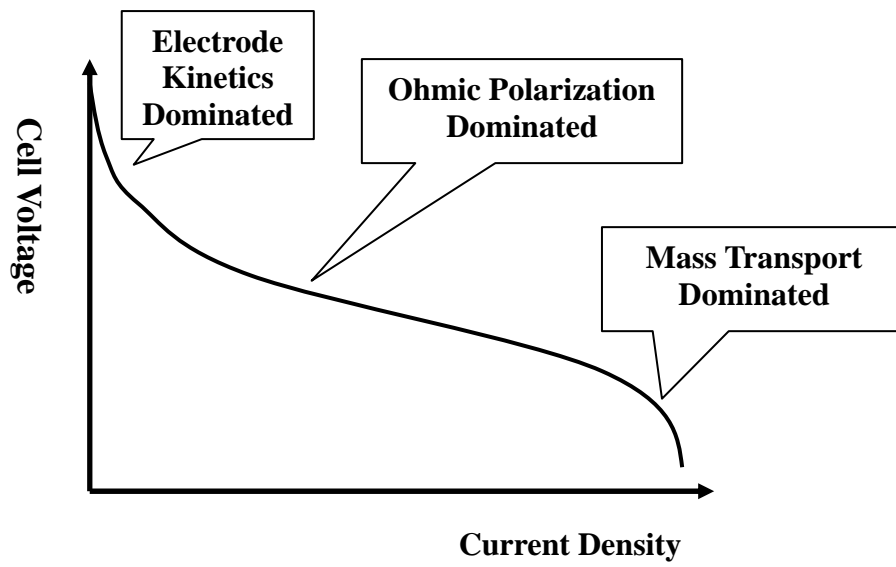


Fig. 1.3 The dominant mechanisms of cell performance



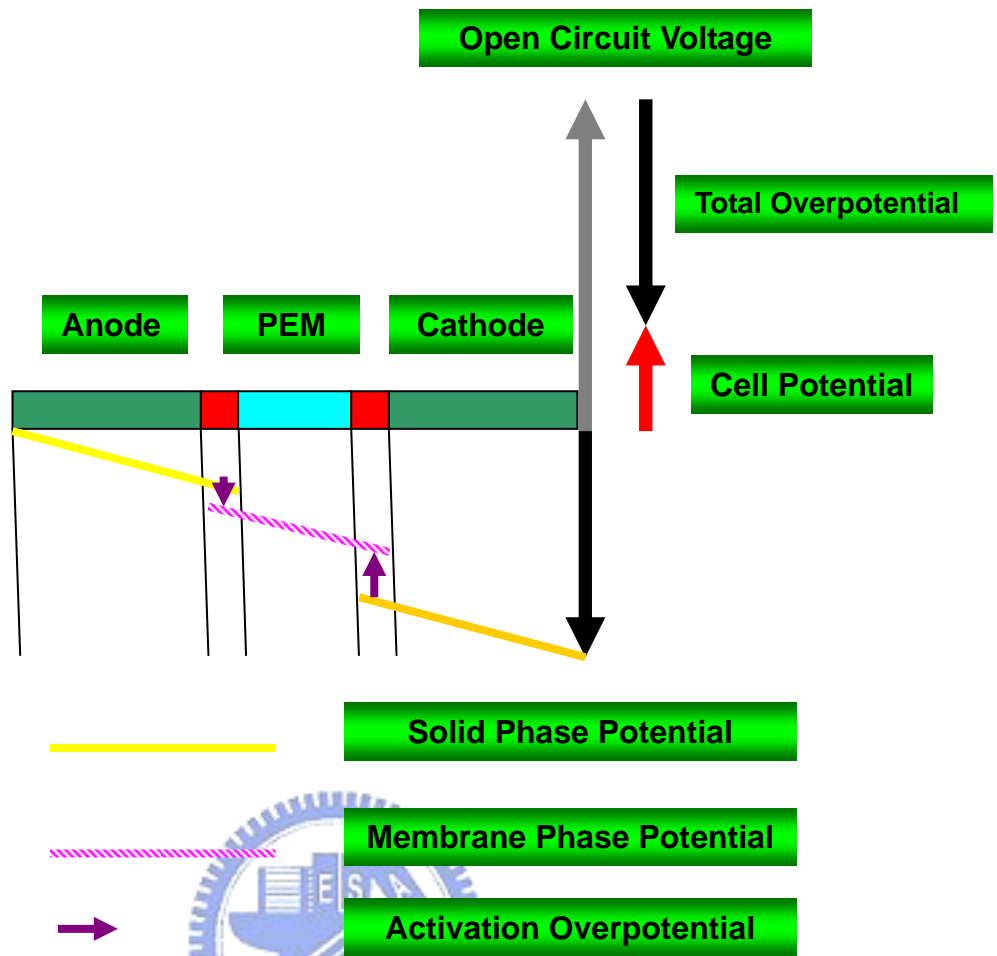


Fig. 1.4 Various overpotentials and available potential in fuel cells

CHAPTER 2

MATHEMATICAL MODELING

The computational fluid dynamic (CFD) method plays an important role on the resolution of the flow and temperature fields of the thermal-fluid problems. As the physical domain in a unit PEMFC is extremely thin, usually within the mm scale for the main components, it is extremely difficult to measure the local values of various important physical properties such as species concentration, velocity, temperature and current density. Based on the conservation law, several governing equations describing the inter-correlated relations of various properties can be developed and solved by numerical algorithm, providing essential and fundamental information to the engineer working on the technique development of fuel cell.

In this chapter, the general modeling framework employed in the subsequent study is presented. Equations depicting the electrochemical reactions as well as current transport are incorporated with the conservation equations of the CFD. Relations featuring the reaction kinetics, membrane conductivity and the transport parameters of the reactant and the product are also provided along with proper boundary conditions to complete the system of the investigation model.

2.1 *Model Description*

The general structure is periodical and symmetric for a fuel cell with straight flow channel. Therefore, as illustrated in Fig. 2.1, the physical region containing nine major components with one single channel and two half shoulders are considered in modeling. The anode, and cathode catalyst layers (CLs) and membrane are regarded as separate entities, despite the ultra-thinness of the CLs. Two GDLs are compressed by current collector ribs(shoulders) on each cell side to deliver reactants to the reaction sites under the ribs. The spaces in the bipolar plate (BP) grooves, commonly called the anode and cathode channels, are passages in which gases are transported throughout the cell. This work describes the following transport phenomena and reaction in a PEMFC:



- Three-dimensional convection and diffusion in flow channels and porous media;
- Electrochemical reactions in the catalyst layers of the anode and the cathode;
- Multi-species mass transport;
- Formation and transport of liquid water;
- Electronic current transport through bipolar plates and electrodes;
- Positive ionic current transport through the membrane and catalyst layers.

2.2 *Basic Assumptions*

Basic assumptions are made to simplify actual cell conditions in the theoretical model and thus facilitate the modeling approach of transport component and operating condition influences on transport phenomena and cell performance. The following are the most important:

- The Reynolds number of the fluid is below 100 due to low mixture velocity, laminar flow is considered;
- The GDLs, CLs and membrane are modeled as porous media;
- Each component has isotropic transport properties;
- The gaseous phase of the working fluid behaves as an ideal gas;
- The electric potential on the outer surface of each bipolar plate is constant;
- No charge accumulates in the electrodes and the domain is electrically neutral;
- The system operates in a steady state.

2.3 Governing Equations

A unified domain approach is employed to avoid tedious boundary condition appointments on the component interface in the following formulations. Instead, proper physical and transport properties such as porosity and permeability are designated on each distinct domain. This method can significantly simplify the model system equations and numerical processes. Also the boundary conditions at the

interfaces between different layers are not required (Gurau *et al.*, 1998; Um *et al.*, 2000; 2004; You *et al.*, 2002; Wang *et al.*, 2003).

2.3.1 Continuity Equation

The continuity equation is used to describe the mass conservation of mixture throughout the domain:

$$\nabla \cdot (\varepsilon^{\text{eff}} \rho \mathbf{U}) = 0 \quad (2-1)$$

where the mixture density ρ is the volume-weighted average of the phase mass concentration for the consideration of the two-phase flow (Wang *et al.*, 2001). It

can be expressed as:

$$\rho = \rho_l s + \rho_g (1 - s) \quad (2-2)$$

where s stands for the saturation level in porous medium, representing the volume fraction of the pore occupied by the liquid phase and can be given as:

$$s = \frac{V_l}{V_l + V_g} \quad (2-3)$$

2.3.2 Momentum Equation

The generalized Navier-Stokes equation is introduced to represent momentum conservation of the mixture; a source term is included to consider the additional drag

forces in the porous medium (Mazumder *et al.*, 2003; Wang *et al.*, 1993):

$$\nabla \cdot (\rho \varepsilon^{\text{eff}} \mathbf{U} \mathbf{U}) = -\varepsilon^{\text{eff}} \nabla P + \nabla \cdot (\varepsilon^{\text{eff}} \mu^{\text{eff}} \nabla \mathbf{U}) + \varepsilon^{\text{eff}} \rho_k \mathbf{g} + \mathbf{S}_m \quad (2-4)$$

where ε^{eff} represents the effective porosity given by $\varepsilon^{\text{eff}} = \varepsilon(1-s)$; μ^{eff} is the effective viscosity of the mixture; ρ_k is the kinetic density; S_m is the sum of Darcy and Forchheimer drag forces associated with the morphology (porosity and permeability) of the porous medium:

$$\mu^{\text{eff}} = \frac{\rho_l s + \rho_g (1-s)}{\left(\frac{k_{rl}}{v_l}\right) + \left(\frac{k_{rg}}{v_g}\right)} \quad (2-5)$$

$$\rho_k = \rho_l k_{rl} \frac{v}{v_l} + \rho_g k_{rg} \frac{v}{v_g} \quad (2-6)$$

$$S_m = -\frac{(\varepsilon^{\text{eff}})^2 \mathbf{U}}{\sqrt{K}} \left(\frac{\mu^{\text{eff}}}{\sqrt{K}} + \varepsilon^{\text{eff}} C_F \rho |\mathbf{U}| \right) \quad (2-7)$$

The momentum equation automatically becomes the Darcy equation in the porous area where the magnitudes of convection and diffusion term are extremely small. In Eq. (5), the relative permeabilities of the liquid and gas phase can be expressed as a function of saturation (Wang *et al.*, 2001):

$$k_{rl} = s^3 \quad (2-8)$$

$$k_{rg} = (1-s)^3 \quad (2-9)$$

2.3.3 Mass Transport

The mass fraction of each species in the gas mixture can be given as follows:

$$\nabla \cdot \left(\varepsilon^{\text{eff}} \rho w_\alpha \mathbf{U} k_{rg} \frac{v}{v_g} \right) = \nabla \cdot \left[\rho \sum_{\beta=1}^{n-1} D_{\alpha\beta} (\varepsilon^{\text{eff}})^\delta \nabla w_\beta \right] + S_{s\alpha} \quad (2-10)$$

Notably, the Bruggemann correction is applied in this equation to consider the mass transport in porous medium. The parameter δ is the tortuosity of the porous

medium. The multi-component diffusion coefficient $D_{\alpha\beta}$ is a function of species concentration and binary diffusion coefficient, the latter can be written as (Cussler, 1997; Wangard *et al.*, 2001):

$$D_{\gamma\delta} = \frac{0.0018583 \left[T^{\frac{3}{2}} \left(\frac{1}{M_\gamma} + \frac{1}{M_\delta} \right)^{\frac{1}{2}} \right]^\delta}{P \psi_{\gamma\delta} \Omega_{\gamma\delta}} \quad (2-11)$$

The source term $S_{s\alpha}$ defines the creation or consumption of species at the electrode catalyst sites and is given by:

$$S_{s,O_2} = \frac{S_{j,c} M_{O_2}}{4000F} \quad (2-12)$$

$$S_{s,H_2O} = \frac{-S_{j,c} M_{H_2O}}{2000F} + S_1 \quad (2-13)$$

$$S_{s,H_2} = \frac{S_{j,a} M_{H_2}}{2000F} \quad (2-14)$$



2.3.4 Electrochemical Reaction

At the electrode catalyst sites, reactants undergo an electrochemical reaction. Hydrogen is oxidized and oxygen reduced at the anode and the cathode, respectively. These two reactions are driven by the potential difference between the solid phase and the electrolyte phase, called the activation overpotential η . The activation overpotential in the anode tends to energize the electrons lost by hydrogen; at the cathode, hydrogen ions and electrons react with oxygen to form water. The

Bulter-Volmer equation describes this important phenomenon and is related to the source terms in Eq. (2-12)-(2-14):

$$S_{j,k} = A_v i_{\text{ref},k} \left(\frac{c_\alpha}{c_{\alpha,\text{ref}}} \right)^{\phi_\alpha} \left[\exp\left(\frac{\beta_{k,a} F \eta_k}{RT} \right) - \exp\left(\frac{-\beta_{k,c} F \eta_k}{RT} \right) \right] \quad (2-15)$$

where A_v is the effective reaction surface area of the catalyst particle and is closely related to the morphology and platinum loading of the catalyst layer. An expression for the relationship among these parameters is written as:

$$A_v = \frac{A_{\text{mas}} m_{\text{plt}}}{H_{\text{cat}}} \quad (2-16)$$

where A_{mas} is the catalyst area per unit mass of catalyst particle, m_{plt} represents the catalyst loading and H_{cat} stands for the catalyst layer thickness.

The term $i_{\text{ref},k}$ in Eq. (2-15) is the exchange current density, which characterizes the catalyst layers. Due to sluggishness of oxygen reduction reaction at the cathode, its value is several orders of magnitude smaller than that at the anode. Hence, the cathode exhibits significant activation overpotential during cell operation.

The experimental results of Parthasarathy yielded the following relation

(Parthasarathy *et al.*, 1992):

$$i_{\text{ref},\text{o}_2} = 10^4 \exp\left(3.507 - \frac{4001}{T} \right) \quad (2-17)$$

2.3.5 Potential Fields

Two charged species, electrons and protons, are transported in the fuel cell and subjected to individual driving forces determined by the potential gradient. The negatively charged electrons flow through the catalyst layer, the gas diffusion layer, and the bipolar plate; the positively charged protons flow goes through the catalyst layer and the membrane. The catalyst layer is a source of charges at the anode and a sink at the cathode. The assumption of electro-neutrality yields the following expressions for electrical current conservation in the catalyst layer:

$$\nabla \cdot (-\sigma_{\text{sol}} \nabla \phi_{\text{sol}}) = -S_{j,k} \quad (2-18)$$

$$\nabla \cdot (-\sigma_{\text{mem}} \nabla \phi_{\text{mem}}) = S_{j,k} \quad (2-19)$$

Outside the catalyst layer, no current sink or source is presented and the right hand sides of Eqs. (2-18) and (2-19) are equal to zero, suggesting that no species is created or consumed; electrical current conservation is therefore easily understood.

In the membrane, the ionic conductivity σ_{mem} is strongly related to the water content γ , defined as the ratio of the number of water molecules to the number of the charge sites (Springer *et al.*, 1991):

$$\sigma_{\text{mem}} = (0.005139\gamma - 0.00326) \left\{ \exp \left[1268 \left(\frac{1}{303} - \frac{1}{T} \right) \right] \right\} \quad (2-20)$$

An empirical relationship between the water content in the membrane and the partial pressure of the water is:

$$\gamma = \begin{cases} 0.043 + 17.81a - 39.85a^2 + 36a^3 & \text{for } 0 < a \leq 1 \\ 12.6 + 1.4a & \text{for } 1 < a \leq 3 \end{cases} \quad (2-21)$$

where a is the water activity and is given by:

$$a = \frac{X_w P}{P_{\text{sat}}} \quad (2-22)$$

In the above equation, the saturation pressure varies with temperature and can be determined from the thermodynamic table or using the following empirical expression:

$$\log_{10} p_{\text{sat}} = -2.1794 + 0.02953T - 9.1837 \cdot 10^{-5} T^2 + 1.4454 \cdot 10^{-7} T^3 \quad (2-23)$$

where T is in unit of $^{\circ}\text{C}$ and P_{sat} is in unit of bars. This formulation can be utilized with a relative error less than 1.5 percent in the range of 20°C to 100°C .

2.3.6 *Liquid Water Transport*

During fuel cell operation, water partial pressure in the electrode may exceed its saturation pressure if the local water concentration is high. Therefore, liquid water is possibly formed and occupies the electrode pore space. Operating the cell at a high reaction rate may cause severe mass transport overpotential because the diffusion species are blocked. Additionally, extremely small pores in the fuel cell porous media cause the capillary force to dominate liquid water transport in the hydrophilic surfaces. Smaller pores correspond to stronger capillary forces. However, the actual expression of this force cannot be formulated because the real liquid-gas interface configuration is not tractable. The generalized Richards equation, originally developed for the oil

recovery field and adapted by Wang *et al.* (1992) to study two-phase flow transport in capillary porous medium, is applied :

$$\nabla \cdot \left(\varepsilon^{\text{eff}} \rho \mathbf{U} k_{rl} \frac{\mathbf{v}}{v_1} \right) + \nabla \cdot \mathbf{N}_1 = \nabla \cdot \left(\varepsilon^{\text{eff}} D^c \nabla s - \frac{K k_{rl} k_{rg} (\rho_l - \rho_g) \mathbf{g}}{k_{rl} v_g + k_{rg} v_l} \right) + S_1 \quad (2-24)$$

where N_1 represents the liquid water flux due to electro-osmosis drag in the membrane, it is associated with proton transport and is a function of local current density and the electro-osmotic drag coefficient. The first term on the right-hand side describes the capillary pressure effect, whereas the second term is the gravitational separation between the liquid and gas phases of water. The variable D^c is the capillary diffusion coefficient and can be expressed as a function of saturation level, surface tension, and permeability (Wang and Beckermann, 1997; You and Liu, 2002):

$$D^c = \frac{K k_{rl} k_{rg} \left[\zeta \cos \theta_c \left(\frac{\varepsilon^{\text{eff}}}{K} \right)^{\frac{1}{2}} (-3.789s^2 + 3.338s - 0.966) \right]}{k_{rl} v_g + k_{rg} v_l} \quad (2-25)$$

where k_{rl} , k_{rg} are the relative permeabilities associated with pore space reduction by the co-existence of multiphase fluids.

The last term in Eq. (2-24) is introduced to account for liquid water condensation or evaporation, and can be expressed as (He *et al.*, 2000):

$$S_1 = M_1 r_{\text{con}} \frac{\varepsilon^{\text{eff}} x_w}{RT} (x_w p - p_{\text{sat}}) y + r_{\text{eva}} \varepsilon^{\text{eff}} s \rho_1 (x_w p - p_{\text{sat}}) (1 - y) \quad (2-26)$$

where y is a constant with unity or zero value depending on water species condensation or evaporation scenarios in the porous medium.

2.3.7 Energy Equation

The temperature field of the cell domain can be obtained from solving energy equation which describes the thermal energy conservation. Except for inlet and outlet boundaries, enthalpy generation is considered from three sources; joule heating due to current transport in the medium, electrochemical reaction irreversibility due to over-potential at electrodes, and latent heat of water due to phase change. Many physical properties are closely related to temperature in the cell domain. First, mixture velocities at channel inlet ports for a fixed reactant stoichiometry and a given cell geometry are primarily decided by their thermodynamic states subsequently dictated by mixture temperatures. Secondly, electrochemical reaction kinetic in the catalyst layer and membrane conductivity are also influenced by local temperatures. Thirdly, the temperature field is also responsible for water formation or evaporation. Consequently, it has certain effects on reactant concentration and membrane water content. The generalized steady state energy equation can be expressed as:

$$\nabla \cdot (\varepsilon \rho h \mathbf{U}) = \nabla \cdot (\kappa^{\text{eff}} \nabla T + \sum_{\alpha=1}^n \sum_{\beta=1}^{n-1} \rho D_{\alpha\beta} \nabla w_{\beta} h_{\alpha}) + \varepsilon \boldsymbol{\tau} : \nabla \mathbf{U} - S_j \eta + \frac{|\mathbf{i} \cdot \mathbf{i}|}{\sigma} + S_h \quad (2-27)$$

where the first two terms on the right hand side represent the conduction energy and reactant enthalpy flux, the third term is the irreversible viscous dissipation. The fourth

and the fifth terms describe the electrical related thermal effects where S_j is the volumetric current density in catalyst layer that can be expressed by the Butler-Volmer equation. The last term results from the consideration of phase change when water evaporation or condensation occurs in the cell domain and is presented in the next section following the phase change formulation. Detail expansion of this equation in scalar form is expressed in App. A.

2.4 Boundary Conditions

2.4.1 Flow Field Boundary Conditions



Model boundaries fall into three categories as indicated by Fig. 2.1 - symmetric boundaries (SBs), impermeable boundaries (IBs), and channel boundaries (CBs). The SB conditions are imposed on both transverse sides of the model and physical quantities such as mass flux or momentum flux have zero gradients. The Neumann conditions are also assigned on IB, the top (or bottom) and side surfaces of the channels adjacent to the bipolar plates. Additionally, non-slip conditions are applied for the IB velocity fields.

Unlike these simple boundary conditions, the CB conditions importantly determine operating conditions and cell performance. At the inlet ports of the channels,

velocities, thermodynamic states, and mass fractions of mixture are specified according to the desired operating scenarios and mixture of interest. Based on the stoichiometric flow ratio, the inlet velocity of the reactant is:

$$v_k = \frac{\xi I W_{\text{cel}} L_{\text{cha}} R T_{k,\text{in}}}{q F W_{\text{cha}} H_{\text{cha}} \left(1 - \frac{P_{\text{sat},w,k}}{P_k} \right) x_{\alpha,\text{in}} P_k} \quad (2-28)$$

The mass fractions of the species on the CB are specified according to operating pressure and fully saturated humidification condition. Dalton's law and the ideal gas law yield the molar fraction of individual species. The mass fraction, used in the preceding formulation, is given by:

$$w_i = \frac{x_i M_i}{\sum_j x_j M_j} \quad (2-29)$$



2.4.2 Potential Field Boundary Conditions

Specific solid phase potential is assigned to each bipolar plate outer surface in addition to these transport variables. This value is generally set to zero on the anode BP outer surface, and a cell total overpotential is set on the cathode BP. Meanwhile, a membrane phase potential zero gradient is applied at the interface between GDL and CL, representing a protonic current absence through this interface because of the lack of a conducting medium. This method yields the local current density in the cell from ohmic law; it also accurately yields the catalyst layer activation overpotential. The cell potential can be obtained from the following expression:

$$V_{ce1} = V_{oc} + \eta_{tot} \quad (2-30)$$

where η_{tot} is the total cell overpotential and V_{oc} is the open circuit voltage given

by (He *et al.*, 2000):

$$V_{oc} = 0.2329 + 0.0025T \quad (2-31)$$

2.5 *Method of Solution*

2.5.1 *Calculation Procedure*

The nonlinearity and coupling in the model formulation eliminate an analytical solution possibility. The forgoing transport equations are numerically solved using the commercial computational fluid dynamic code CFD-ACE⁺, based on the control volume formulation and the SIMPLE algorithm (Patankar, 1980; CFD-ACETM User Manual, 2004; Liu *et al.*, 2005; Soong *et al.*, 2005). The numerical flow chart of present investigation is shown in Fig. 2.2. The calculation is regarded to be converged if the normalized residual of each variable is less than 10e-4.

2.5.2 *Model Validation*

Three structure mesh systems- 60x30x12, 80x40x16, and 90x48x18 are constructed to explore numerical result dependence on computational cell number. Base model geometries and operating conditions are listed in Table 2.1. Model component electrochemical parameters and transport properties, obtained mainly from open literature (Um *et al.*, 2000; Mazumder and Cole, 20003, Marr and Li, 1999;

Weng *et al.*, 2005; Hum and Li, 2004; Nguyen *et al.*, 2004; <http://www.etek-inc.com/home.php>), are listed in Table 2.2. Numerical calculations are performed on a Pentium IV 2.4GHz PC with a 1G RAM. The mesh system (80x40x16) is adopted because current density values are satisfactory with an error range of 2% when using base model geometries and parameters of these two Tables, please see Table 2.3. Based on the reported operating conditions and component geometries of Wang *et al.*'s report (Wang, Husar, Zhou and Liu, 2004), data in Figure 2.3 show that the present model to be consistent with previous studies.



Table 2.1 Cell geometries and operating conditions of base model

Geometry and condition	Value	Unit
Domain length	50	mm
Domain width	1.6	mm
Gas channel width	0.8	mm
Domain height	4.303	mm
Gas channel height	0.8	mm
Diffusion layer height	0.254	mm
Catalyst layer height	0.01	mm
Membrane height	0.175	mm
Molar ratio of cathode side dry air (N ₂ /O ₂)	79/21	
Reactant relative humidity	100%	
Reactant stoichiometry	3	
Cell back pressure	2	atm
Operating temperature	353	K



Table 2.2 Electrochemical parameters and transport properties

Parameters and Properties	Value	Unit	Sources
Porosity of the diffusion and catalyst layer	0.4		(Um <i>et al.</i> , 2000)
Porosity of the membrane	0.28		(Um <i>et al.</i> , 2000)
Permeability of the diffusion and catalyst layer	2.3E-11	m ²	(CFD-ACE™ User Manual, 2004)
Permeability of the membrane	1.0E-18	m ²	(CFD-ACE™ User Manual, 2004)
Tortuosity of the diffusion and catalyst layer	1.5		(Mazumder and Cole, 2003)
Tortuosity of the membrane	3		(Mazumder and Cole, 2003)
Condensation rate constant	100	sec ⁻¹	(He <i>et al.</i> , 2000)
Evaporation rate constant	100	atm ⁻¹ sec ⁻¹	(He <i>et al.</i> , 2000)
Concentration dependence of H ₂	0.5		(Marr and Li, 1999)
Concentration dependence of O ₂	1		(Marr and Li, 1999)
Transfer coefficients at anode (anodic and cathodic)	0.5		(Mazumder and Cole, 2003)
Transfer coefficients at cathode(anodic and cathodic)	1.5		(Mazumder and Cole, 2003)
Electrical conductivity of electrode	114	S m ⁻¹	(Hum and Li, 2004)
Catalyst loading	0.4	mg cm ⁻²	
Catalyst surface area per unit mass	100	m ² g ⁻¹	http://www.etek-inc.com/home.php
Contact angel	0	degree	(Natarajan and Nguyen, 2001)
Exchange current density for anode reaction	1.4E5	A cm ⁻³	(Nguyen <i>et al.</i> , 2004)
Reference concentration of oxygen	3.39E-6	mol cm ⁻³	(Nguyen <i>et al.</i> , 2004)
Reference concentration of hydrogen	5.64E-5	mol cm ⁻³	(Nguyen <i>et al.</i> , 2004)

Table 2.3 Results of three computation grid systems based on the parameters in Table 2.1 and Table 2.2

Grid	60x30x12			80x40x16			90x48x18	
Cell Voltage (V)	current density (A/cm ²)	cpu time	relative error (100%)	current density (A/cm ²)	cpu time	relative error (100%)	current density (A/cm ²)	cpu time
0.47	0.866	17324	3.12	0.885	43989	0.99	0.894	105114
0.57	0.645	14657	3.84	0.661	37643	1.43	0.670	89178
0.67	0.433	6113	3.81	0.444	31270	1.44	0.450	79827
0.77	0.239	4688	3.51	0.245	24386	1.33	0.248	56722
0.87	0.075	3467	2.67	0.077	20043	1.00	0.077	47062



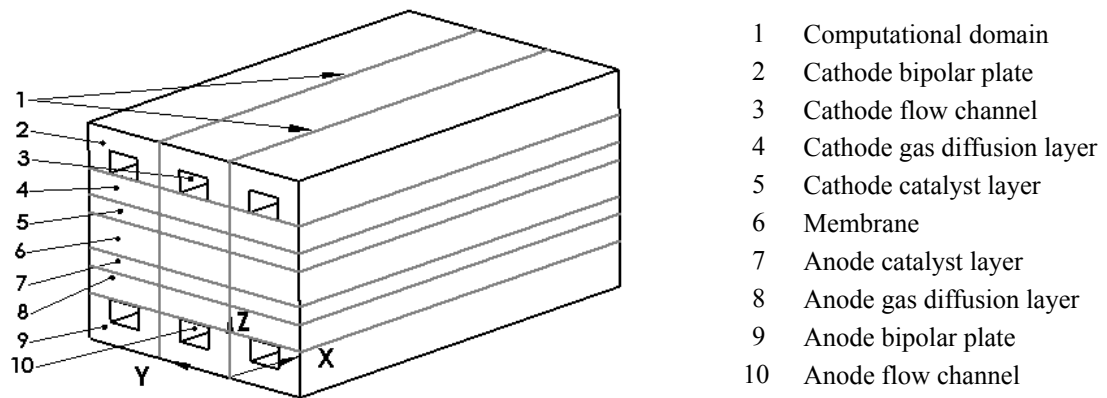


Fig. 2.1. Physical and computational domains considered in this study



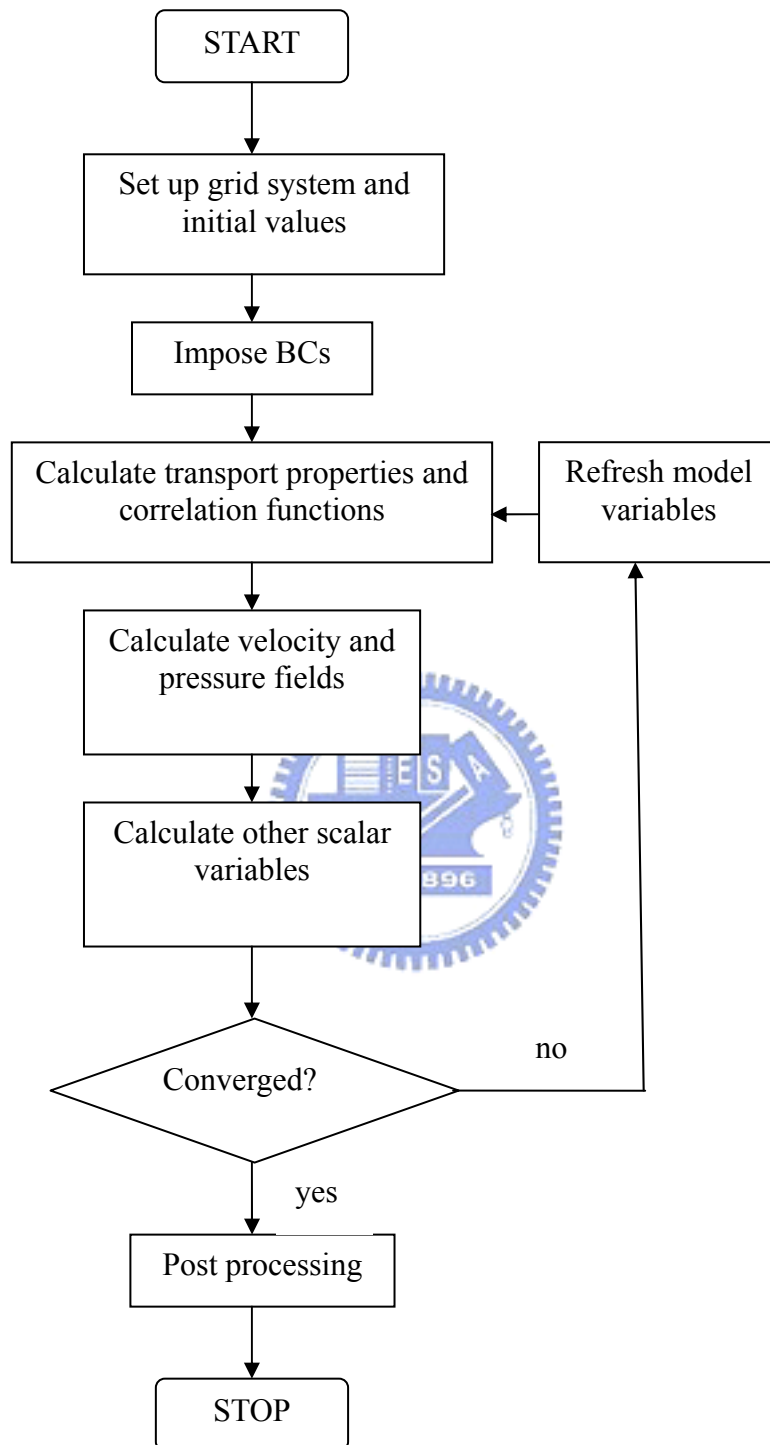


Fig. 2.2. Numerical flow chart of current study

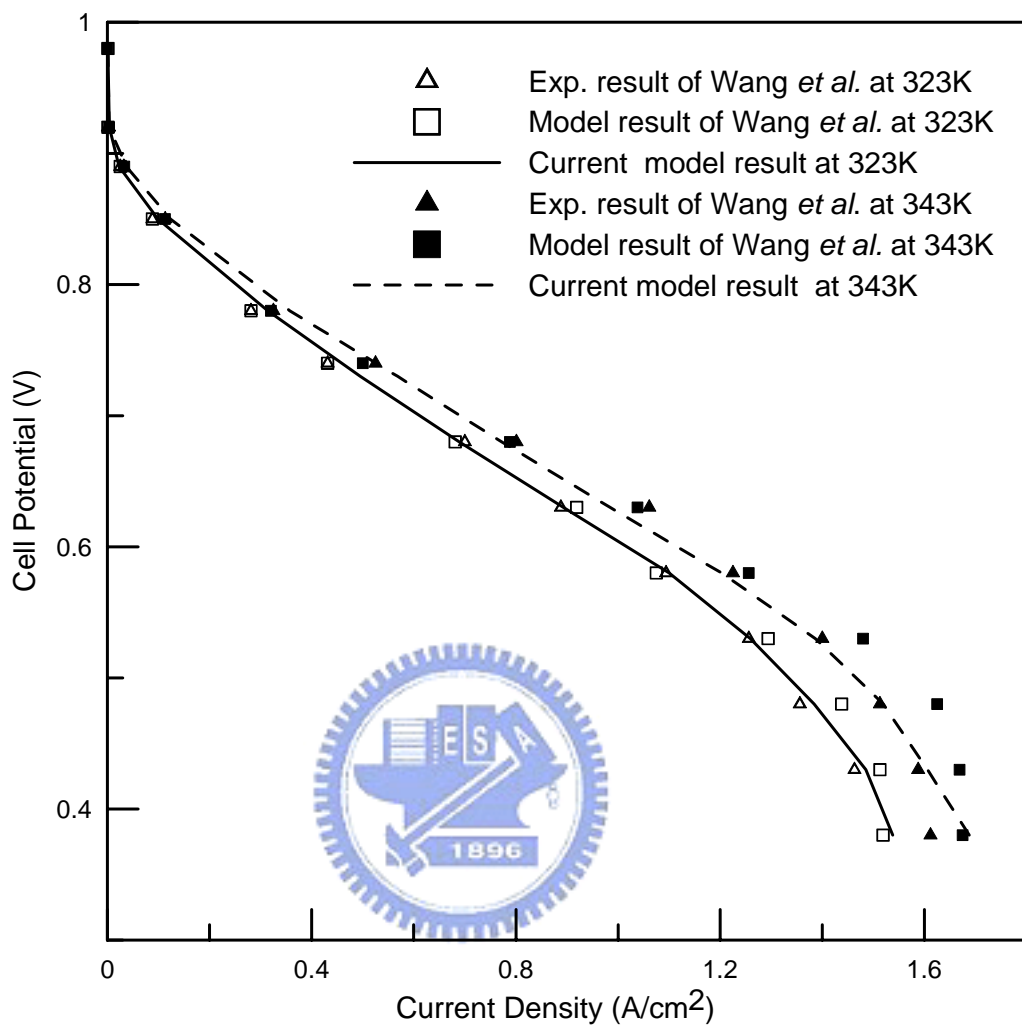


Figure 2.3 Comparison of current model results with Wang *et al.* at 323K and 343K

CHAPTER 3

EFFECTS OF TEMPERATURE AND HUMIDIFICATION LEVELS ON THE PERFORMANCE OF PROTON EXCHANGE MEMBRANE FUEL CELLS

3.1 *Introduction*

The water and thermal management plays an important role on the transport phenomena and electrochemical reaction of the PEMFCs. When fuel cell operates with a proper control of these two factors, the membrane is able to conduct ions efficiently because of the higher water content and electric conductivity. Moreover, elevated cell temperature is beneficial to the enhancement of ionic phase conductivity as well as the prevention of liquid water formation if the counter effect on membrane water content can be ignored. Unfortunately, these three factors are coupled and mutual interlocked during the operation of PEMFCs, increasing the difficulty of reaching an optimal operation of the water and thermal management. Generally, the operating temperature and humidification level are two important factors of implementing the cell water and thermal management. In the following sections, cell polarization curves obtained from scenarios of various temperature gradient conditions as well as humidification schemes are presented. Prediction results presented are two-fold: first, those based on equal cell boundary temperatures on both

sides while reactant humidification temperatures are altered; second, those based on equal temperatures of boundary and humidification on each side with a temperature gradient imposed between the both sides. To examine the interrelation between the two main factors considered, humidification level and cell boundary temperatures varied from higher values (353K to 363K) to lower values (333K to 323K). This differs from previous studies with only one parameter changed (Berning and Djilali, 2003; Wang *et al.*, 2003), hence a more vivid situation that simulates cell operation is expected. The mechanisms that vary the trends of these curves are interpreted from the viewpoints of membrane conductivity and its water content.



3.2 *Effects of Humidification Scheme*

In regard to promoting proton transport through the membrane, proper water vapor concentration in the cell region is crucial. Enhanced or reduced humidification scheme results on one or both sides of channel inlet ports are first reported. Subscripts B, H, A, and C in the legend of Fig. 5.1 and the following figures represent boundary, humidification, anode, and cathode respectively. A temperature difference of 10K between cell and humidification level, either larger or smaller, is posted on designated positions.

3.2.1 *Enhanced Humidification Scenario*

Results between the anode enhanced humidification scheme and the base cases with these four temperatures being equal are compared in Fig. 3.1. Three cell boundary temperatures 333K, 343K, and 353K are considered. The data in Fig. 3.1 reveal a concentration polarization effect for this humidification scheme in higher current density. Also, this decay onset depends on cell temperature, and at higher cell temperature this phenomenon appears earlier. Since inlet gas is fully saturated according to the humidification level, the anode mixture temperature decreases from heat transfer with the cell solid phase, and saturation level in the anode is elevated due to water condensation. This causes effective transport passage decrease of anode gas, promoting concentration overpotential. Another contributor to this is hydrogen depletion from the oxidation reaction in the anode catalyst layer, such that water partial pressure increases as well as condensation probability.

Cathode enhanced humidification scheme influence with cathode mixture remained at 10K greater than cell temperature as shown in Fig 3.2. The results reveal a more serious concentration overpotential than the previous scheme; and the limiting current density decreases at higher cell temperature. That is, cell performance dependence on temperature reversed at a high reaction rate for the present humidification scheme. Higher humidification temperature and corresponding low oxygen concentration in the inlet port may be considered to cause extra concentration

overpotential at high cell temperature for this humidification scheme. However, reactant gas inlet velocity adjusts to alleviate dilution caused by high vapor concentration and satisfies the required stoichiometry as indicated in Eq. (20). In this context, high humidification level and water generation combined effect in the cathode reaction leads to a stronger effective porosity decay in the cathode electrode and decreases limiting current density at high cell temperature.

The simulation results for anode reduced humidification scheme are presented in Fig. 3.3. In this case, effect is found on the larger performance decay compared with the base cases. This cell voltage reduction attributes to water swell deficiency in the membrane due to lower inlet water concentration. Since the membrane conductivity is dictated by water content - the number of water molecules per fixed charged site, the supplied water vapor from anode inlet port is not enough to keep the membrane fully hydrated, such that the membrane proton transport is more difficult and activates a larger ohmic overpotential.

3.2.2 *Reduced Humidification Scenario*

Figure 3.4 shows the effect of cathode reduced humidification scheme effect on cell output for various cell temperatures. Comparing with base cases, it reveals the merit of applying the current scheme at a higher current density, causing cell voltage and performance increase at each cell temperature. Gas passage clogging prevention

in the electrode is responsible for this gain because the produced water in the cathode reaction balances the lower inlet water concentration. However, an additional study (not shown in the figure) revealed that it reaches a plateau above cell temperatures of 348K as large amounts of water generation exceed reduced humidity. For further improved performance, a larger humidification temperature reduction is needed to influence the membrane water content. Also, at medium reaction rate and high cell temperature, cell resistance shows a slight variation. This is because the variation of membrane water content and conductivity arise from lower cathode water concentration.

3.2.3 *Combined Enhanced and Reduced Humidification Scenario*

To examine the impact of greater cell humidification gradient, the combined results of anode reduced and cathode enhanced humidification schemes are depicted in Fig 3.5. The ohmic and concentration overpotentials clearly are all altered compared with base cases. Cell performance in this operating condition can be regarded as the individual scheme superposition. Nevertheless, the plot for 353K exhibits a smaller decay at high reaction rate than the result in Fig. 3.2, as the reaction rate at the conduction dominated region is suppressed from low anode humidity and the accompanying small membrane conductivity. Consequently, the series concentration overpotential at low cell voltage is slightly released. In a further study

that reverses the humidification condition of the previous case, the same expected individual scheme superposition is shown. However, this effect is intrinsically nonlinear due to complicated mechanisms of the coupled transport phenomena.

3.3 Effects of Cell Temperature Gradient

Increasing cell bulk temperature reportedly creates a positive influence on cell performance (Wang *et al.*, 2001). Prediction results containing a series boundary and humidification temperatures variation on one electrode with others fixed are reported in this section. The reactants are also fully saturated based on boundary temperature. Polarization curves are plotted as total cell overpotential versus current density as cell temperature used in Eq. (22) cannot be obtained.

3.3.1 Cell Performance at Higher Cathode Temperature

Results with anode temperatures increased from 333K to 353K at 353K cathode temperatures are presented in Fig. 3.6. Cell current density does not change significantly until a higher reaction rate according to findings. Ionic phase conductivity along central channel direction on the membrane middle plane is drawn in Fig. 3.7 at total cell overpotential 0.98V for further result information. It reveals a positive effect of anode side temperature on the conductivity. According to Eq. (2-19), a higher membrane temperature corresponds to greater membrane conductivity.

Therefore, the conductivity is the largest for the case of 353K anode side temperature when cathode side temperature remains at 353K. Another interesting point disclosed from this figure is that the conductivity around the channel inlet region is smaller than that at rear region. This is attributed to the fact that higher cathode side temperature reduces the water activity and membrane water content. However, heat generation and water formation from cell reaction increase the membrane conductivity at channel rear region. Consequently, at 333K anode temperatures, cell current density exhibits a sensible decrease compared with other higher anode temperature situations. A similar scenario with 333K cathode temperature was also calculated. However, no appreciable cell performance variation is revealed. This can be explained by the anode kinetic independence with temperature that leads to trivial cell output change.

3.3.2 Cell Performance at Higher Anode Temperature

The prediction result at 353K anode temperatures and continuous cathode temperature variation from 333K to 353K is represented in Fig. 3.8. Obviously, the output current density increased monotonously with cathode temperature change, indicating that cell behavior is dominated by the electrochemical reaction kinetic rather than conduction or concentration overpotentials. With sluggish cathode oxygen reduction, cathode exchange current density is several orders of magnitude smaller

then the anode value, and a higher cathode temperature is beneficial for cell reaction and electricity generation.

3.3.3 Cell Performance at Lower Anode Temperature

Temperature gradient effect at low anode temperatures 333K and cathode temperatures varied from 333K to 353K is shown in Fig. 3.9. It indicates that current density dependence on cathode temperature variation has an entirely different tendency between medium and high cell reaction rates. Membrane conductivities along central channel direction on middle section for total cell overpotentials of 0.6V and 0.98V are plotted in Fig. 3.10 for further investigation. The data that ionic phase conductivity increases from channel entrance to exit. However, when the cathode side temperature is much higher than anode temperature 333K, ionic conductivity declines drastically at channel entrance. This is attributed to the reason that higher cathode temperature reduce the water activity at anode side and the corresponding membrane water content, according to Eq. (2-21). Therefore, the ionic phase conductivity decreases subsequently despite its positive effect of higher temperature on conductivity. This phenomena are obvious at cathode temperature of 343K and 353K in Fig. 3.10(a) and at 343K, 348K and 353K in Fig. 3.10(b). Consequently, it reverses the intrinsic relation between cell temperature and performance at high reaction rate.

3.4 Local Distributions of Model Variables

Various temperature and humidification gradient effects on cell performance are previously presented. Displaying local physical property variations such as reactant concentration, temperature, and saturation level offers a more insightful understanding of the coupled transport phenomena in the PEMFCs.

3.4.1 Temperature Field

Temperature contours in cathode GDL at the $x=0.025\text{m}$ section with 353K anode temperatures and 343K, 333K cathode temperatures are shown in Fig. 3.11. The total cell overpotential is at 0.8V. The upper region of the plot is adjacent to the cathode channel and shoulders, while the lower boundary of the plot is connected to the CL. Obviously, as CL is the main source of heat generation; the highest temperature appears at the bottom of GDL. Meanwhile, on this CL interface, the central region exhibits greater temperature as the cathode BP and shoulder have more capability to dissipate heat than the channel.

3.4.2 Oxygen Concentration Distribution

The expected effect on cell physical properties is justifiable given the temperature distribution. Local oxygen mass fractions for the previous cases are shown in Fig. 3.12. The data in this figure indicate that a higher GDL and CL temperature corresponds to lower oxygen concentration. This can be attributed to the

higher reaction rate from Eq. (19) and greater membrane conductivity. More oxygen is consumed in the cell reaction as a result, and local concentration is reduced.

3.4.3 Water Saturation Level

Another temperature field influence can be observed in Fig. 3.13, which is the water saturation level in the GDL for the same scenarios. There are two important points that can be observed from this plot. First, as the transport direction is opposite to that of oxygen, the GDL shoulder region tends to accumulate more water vapor than the GDL channel region, leading to a higher saturation level at this location. Secondly, water vapor saturation pressure decreases at lower temperature, such that local water vapor partial pressure is apt to exceed saturation pressure. Consequently, local saturation level increases with a 333K cathode temperature. The further influence of this phenomenon is that reactant and product transport passages are hindered and concentration overpotential is elevated.

3.5 Tendency Comparisons between Predicted and Other Experimental Results

To support the numerical predictions in the preceding sections, experimental results from other research groups with similar scenarios of interested cases are proposed. However, as the detailed information concerning the experimental cell and operating conditions are not available, the comparison is merely intended to show the

variation trends between than. Furthermore, according to the survey from open literatures, only a few cases are able to be utilized in the comparisons.

Figure 3.14 shows the experimental results of the effects of cathode humidification levels on cell performance for a PEM fuel cell with active surface area of 7.2 x 7.2 cm (Wang *et al.*, 2003). The cell temperature and anode humidification temperature are maintained at 343K while the cathode humidification temperature varied from 313K to 353K. The results exhibit quite similar tendencies of the polarization curves with current modeling results which subjected to enhanced and reduced cathode humidification schemes. That is, reduction of cathode humidification temperature is beneficial to the reactant transport and the concentration polarization at high reaction region is alleviated. Meanwhile, the increase of cathode humidification temperature such as at 353K causes stronger concentration overpotential. In Fig. 3.15, experimental results of enhanced anode and cathode humidification levels are presented [Lee *et al.*, 1999b]. As delineated from this figure, the cell performance has a severe decay when the anode/cathode humidification temperatures increase from 358K/348K to 368K/358K at a constant operating temperature of 343K. This tendency is quite consistent with current numerical results of anode and cathode enhanced humidification schemes. Despite the lack of complete data and information

of these experiments, the correctness of modeling predictions are justified by these results.

3.6 *Summary*

The three-dimensional, multi-component and multi-physics model has been applied to explore the temperature gradient and humidification perturbation effects on PEMFCs. This model accounts for various species transport and the two-phase flow problem. The CL local activation overpotential resolution is also achieved. According to the model prediction results and discussion, the following conclusions can be addressed:

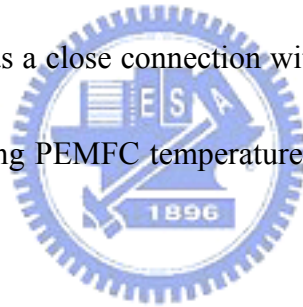


1. The anode humidification level bears the impact of concentration and ohmic overpotentials on cell performance at elevated and reduced situations respectively.
2. Proper cathode humidification level reduction benefits cathode reactant transport and improves polarization concentration at a high reaction rate.
3. Despite its nonlinear behavior, a suitable PEMFC humidification scheme can be reached by carefully using the individual humidification level effect on either side of the cell.
4. Temperature gradient effect on cell performance exhibits entirely different behaviors according to its direction and magnitude. When the cathode temperature

is fixed at a lower level, the anode temperature variation has no noticeable change in output current. However, when it is specified at a higher value, a larger temperature gradient is harmful at high current density.

5. Positive cell temperature gradient effect on its performance is found for medium reaction rate at a lower anode temperature. However, this trend is reversed at a higher reaction rate due to membrane dehydration.

6. Local physical property contours demonstrate interrelations among the temperature field, local oxygen concentration, and water saturation level. As a result, cell performance has a close connection with these property variations, and the essential role of existing PEMFC temperature and humidification gradients is elucidated.



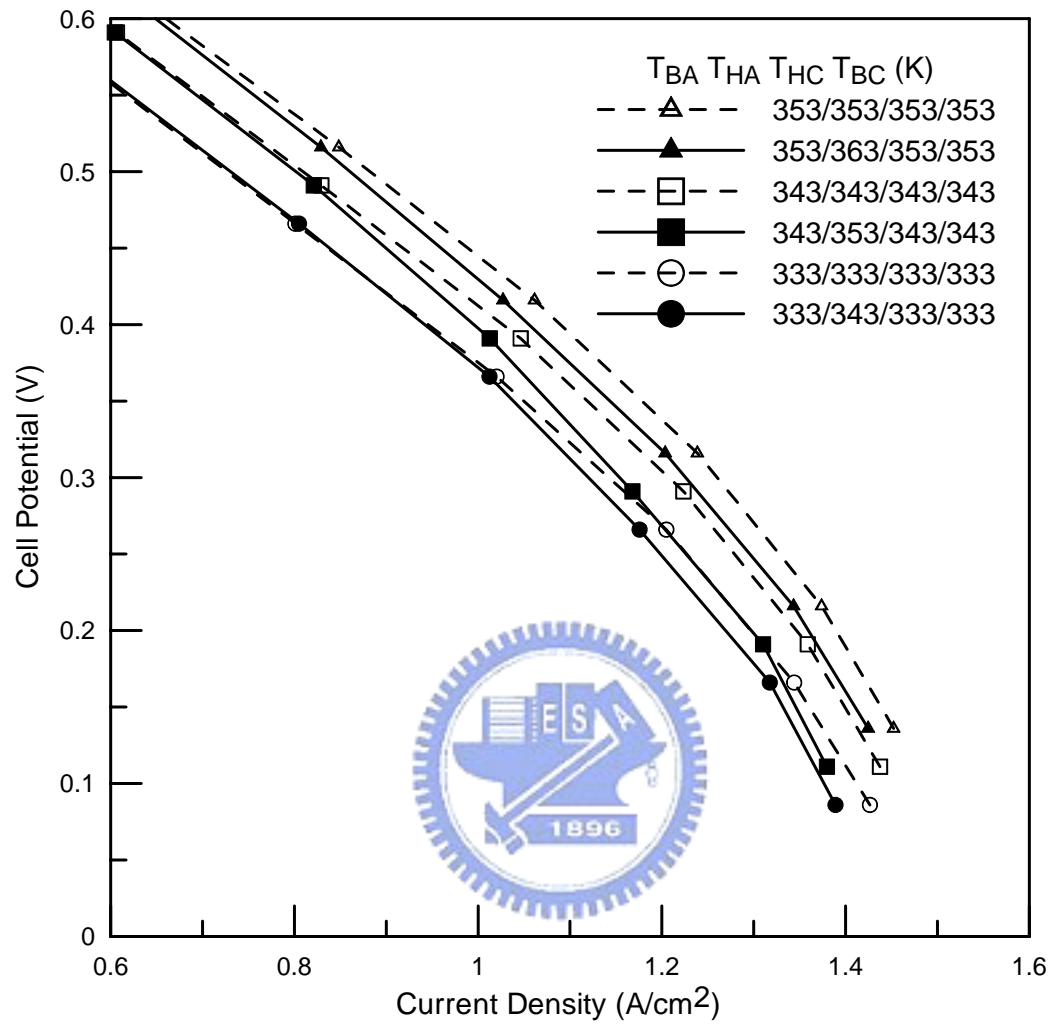


Fig. 3.1. Effect of anode enhanced humidification scheme with 10K of anode humidification level greater than cell temperature for cell temperatures 333K, 343K and 353K

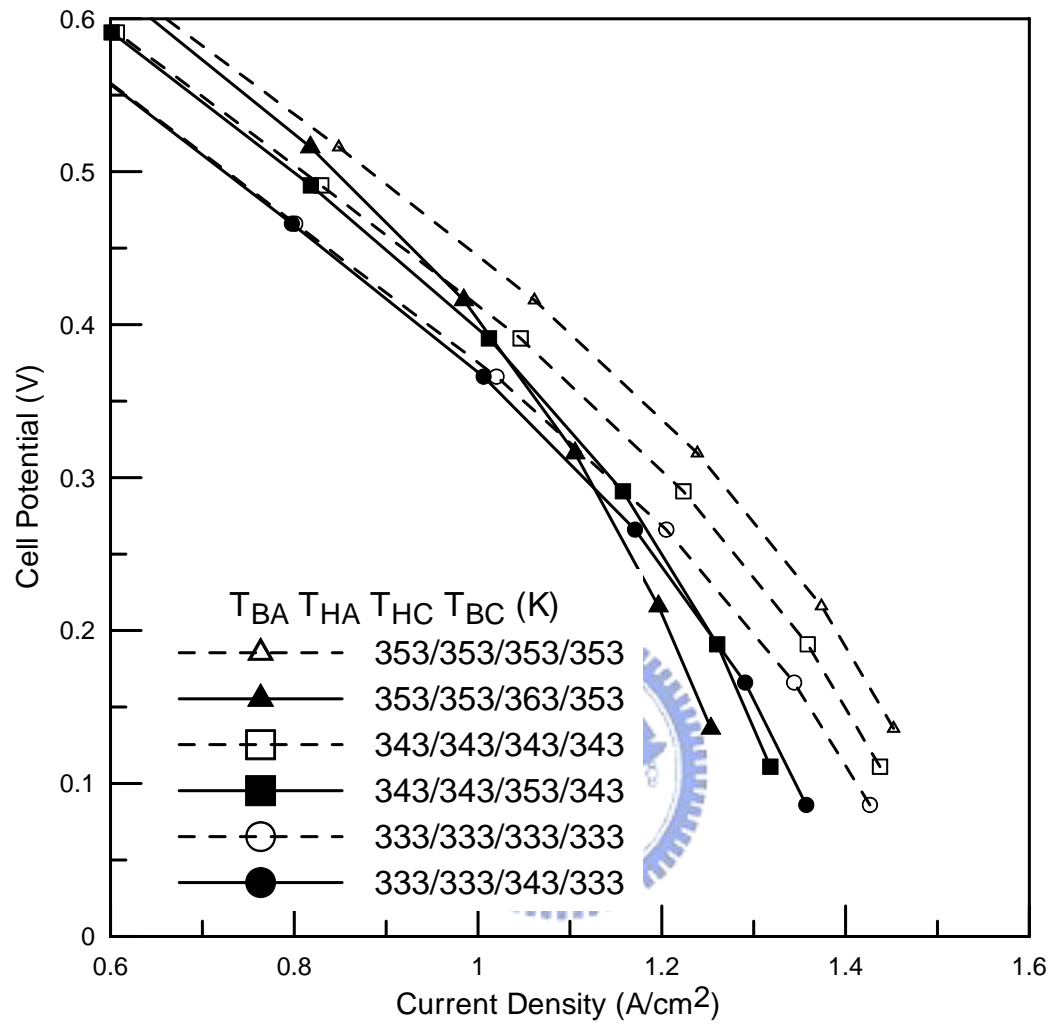


Fig. 3.2. Effect of cathode enhanced humidification scheme with 10K of cathode humidification level greater than cell temperature for cell temperatures 333K, 343K and 353K

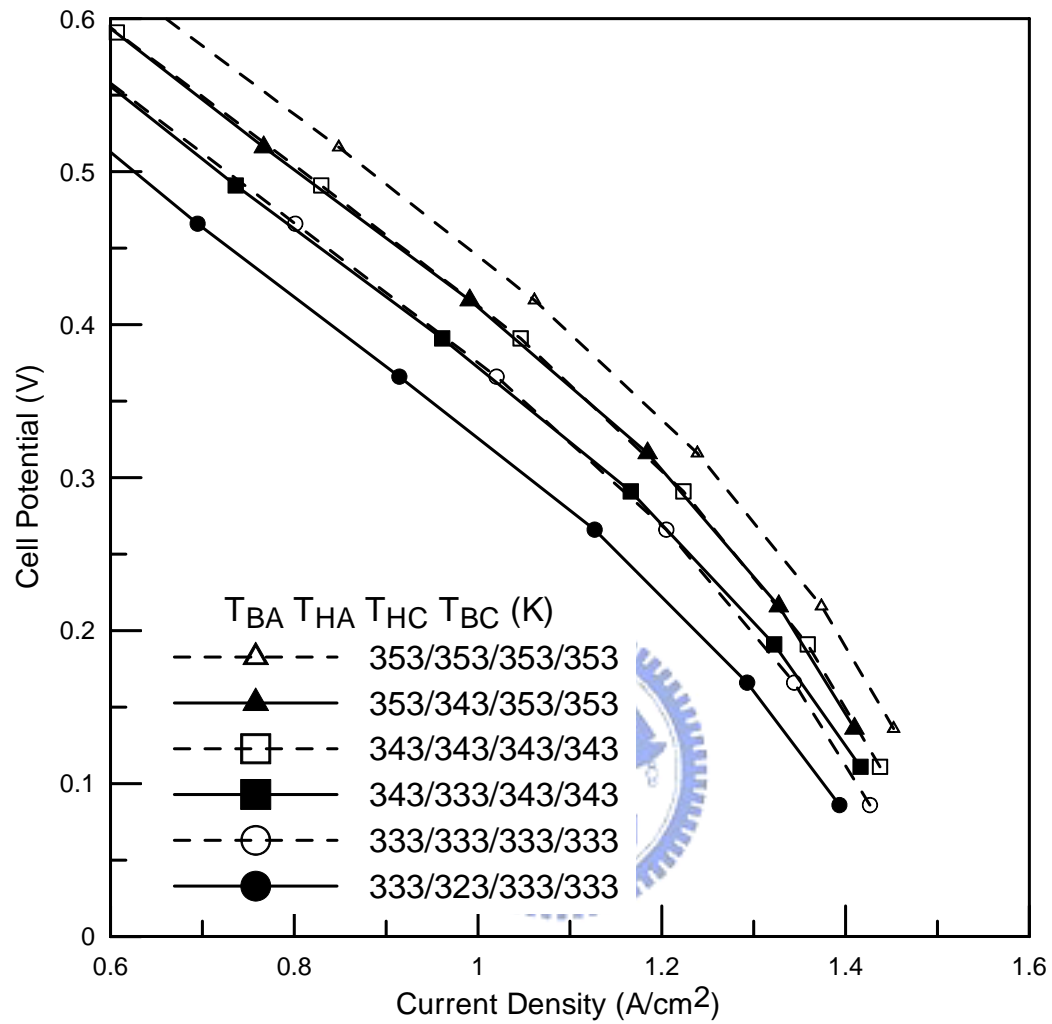


Fig. 3.3. Effect of anode reduced humidification scheme with 10K of anode humidification level smaller than cell temperature for cell temperatures 333K, 343K and 353K

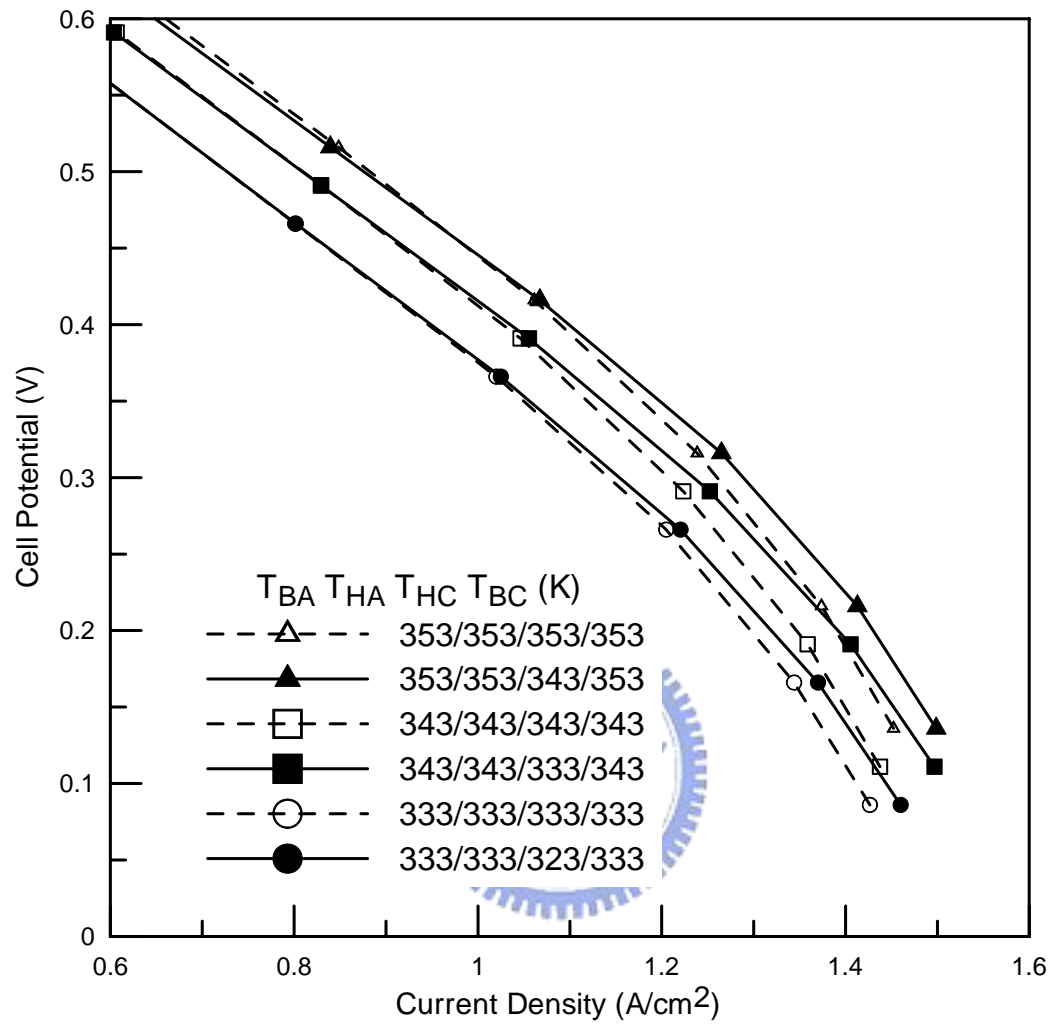


Fig. 3.4. Effect of cathode reduced humidification scheme with 10K of cathode humidification level smaller than cell temperature for cell temperatures 333K, 343K and 353K

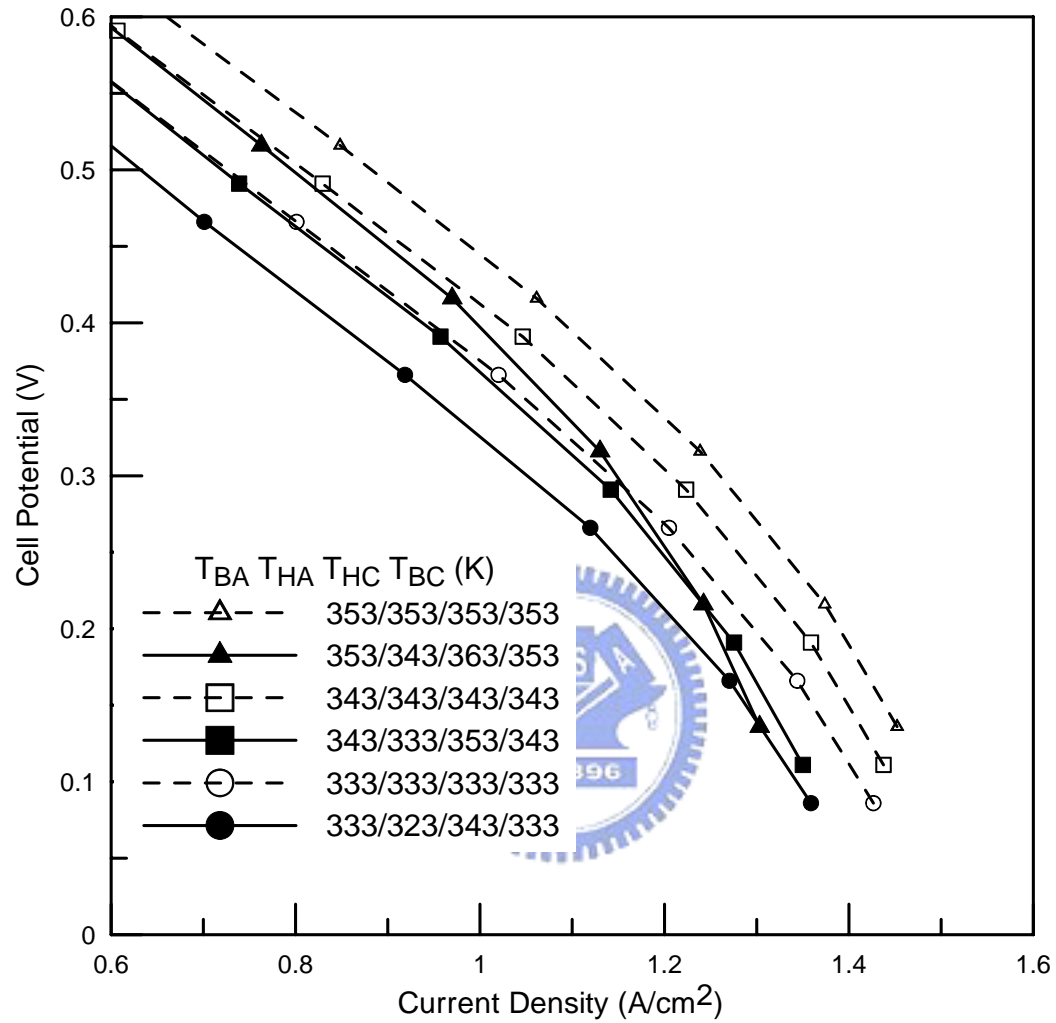


Fig. 3.5. Effect of humidification gradient that combines anode reduced and cathode enhanced schemes for cell temperatures 333K, 343K and 353K

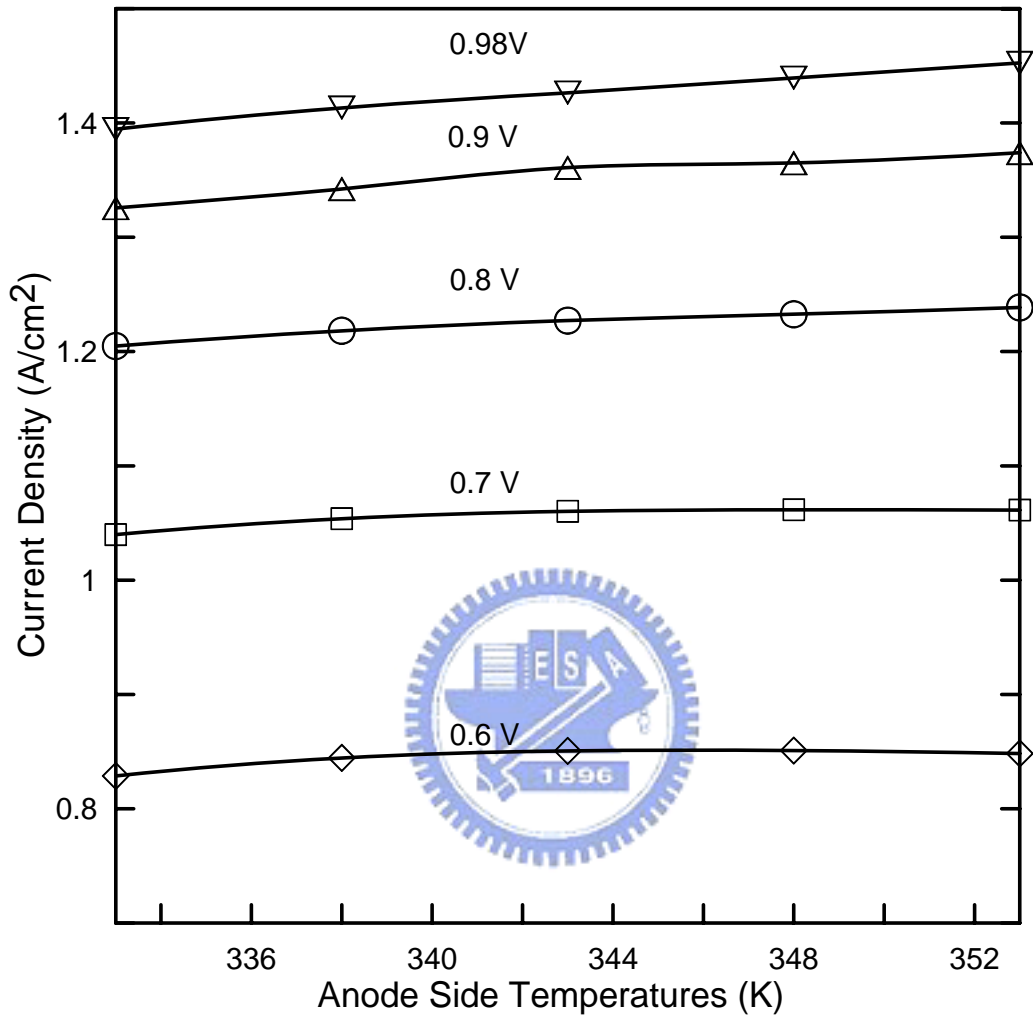


Fig. 3.6. Cell performance at various total overpotentials with 353K cathode temperatures and anode temperatures varied from 333K to 353K

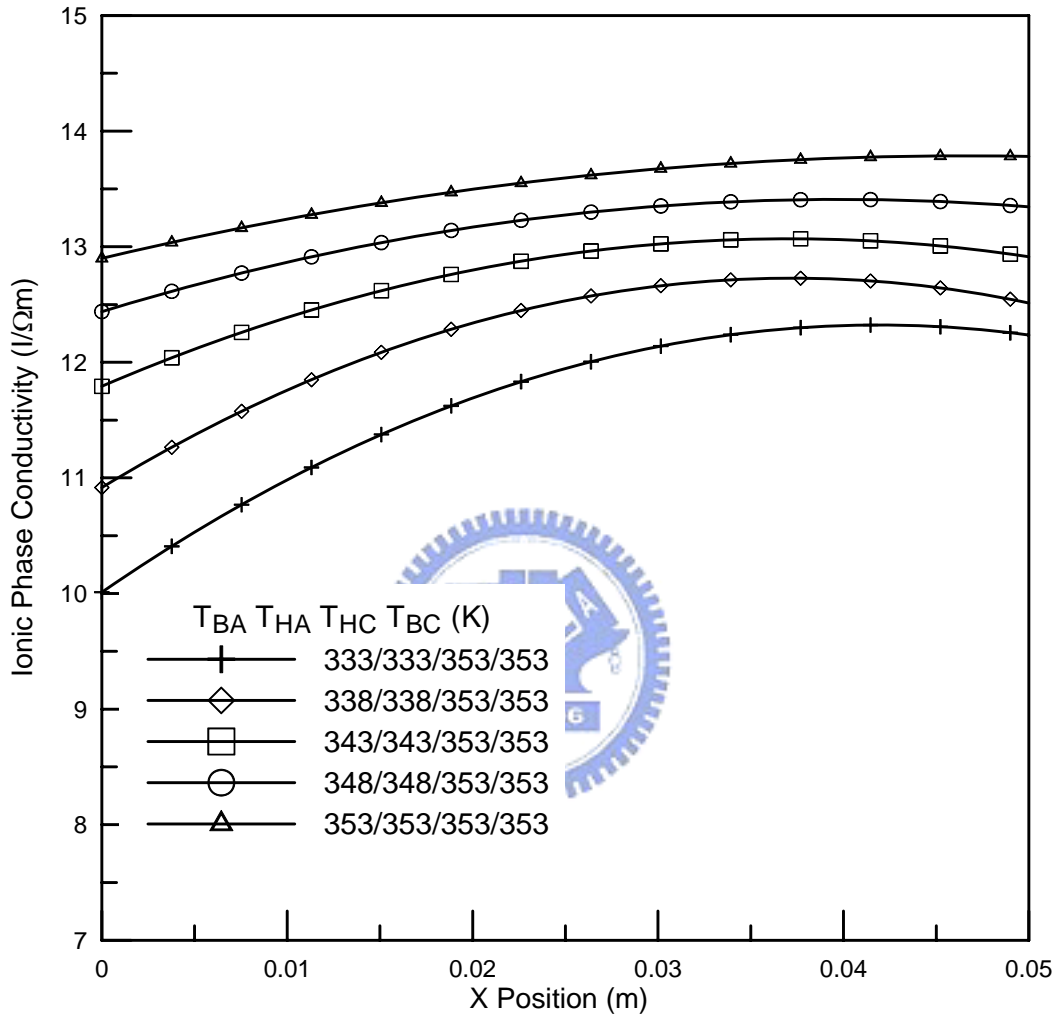


Fig. 3.7. Ionic Phase conductivity along central channel direction on membrane middle section for cases in Fig. 3.6

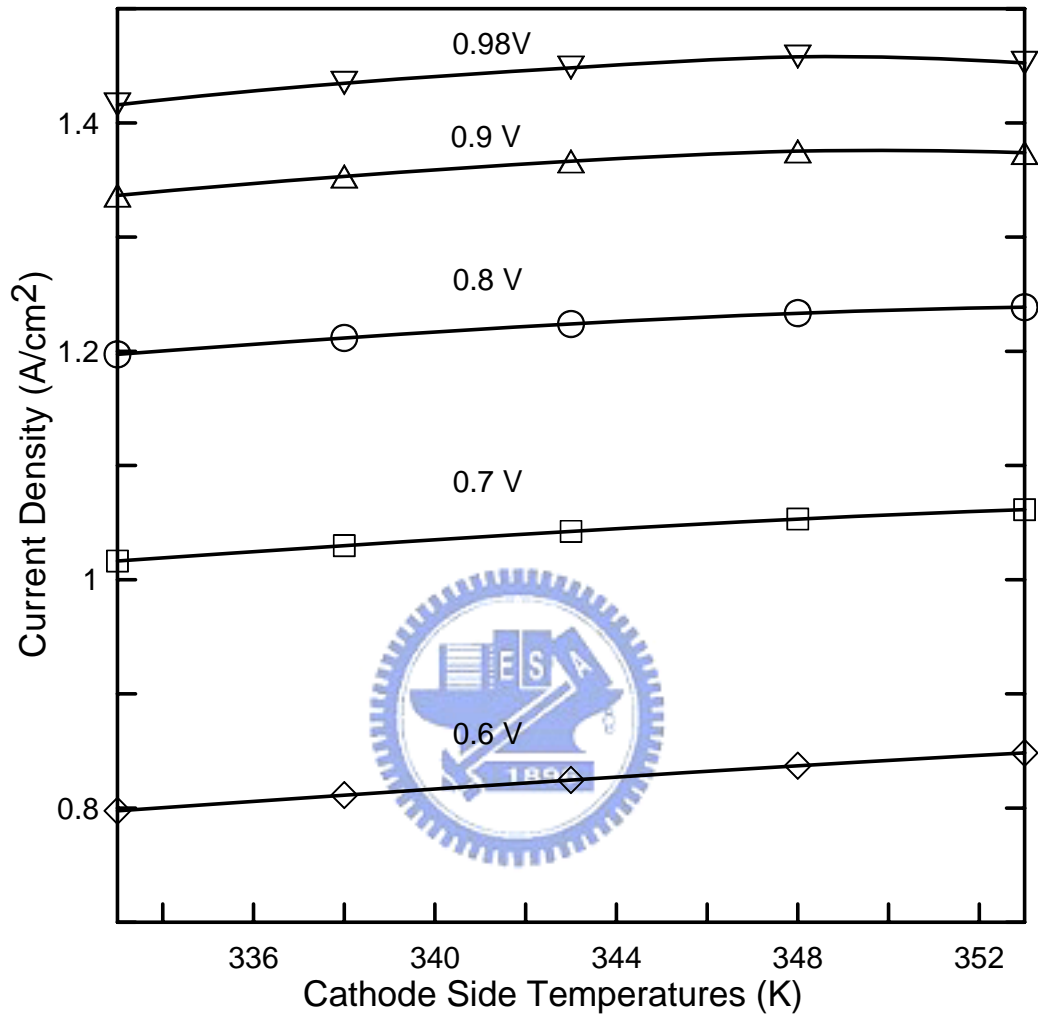


Fig. 3.8. Cell performance at various total overpotentials with 353K anode temperatures and cathode temperatures varied from 333K to 353K

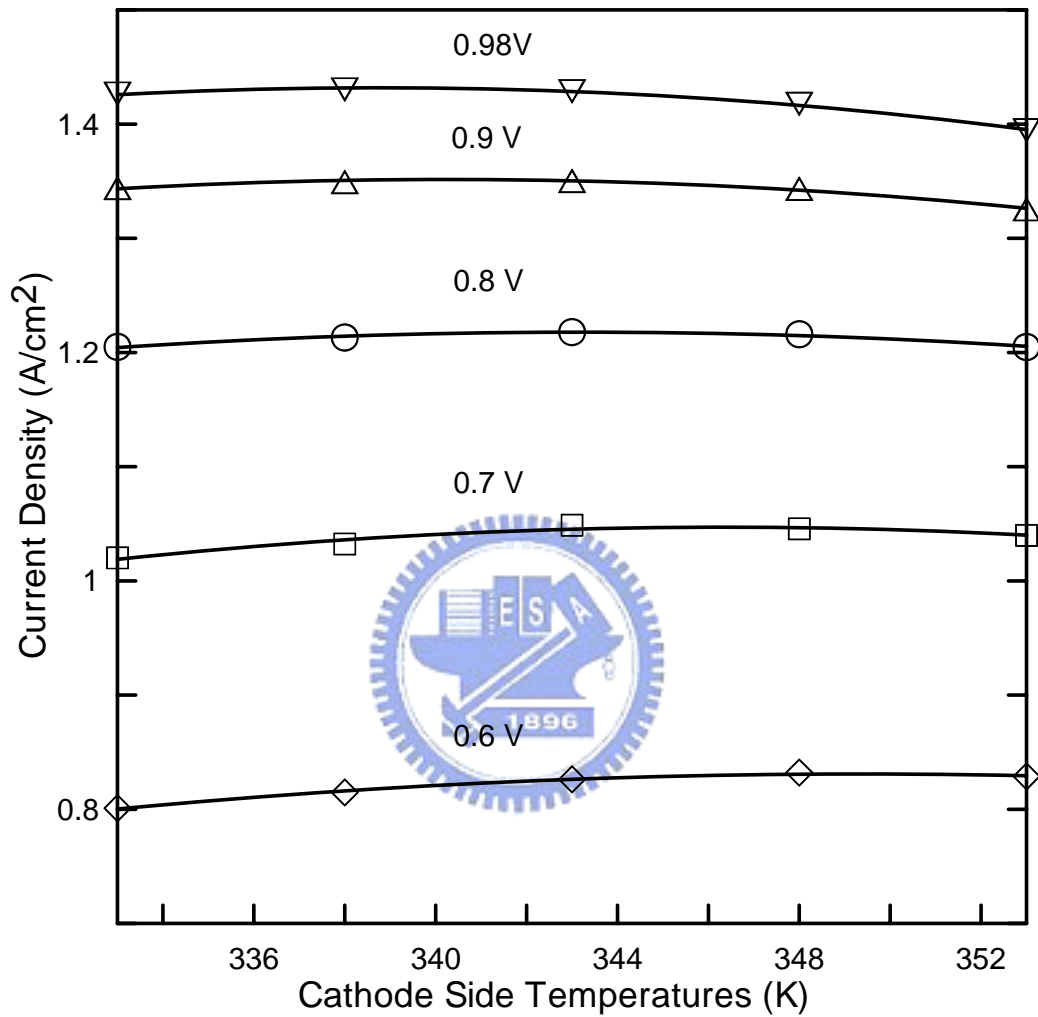


Fig. 3.9. Cell performance at various total overpotentials with 333K anode temperatures and cathode temperatures varied from 333K to 353K

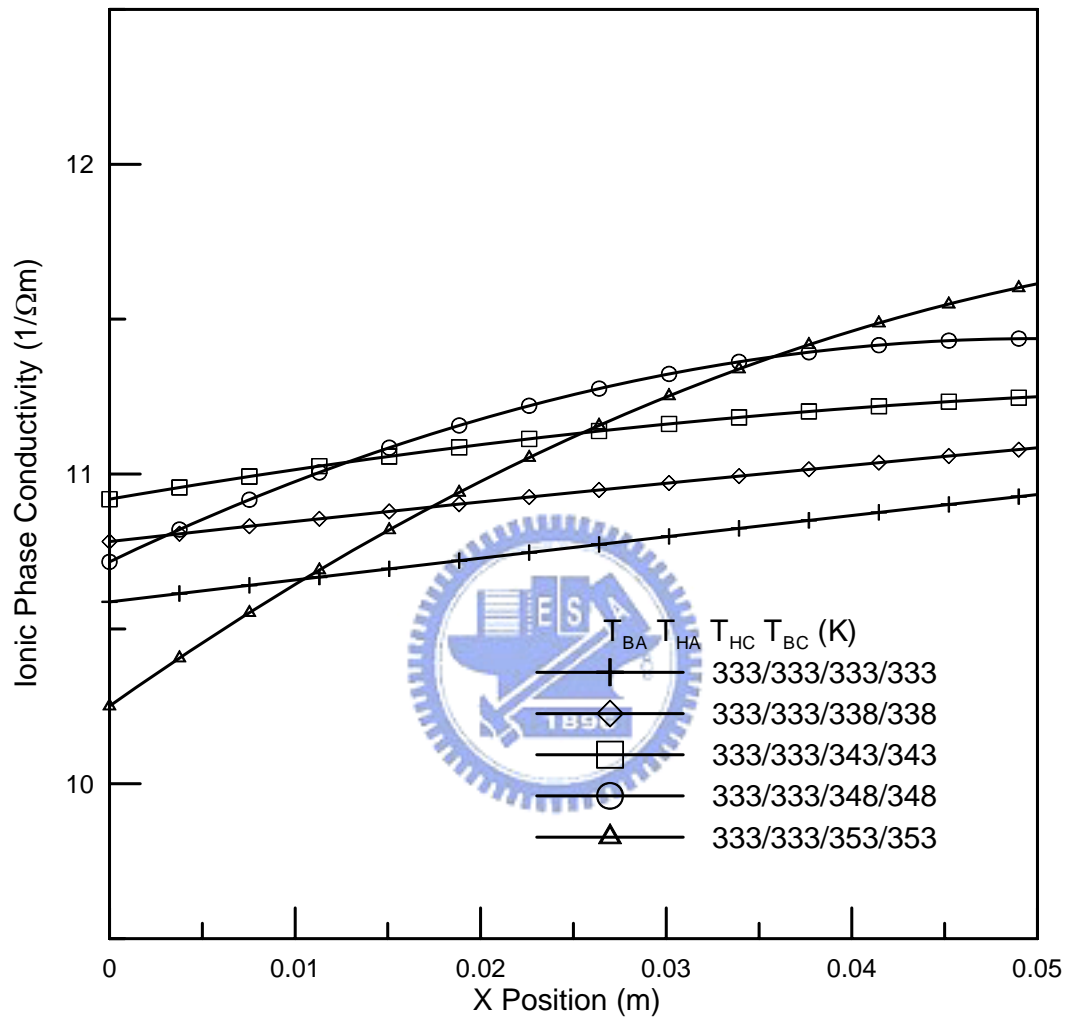


Fig. 3.10(a). Ionic phase conductivity along central channel direction on membrane middle section for cases in Fig. 3.9 at total cell overpotential of 0.6V

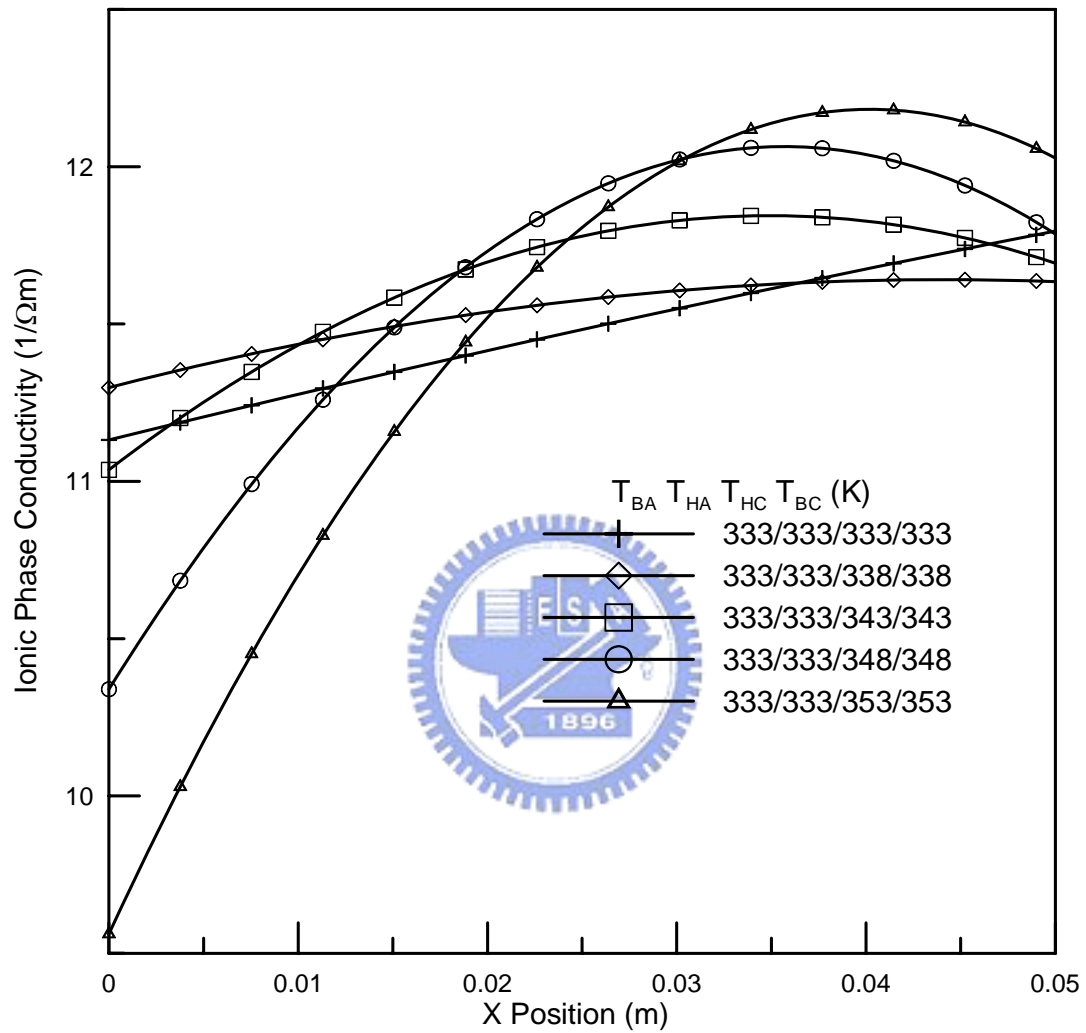


Fig. 3.10(b). Ionic phase conductivity along central channel direction on membrane middle section for cases in Fig. 3.9 at total cell overpotential of 0.98V

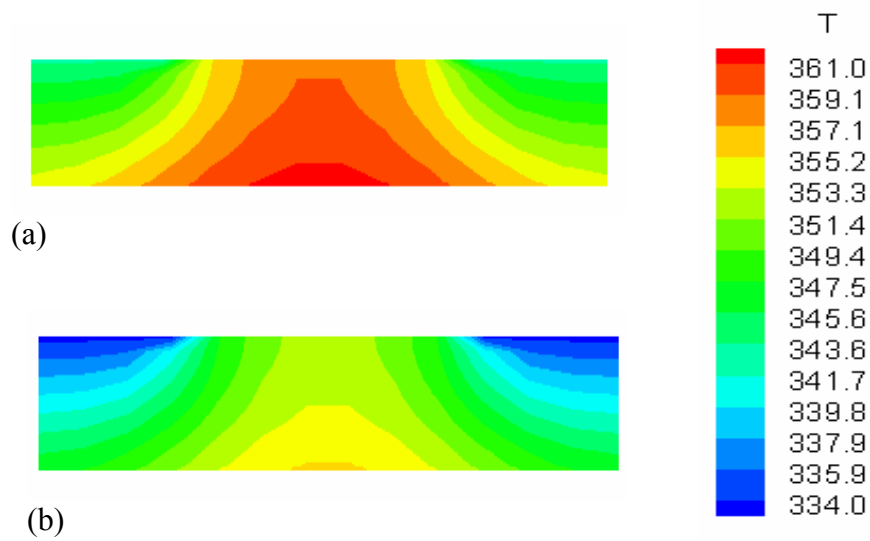


Fig. 3.11. Local temperature contours in cathode GDL at section of $x=0.025\text{m}$ with 353K anode temperatures and cathode temperatures (a) 343K (b) 333K

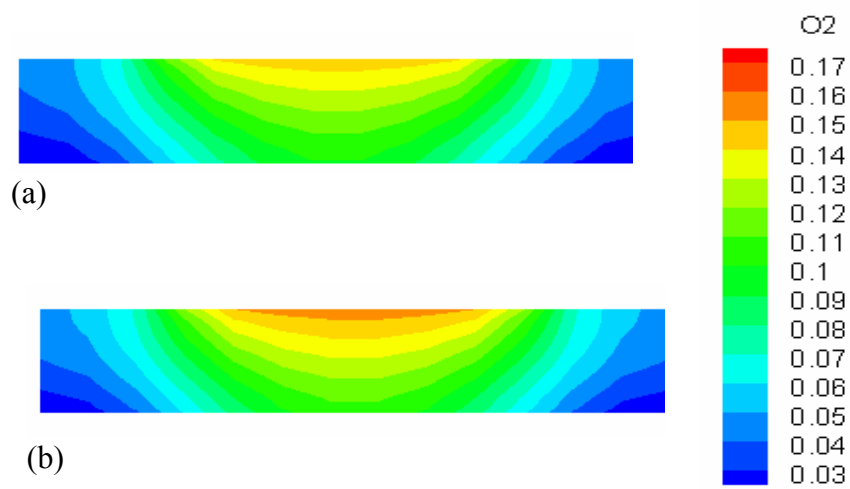


Fig. 3.12. Local oxygen mass fractions in cathode GDL at section of $x=0.025\text{m}$ with 353K anode temperatures and cathode temperatures (a) 343K (b) 333K

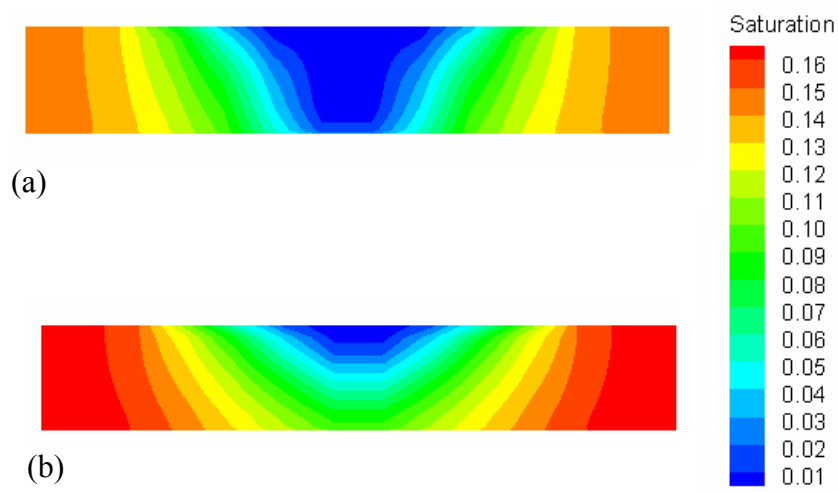


Fig. 3.13. Local water saturation in cathode GDL at section of $x=0.025\text{m}$ with 353K anode temperatures and cathode temperatures (a) 343K (b) 333K

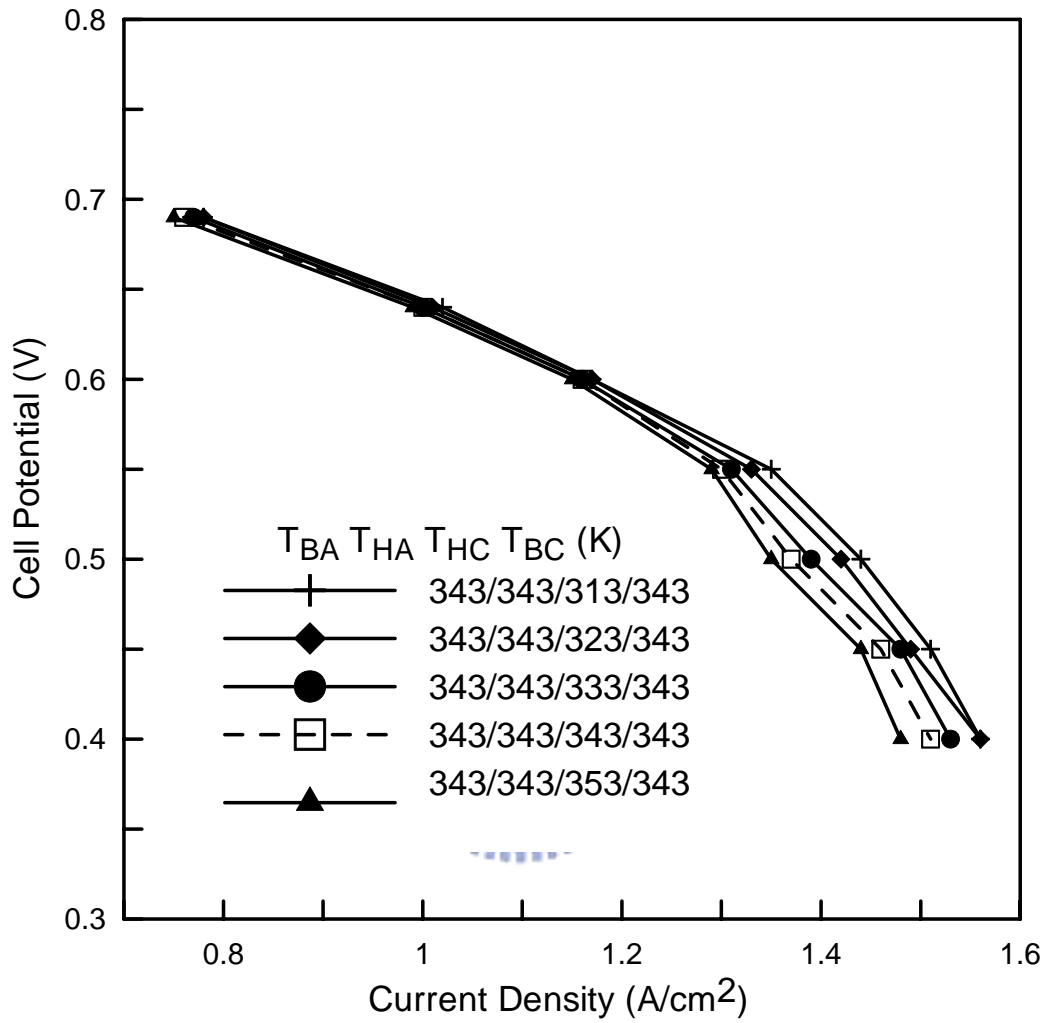


Fig. 3.14 Experimental results of Wang *et al.* (2003) on the effects of cathode humidification schemes. The cell temperature is set at 343K and the cathode humidification temperatures varied from 313K to 353K

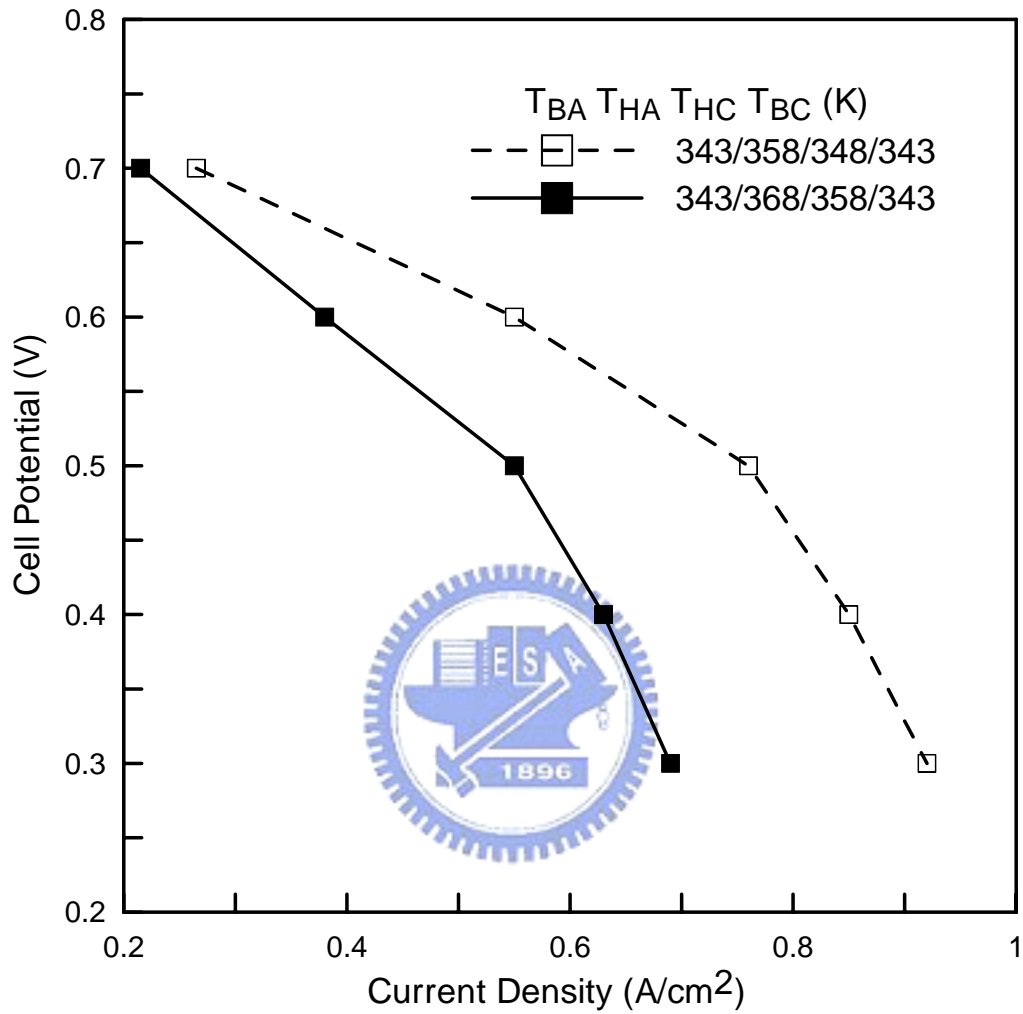


Fig. 3.15 Experimental results of Lee *et al.* (1999b) on the effects of anode and cathode enhanced humidification schemes. The cathode humidification temperatures vary from 348K to 358K while the anode humidification temperatures vary from 358K to 368K

CHAPTER 4

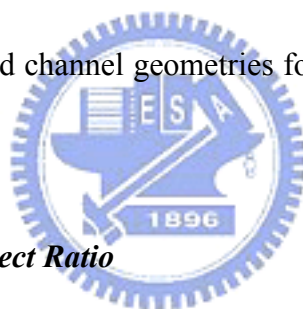
TRANSPORT COMPONENT DESIGN EFFECTS ON PROTON EXCHANGE MEMBRANE FUEL CELL PERFORMANCE

4.1 *Introduction*

As introduced in chapter 2, the main components of PEMFCs consist of bipolar plates, flow channels, gas diffusion layers, catalyst layers and membrane. Reactant gases and charged species move along individual route to complete the functions of electrochemical reaction as well as product discharge. In order to reach an optimal characteristic of the cell performance, it is vital to carefully examine the individual effects of transport component design. The most important issues are those which can evenly and efficiently deliver various species to the reaction sites, such that the cell can release the largest fraction of the chemical energy stored in the reactants. Meanwhile, the movement of the water vapor or liquid, product of cell reaction, is also essential because the transport passage could be clogged and the diffusion rate of reactants is reduced if no additional attention is addressed at high reaction rate condition. In this chapter, the influences of transport component design such as channel aspect ratio and GDL thickness are investigated and described in detail.

4.2 *Cell Performance Subjected to Transport Component Design*

Flow channel geometry is important for optimizing cell performance with delivery of sufficient reactant to the reaction sites. Various configurations with different channel aspect ratios are investigated to explore the effects of channel geometry design. The aspect ratio (AR) is defined as the height (in Z-direction) of the channel divided by the width (in Y-direction) of the channel. Channel height and width are modified according to the AR, such that the channel cross-sectional area is fixed. Hence, the reactant mass flow rate at the inlet and the channel hydraulic diameter are the same in all case studies. To maintain a fixed cell width, the shoulder width is also changed. Detailed channel geometries for each considered AR are listed in Table 4.1 and Fig.4.1..



4.2.1 Effect of Channel Aspect Ratio

Fig. 4.2(a) shows the relationships between output current densities and AR at moderate and low cell voltages. Clearly, cell performance dependence on the channel aspect ratio varies with operating conditions. The cell output current density is larger at moderate cell voltage and performance declines rapidly in the high reaction rate region, when the AR is large as in the case of 1.5. However, despite poor performance at cell potentials of 0.42V to 0.62V when the channel is flat, such as at AR =0.5, current density exceeds that obtained with other channel geometries at 0.14V.

4.2.2 Effect of Diffusion Layer Thickness


Figure 4.2(b) displays cell current density curves with five GDL thicknesses. A thinner diffusion layer is generally believed to reduce the reactant vertical diffusion path such that more oxygen arrives at the catalyst layer to gain more current. In contrast, cell performance varies with increased thickness of the diffusion layer because the reactant is transported through a longer distance and the flooding problem occurs. However, the data in Fig. 4.2(b) reveals that optimal thickness increases from 152 μm at 0.62V to 254 μm at 0.22V, beyond which potential, it decreases. The tendency is slightly different from the work of Jeng *et al.* (2004)] with a monotonously decreased performance when GDL thickness increases for a low - porosity GDL. By using a high-porosity GDL however, the trends coincide.

Fuel cell output is controlled by three degrading mechanisms- loss associated with reactant activation energy at the electrodes; loss associated with transport of the current in the electrically conducting media, and loss associated with the transport of reactant gases in the cell. These are called activation overpotential, ohmic overpotential, and concentration overpotential, respectively. The AR and GDL thickness influences relative magnitudes of these three irreversibilities according to the operating voltage, as is obvious from the data in Fig. 4.2. Local variations of these factors may also play an important role on the trend transition shown in the figure. A fixed cell overpotential is notably designated on the cathode BP surface in the present

study. The current conservation equation solution provides detailed information of potential distribution throughout the domain. Therefore ohmic overpotential and activation overpotential can be resolved and compared with the oxygen concentration for different operating voltage. Without generality loss, representative locations in the cell domain are assigned to investigate the effects of these two parameters and various transport properties on cell performance variation in the following sections.

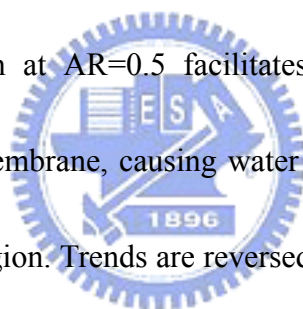
4.3 Local Properties Variations in Transverse Direction

4.3.1 Membrane Conductivity and Potential



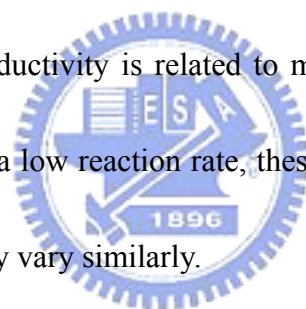
A series of demonstrations involving the most important transport quantities, such as phase potentials, reactant concentrations at selected locations, and cell voltages are performed to elucidate the cause of the forgoing results. All of the data are mirrored to yield results for a complete channel and a pair of half shoulders adjacent to the channel. Notably, the negatively charged electrons move from low potential to high potential and the positively charged proton move oppositely. The main concern in the potential variation discussion is that the passages with lowest electron potential increase from the cathode boundary, and the ionic potential decrease from the anode catalyst layer. Therefore, ohmic overpotential decreases, and the absolute value of the electrochemical reaction driving force, the activation

overpotential, in Eq. (14) increases. Fig. 4.3 plots and compares the membrane potential and conductivity in the transverse direction of the middle X-Y plane of the membrane for AR=0.5, 1, and 1.5, and cell voltages of 0.62V and 0.14V at Z-coordinate of 2.152mm. The short bars on the plot indicate the interfaces between channel and shoulder for each AR. At a cell voltage of 0.62V, the membrane conductivity patterns in the channel region and the shoulder differ, according to the AR value. At the membrane location of the channel region, conductivity is greater at a lower AR. Membrane conductivity is a function of water activity, so increasing the channel transverse dimension at AR=0.5 facilitates water transport at the anode through the channel to the membrane, causing water activity in the central region to exceed that in the shoulder region. Trends are reversed at the other AR values because of local current density effect. Membrane phase potential variations are strongly related to the conductivities; a lower conductivity is responsible for a larger membrane ohmic loss at a moderate reaction rate at which the local change in current density is expected to be small. However, the data in Fig. 4.3(b) indicate that at a high reaction rate, higher membrane conductivity locations exhibit a larger membrane ohmic loss because the local current density varies markedly at this cell voltage. The ohmic law and the fact that a large current density variation outweighs the trivial local



conductivity fluctuation demonstrate that ohmic loss in the membrane phase is consistent with local current density.

Figure 4.4 plots the membrane phase conductivity and potential at GDL thicknesses of 152 μm , 203 μm and 356 μm and cell voltages of 0.62V and 0.14V, to examine GDL thickness and cell voltage effects on the various transport properties. The data were obtained from the same position as in Fig. 4.2. A thick GDL stabilizes transverse variation of local conductivity. Reducing this parameter leads to a highly non-homogeneous local conductivity distribution at a cell voltage of 0.14V. The data in Fig. 4.4 indicates that conductivity is related to membrane potential in a manner similar to that in Fig. 4.3. At a low reaction rate, these two variables vary oppositely, but at a high reaction rate, they vary similarly.



4.3.2 Solid Phase Potential and Activation Overpotential


Solid-phase potential and activation overpotential in the transverse direction for various AR at the interface between the cathode catalyst layer and the GDL are described in Fig. 4.5. The data in Fig. 4.5(a) reveal that the shoulder area exhibits a small ohmic overpotential from the outer surface of the cathode BP. The longer electron passage in the catalyst layer beneath the channel region corresponds to greater potential variation on the way to this location. Consequently, the activation

overpotential absolute value in the shoulder region exceeds that in the channel region, indicating that the electrochemical reaction driving force is stronger there. This finding of non-uniform activation overpotential is consistent with that of Kulikovsky *et al.* (1999) and Sun *et al.* (2005b). Comparing the potential variation effects in the three selected designs of the channel AR, show that a slender channel design exhibits a smaller ohmic overpotential, and a larger absolute activation overpotential at all positions of interest. This result is explained by the wide electron transport passage along the shoulder height and the reduced average distance between the shoulders and the channel center, leading to a reduced current resistance. Variation of these two potentials at 0.14V appears initially to be similar to that in Fig. 4.5(a). The channel with AR =1.5 has a stronger driving force of electrochemical reaction in the shoulder region as it has the smallest membrane and solid phase ohmic overpotential compared to the other two channel designs.

Figure 4.6 compares the transverse variation in the solid phase potential and the activation overpotential at the location between the cathode GDL and the catalyst layer at three GDL thicknesses and two operating potentials. The GDL thickness effect on ohmic overpotential is clearly demonstrated in the data in Fig. 4.6(a). Despite the fact that the catalyst layer shoulder area exhibits minor ohmic overpotential in the design with a thickness of 152 μm , the potential increases

abruptly toward the channel central region, because the height and cross-sectional area of the electron transverse transport passage are small in this thinnest design. For the design with the thicker GDL, the larger ohmic overpotential in the catalyst layer shoulder region is problematic, but the moderate potential variation toward the central channel is advantageous. Accordingly, the activation overpotential variation exhibits the same tendency as that of the solid phase potential. These situations are similar at the two operating voltage, but the absolute values and variations are greater in the 0.14V case.

4.3.3 Water Saturation Level



Channel geometry effects on the transverse saturation level of the cathode GDL along the channel direction is presented in Figure 4.7. The flat channel advantage is evidenced by liquid water accumulation. The relatively short distance through which water is transported at AR=0.5 leads to the low saturation level in the channel direction even at a high reaction rate. That means the fast diffusion associated with the flat channel design causes the local partial pressure of water vapor to be low. In contrast, saturation level at the rear section of the channel with AR=1.5 is high, as the water vapor cannot easily escape from GDL under the shoulder. In this scenario, effective pore space in the porous medium is reduced considerably, and more mass

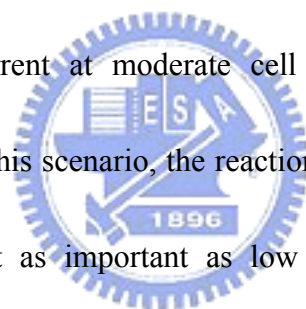
transport overpotential is activated, so cell performance is drastically degraded at low cell voltage.

Figure 4.8 plots the saturation level in the transverse direction of the cathode GDL at three positions $x=0.05\text{m}$, 0.025m and 0.045m , to elucidate GDL thickness effects on liquid water distribution. The plot demonstrates that the thinner GDL design has the lowest saturation level since water vapor produced in the cell reaction easily transports to the channel and outside the cell. On the contrary, the longer path and water vapor lower diffusion rate in the design with the $356\ \mu\text{m}$ -thick GDL results in greater water vapor concentration with a high probability of over-saturation and liquid water formation, contributing to concentration overpotential and performance reduction, especially at $x=0.45\text{m}$ at a cell potential of 0.14V .

Note that in the discussing of saturation level in the electrodes, the temperature field may also be an influential factor. At locations where the electrochemical reaction rate is high, the enthalpy as well as temperature increase accordingly. The higher temperature region corresponds to a greater saturation pressure of water and lower local partial pressure, causing a lower water saturation level. However, the high production rate of water vapor at this region causes a counter effect.

4.3.4 Oxygen Concentration and Current Density

Figure 4.9 depicts oxygen mass fraction distribution and local current density under the same condition and at the same location as in Fig.4.5. Intuitively, the flat channel supplies more oxygen to the catalyst layer and a high current density is expected. However, calculations reveal entirely different trends between channel and shoulder region catalyst layers. The design with $AR=0.5$ generates the lowest local current density in the channel region, despite its having the largest oxygen mass fraction, and the expected relationship between reactant concentration and the reaction rate is not observed except at the shoulder center. On average, the slender design with $AR=1.5$ generates more current at moderate cell voltage. This phenomenon is explained by the fact that in this scenario, the reaction is relatively slow and the high reactant concentration is not as important as low ohmic overpotential and high activation overpotential provided by slender channel geometry such as $AR=1.5$. This design has a wider rib zone than those of other designs, providing a small increase and variation in the solid phase potential as well as large absolute activation overpotential, causing high current density and favorable cell performance. At a high reaction rate as shown in Fig. 4.9(b), the dominant mechanism of local current density transits from electric potential at the channel region, to oxygen concentration at the shoulder region at $AR=1.5$. This transition is also found when $AR=1$. The design with $AR=0.5$ exhibits the same local current density variation trend as in the case of 0.62V. At $AR=1.5$, a

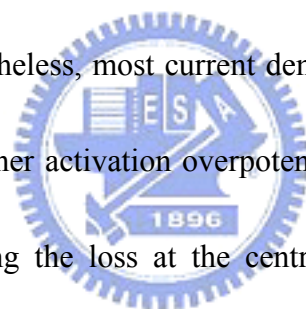


high reactant concentration need outweighs a high activation overpotential need, so the expected relationship between the concentration and the local reaction rate appears earlier. The large shoulder area width hinders reactant transport, resulting in a relatively low level of local oxygen mass fraction and a sharp decline in the local current density under the shoulder area. In contrast, the sufficient oxygen provided by the flat channel such as $AR=0.5$ causes most of the region to exhibit a potential controlled state and on average, produces a greater current than that generated by other designs.

GDL thickness effects on transverse distribution of oxygen concentration and current density is plotted in Fig. 4.10. Exhibiting a trend opposite to that of the potential, a thinner GDL provides more oxygen to the channel region catalyst layer.

The thickest design is associated with a greater concentration in the shoulder region. These variations are related to the vertical depth and transverse cross-section of reactant delivery. In the case in which GDL thickness is $152\mu\text{m}$, the vertical path is short and oxygen concentration is high at the catalyst layer beneath the channel. Nevertheless, the transverse transport cross-section is reduced and oxygen concentration falls substantially at the shoulder region. With reference to local current density distribution, mechanisms of activation overpotential mechanism and oxygen concentration have different effects in different regions. The activation overpotential

dominates the reaction in the catalyst layer under the channel region because oxygen concentration fulfills the requirement for electrochemical reaction. Accordingly, the current density trend is consistent with that of the activation overpotential throughout the entire region in the 356 μm case and in most of the region in the 203 μm and 152 μm cases at 0.62V. A peak point in the concave pattern of the local current density appears only near the central shoulder region in the 152 μm cases, suggesting that from this point to the central shoulder, oxygen deficiency forces the current density to drop according to the oxygen mass fraction, and local performance is dominated by oxygen concentration. Nevertheless, most current density gain in the shoulder region catalyst layer arises from higher activation overpotential for the design with the 152 μm -thick GDL, compensating the loss at the central region and generating more current than other designs at 0.62V.



Similar result can be found in the work of Sun *et al.* [2005b] which investigated the GDL thickness effects at total cell overpotentials of -0.4V, -0.5V and -0.6V. The thinner GDL thickness design exhibits the slowest reaction rate at the catalyst site under the channel region. This phenomenon was interpreted by a longer electron traveling length to the channel region than to the shoulder region, such that fewer electrons would participate in the electrode reaction in the region under the channel.

At a high reaction rate with a cell voltage of 0.14V as shown in Fig. 4.10(b), oxygen concentration is lower than in Fig. 4.10(a) because the reaction rate is higher, but transport depth and transverse cross-section effects on oxygen concentration are the same. However, local current density distributions exhibit quite different patterns. The plot depicts clear peak points in the concave pattern for all three GDL thicknesses. As stated previously, the 356 μm design generates more current than the other two designs at the central channel region catalyst layer because the activation overpotential dominates the reaction. This situation changes rapidly toward the shoulder region since oxygen concentration is extremely low. The figure also shows that the peak current density points move near the shoulder in the remaining two cases. A thinner GDL corresponds to a latter peak point from the channel central and a larger peak current density. Beyond these points, current density variation is nearly the same as oxygen concentration. At the peak points, the design with the 152 μm -thick GDL clearly has the largest local current density; unfortunately, oxygen concentration falls sharply toward the shoulder center and current density is the lowest of the three designs. Consequently, the 152 μm -thick case does not exhibit the best cell performance. On the other hand, despite the fact that the 203 μm -thick design has a moderate local current density output at the channel center, peak point, and shoulder center, its local current density curve envelopes the largest area with the x-y plane and

becomes the optimal GDL thickness at low cell voltage. This finding is quite different from the result of Sun *et al.* (2005b) that no significant variation of average current density was found when GDL thickness reduced from 0.35 to 0.15 mm. The discrepancy may be attributed to different operating conditions or cell geometries between these two models.

4.4 Vertical Distributions of Velocity and Oxygen Concentration

In order to obtain a further insight of the transport process in the PEMFCs, vertical distributions of axial velocity and oxygen concentration in cathode channel and GDL are shown in Fig. 4.11 for AR values of 0.5 and 1.5. The data are extracted from central point of X-Y plane. This plot demonstrates the fact that the main transport mechanism in channel is the convection, such that the velocity profile exhibits a fully developed pattern. However, in GDL region, the fluid velocity is extremely small but the oxygen concentration varies significantly toward CL, meaning that diffusion is the primary way of mass transfer. Comparing the oxygen concentration at interface of GDL and CL between these two figures reveals the fact that a flat channel design such as AR=0.5 is capable of providing higher concentration of oxygen as the vertical diffusion path is shorter than that of AR=1.5. When channel height remains constant and GDL thickness varies, similar results can be seen as

shown in Fig. 4.12. The variation trends of these two variables have the same tendency comparing with that in Fig. 4.11. When the GDL thickness is small, vertical diffusion path is short and more reactant gas can be delivered to the reaction sites. Another finding from these figures is that the slopes of the oxygen concentration are different between operating conditions of 0.22V and 0.62V. At 0.22V, it demonstrates a serious decay toward the CL. This is due to the reason that the cell reaction is strong and the oxygen consumes at a larger rate than that at 0.62V. Therefore, the magnitude of oxygen concentration is also smaller at 0.22V.

4.5 *Effect of Operating Temperature*

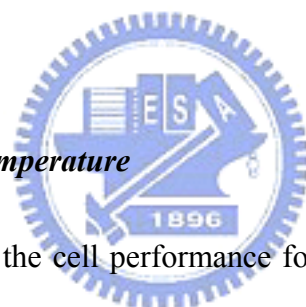


Figure 4.13 compares the cell performance for various channel geometries at three different operating temperatures 353K, 343K and 333K. According to the findings in chapter 3, the cell temperature has a close connection to the membrane conductivity; therefore, its effect on cell performance is obvious at medium reaction rate where ohmic loss dominates the cell reaction. Consequently, at cell voltage of 0.62V the cell output current density increases as the temperature increases, no matter what the channel geometry is. However, at a higher reaction rate, the cell output current density does not vary significantly when the cell temperature changes. In particular, when AR is greater than 1.25 and cell voltage is 0.22V, there is no obvious

change in output current density. This is attributed to the fact that for such a channel shape, reactants are not easy to reach the CL under the shoulder region; therefore, the concentration overpotential overcomes the merits of higher membrane conductivity arising from greater cell operating temperature.

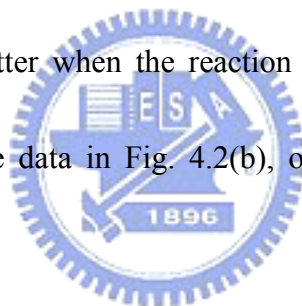
Similar phenomena can also be found in Fig. 4.14 where temperature effect for five different GDL thicknesses is presented. At a medium reaction rate, cell performance increases monotonically according to the increase of cell temperature and to the decrease of GDL thickness. This is mainly due to the improvement of the transport of either electrons or ions. Therefore, the ohmic overpotential is improved. At 0.62V, the situation is more involved and an optimum GDL thickness exists according to the cell temperature. As indicated in previous section, a thinner GDL thickness design is able to offer sufficient oxygen concentration at region under the channel but the transverse transport section area reduces accordingly such that the reaction sites under the shoulder are not easy to access enough reactant gases. A close examine of Fig. 4.13 shows that at this operating voltage, optimal GDL thickness shifts toward thinner design when cell operating temperature decreases. This can be explained by the fact that at a lower operating temperature, cell reaction rate is not reduced and the ohmic overpotential has a greater contribution to the cell performance. Consequently, the design of GDL thickness which is able to generate greater current

density shifts toward a thinner value because it is beneficial for the electron transport and the ohmic overpotential is decreased.

4.6 Tendency Comparisons with Previous Works from Literature

The transport phenomena of various species in PEMFCs and the competition effect between electrons and reactant gas are elucidated in this chapter. Contrary to the earlier investigation, current modeling results on the transport component design effects show that the peak point of local current density is not located at the middle of channel but moves around shoulder and channel regions of the CLs. This phenomenon is explained by the combined effort of reactant concentration and activation overpotential that appeared in the Butler-Volmer equation. Similar results can be found in the works of Sivertsen (2005) and Meng (2004). As regards the comparison with experimental results, literature survey shows that there is few experimental works concerning the polarization curves for the effects of AR and GDL thickness. The work of Lee *et. al.* (1999a) on the effects of compression and gas diffusion layers may provide a clue to examine the effect of GDL thickness. Fig. 4.15 shows their experimental work of cell performance subjected to three different screw compression forces by using the ELAT GDL which is a flexible material. From the principle of material mechanics, material with lower compression force corresponds to a larger

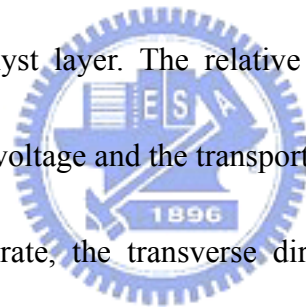
dimension and vice versa. Therefore, this figure may be employed to the examination of GDL thickness effects. The data show that when the bolt torque is 100in-lb, which corresponds to the thickest GDL, the cell current density is the smallest at each operating voltage. This is consistent with current modeling result in Fig. 4.2(b) that the 352 μm GDL design has the worst performance for every cell voltage. Furthermore, experimental results of 125 and 150 in-lb bore torques reveal that the better performance case is dictated by the operating condition. At cell voltage of 0.7V, the cell with 150 in-lb bore torque exhibits greater current density and that with 125 in-lb bore torque behaves better when the reaction rate increases. Apparently, this tendency is coincide with the data in Fig. 4.2(b), offering a strong support of the reliability of current work.



4.7 Summary

A multi-dimensional, multi-component, computational fluid dynamic model has been employed to elucidate transport phenomena and electrochemical reaction in PEMFCs. Two important transport component design parameters - channel aspect ratio and GDL thickness, are investigated in detail. The simulation and discussion support the following conclusions:

1. The designs of channel aspect ratio and GDL thickness affect the physical property distributions. At a high reaction rate, these two parameters have a strong influence on cell performance.
2. Three mechanisms of cell irreversibility are resolved locally from the model and are considered to determine variation in the macroscopic cell current density and performance.
3. Transverse current density distribution is governed by both electron conduction and activation overpotential in channel region or by reactant concentration in shoulder region of catalyst layer. The relative strengths of these two factors depend on the operating voltage and the transport geometry.
4. At a moderate reaction rate, the transverse direction current density in most regions is a convex function of position and is influenced by solid phase potential and activation overpotential, making the peak point of the concave pattern current density either close to the shoulder region or non-existent. Thus, a geometry design that facilitates electron transport such as a large channel aspect ratio or a thin GDL thickness causes a relatively larger current in the catalyst layer.
5. At a low cell voltage, the largest reaction rate location is close to the channel center, therefore, the electrochemical reaction in the majority regions is



dominated by the reactant transport and a smaller channel aspect ratio design is preferred.

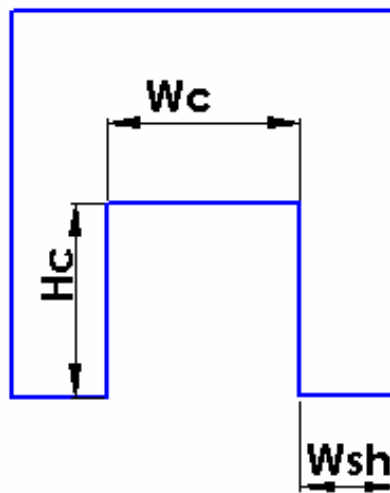
6. Large GDL thickness positively increases oxygen transport under the shoulder region; therefore output current density elevates according to cell voltage decrease. However, at the lowest considered cell voltage of 0.14V, oxygen deficiency caused by long traveling length and liquid water clogging effect reverses this relationship.

7. Plots of axial velocity and oxygen concentration in cathode vertical direction indicate that the main mass transport mechanism in channel is the convection and that in electrode is the diffusion. Therefore, vertical distance change arising from the variation of channel aspect ration and GDL thickness cause a marked difference of oxygen concentration level at cathode CL.

8. The operating temperature has a positive effect on cell performance for various cases of transport component designs considered in this study at medium cell voltages due to its improvement of ohmic overpotential. However, this phenomenon is not sensible at high reaction rates for the design with a higher AR or GDL thickness as the concentration overpotential smears the effect of the higher operating temperature.

Table 4.1 Channel and shoulder geometries for various ARs (unit: mm)

AR	Channel Height (Hc)	Channel Width (Wc)	Half Shoulder Width (Wsh)
0.5	0.57	1.14	0.23
0.75	0.69	0.92	0.34
1	.080	0.80	0.40
1.25	.089	0.72	0.45
1.5	0.98	0.66	0.47



$$AR = Hc / Wc$$

Fig. 4.1 Definition of channel aspect ratio AR

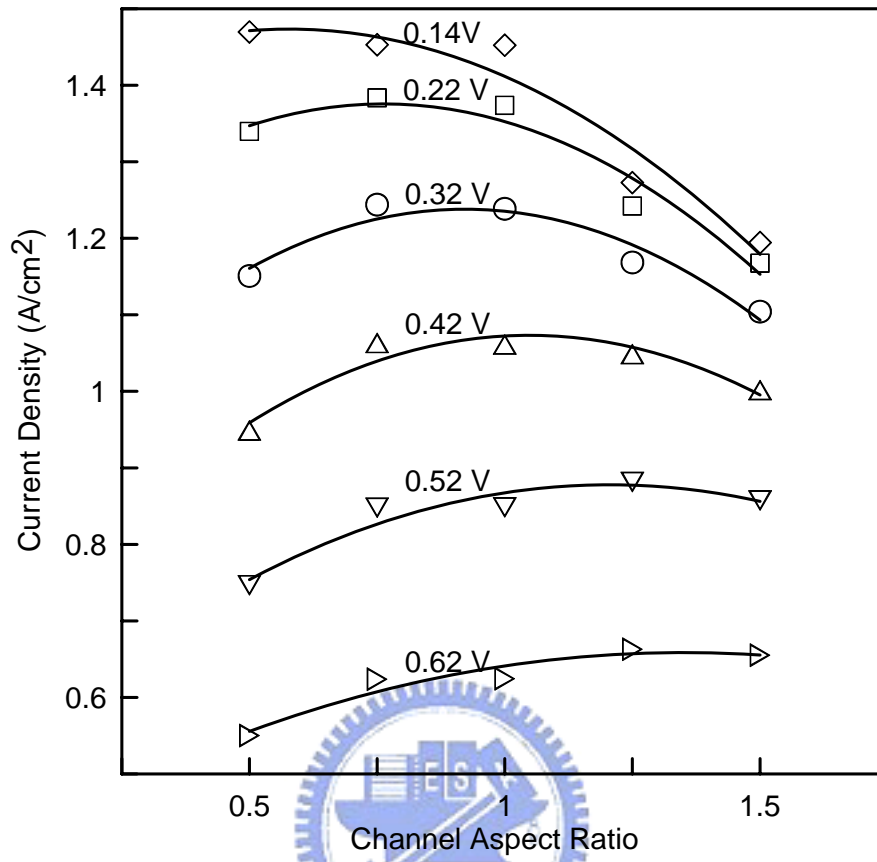


Fig. 4.2(a) Current density distribution at various cell voltages as function of AR

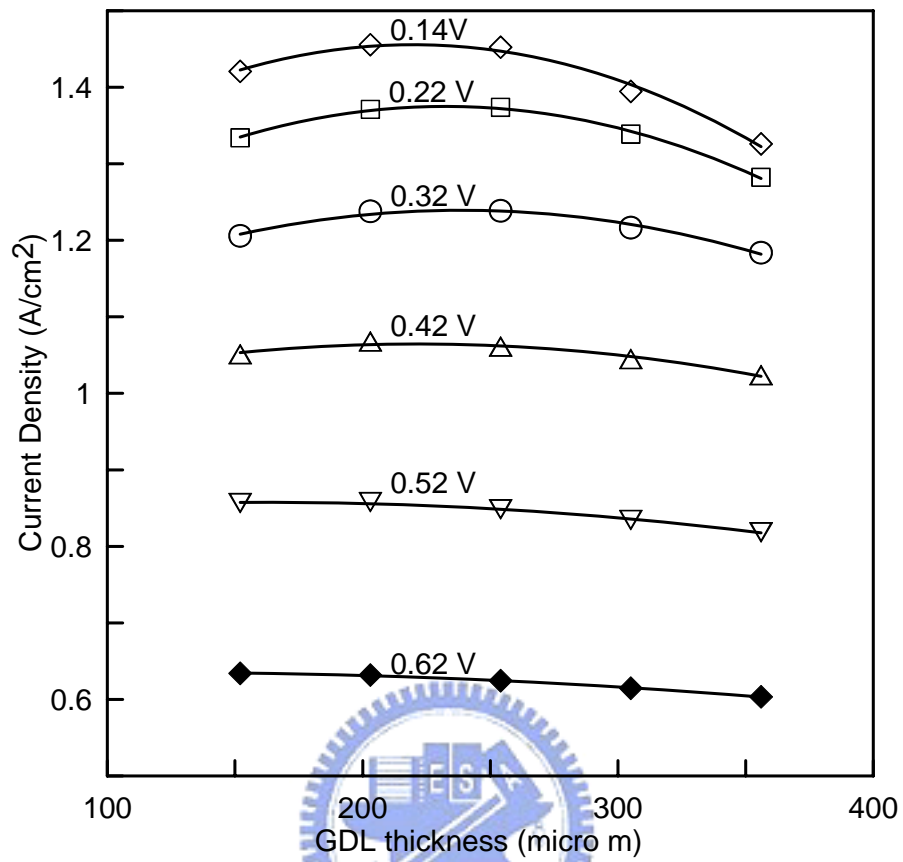


Fig. 4.2(b) Current density distribution at various cell voltages as function of GDL thickness

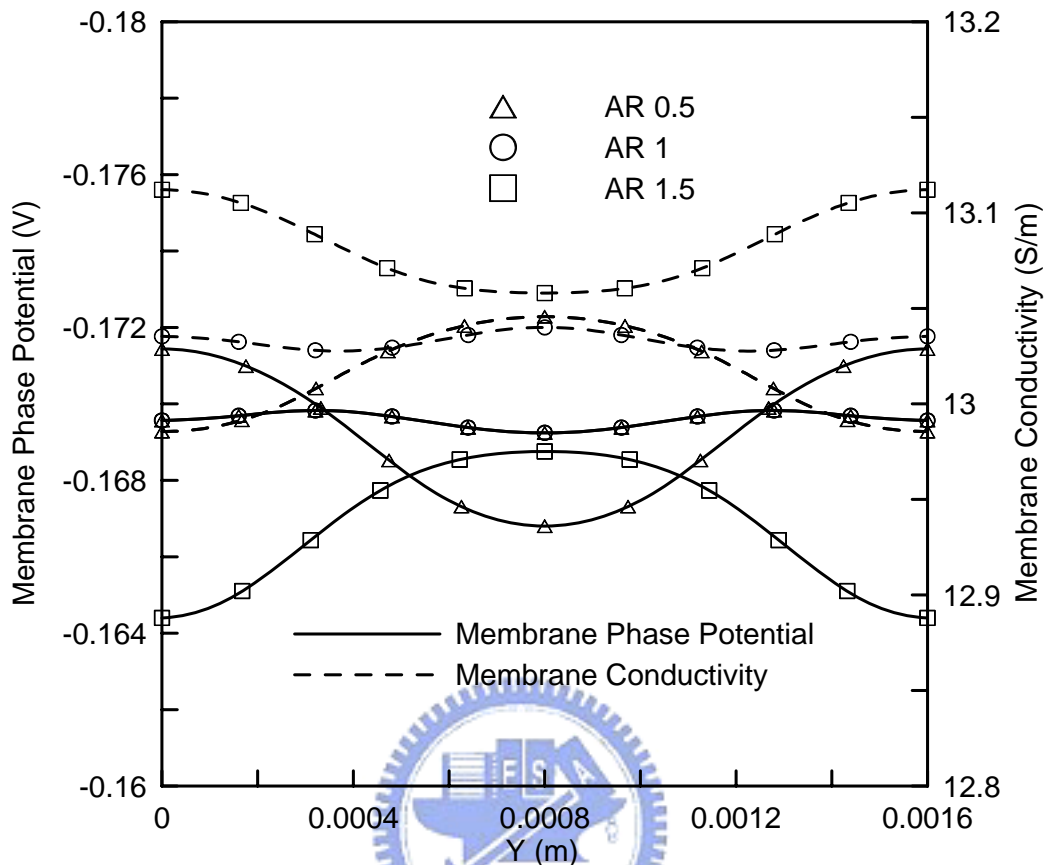


Fig. 4.3(a) Distributions of potential and conductivity of membrane in the transverse direction of the middle X-Y plane for three values of AR at cell voltages of 0.62V

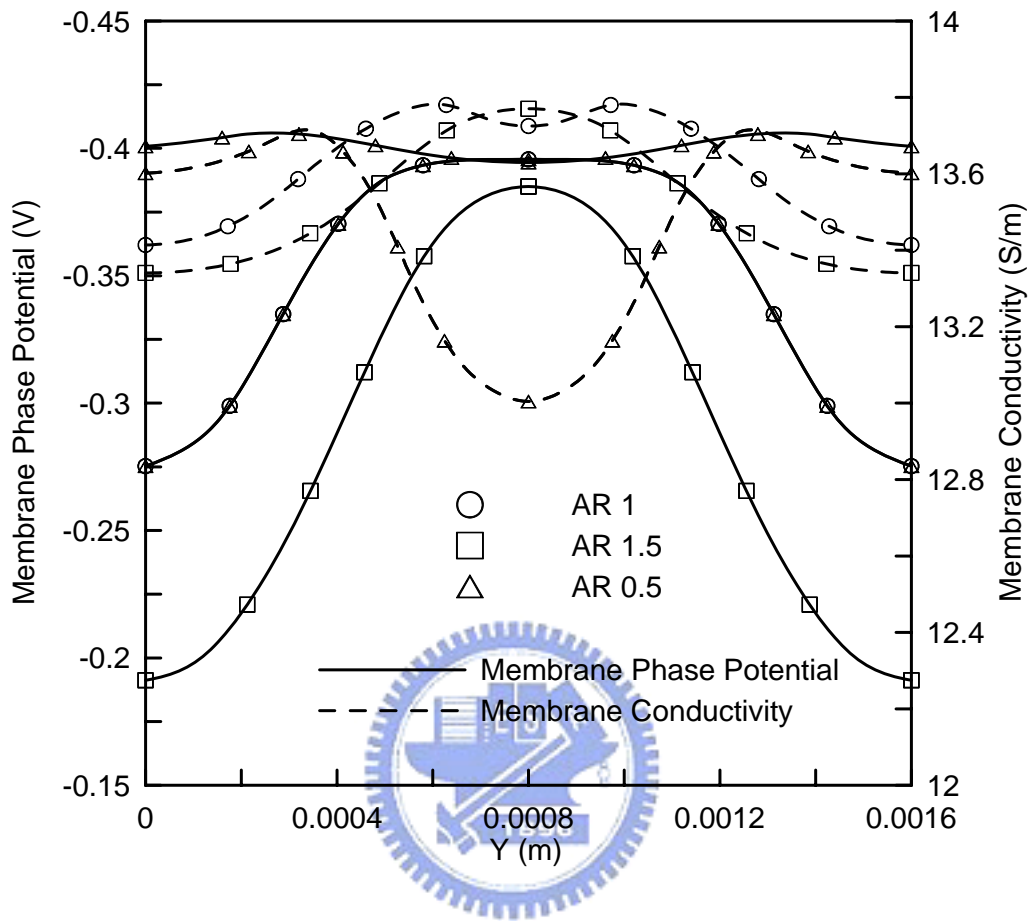


Fig. 4.3(b) Distributions of potential and conductivity of membrane in the transverse direction of the middle X-Y plane for three values of AR at cell voltages of 0.14V

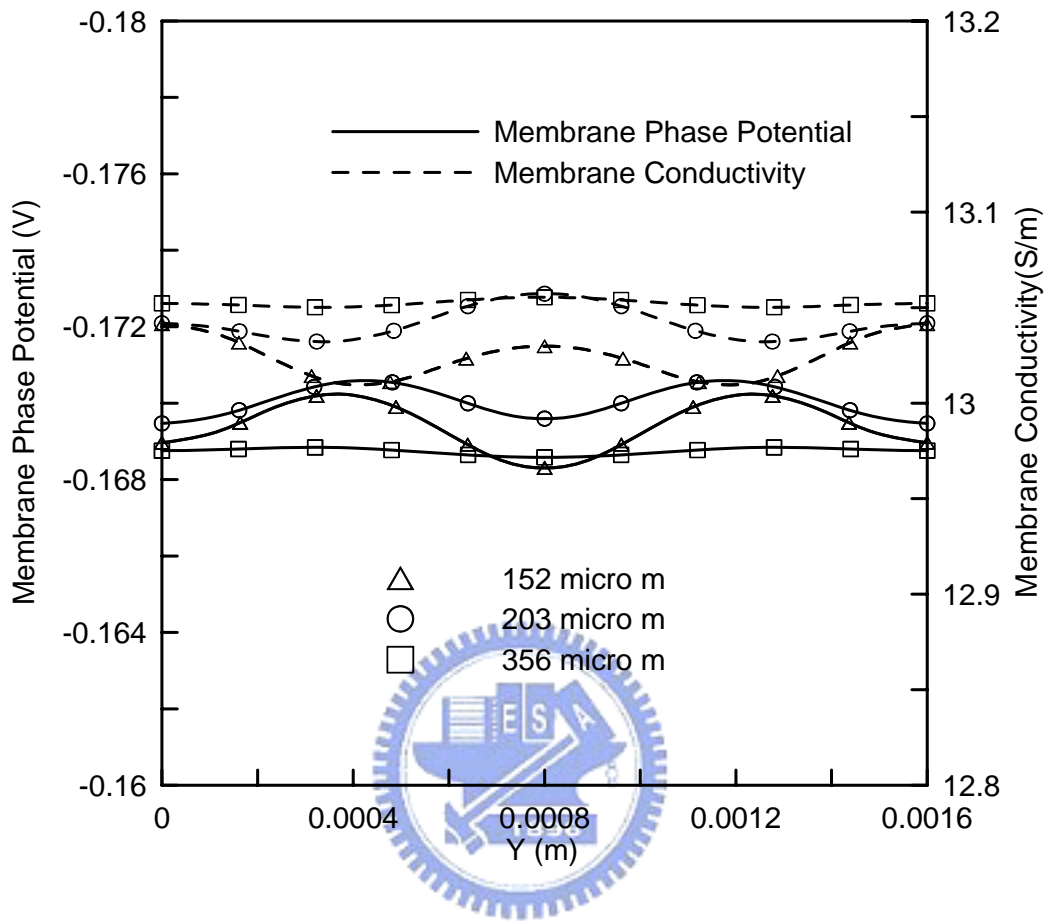


Fig. 4.4(a). Distributions of potential and conductivity of membrane in the transverse direction of the middle X-Y plane for three values of GDL thickness at cell voltage of 0.62V

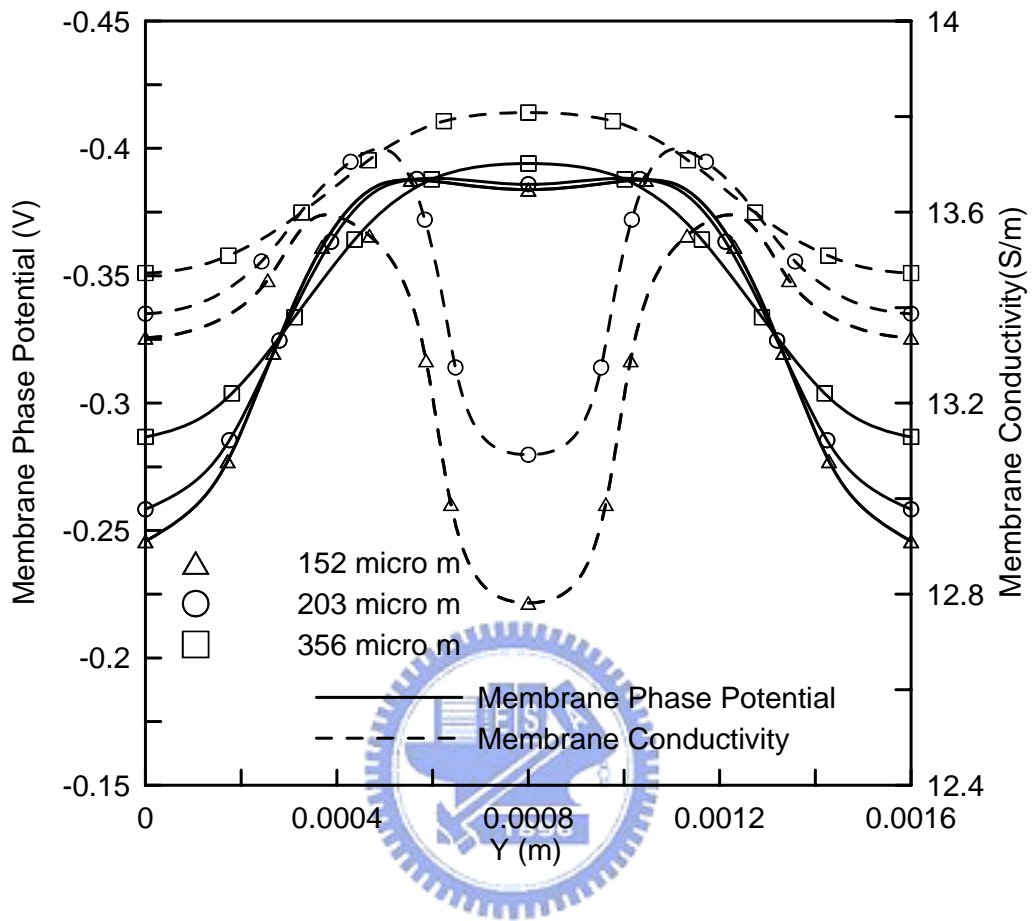


Fig. 4.4(b). Distributions of potential and conductivity of membrane in the transverse direction of the middle X-Y plane for three values of GDL thickness at cell voltage of 0.14V

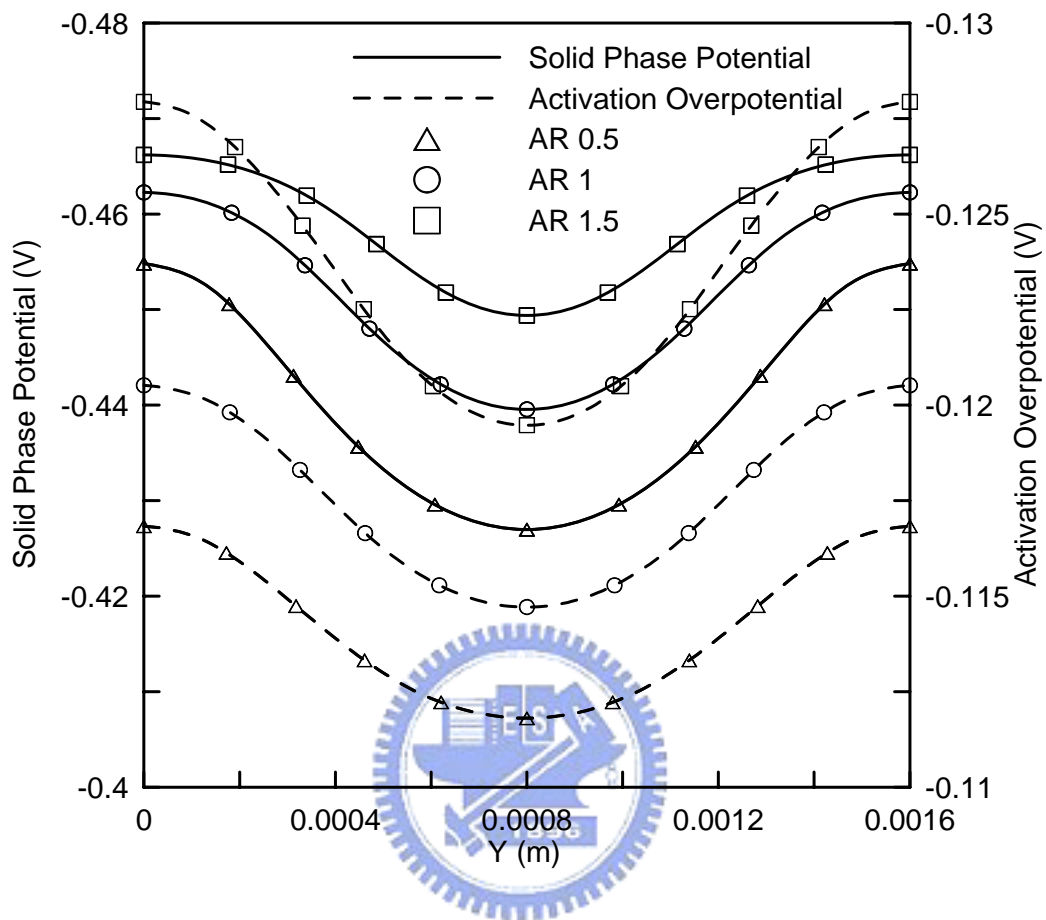


Fig. 4.5 (a). Transverse distributions of solid phase potential and activation overpotential at the interface between the cathode catalyst layer and the GDL for three values of AR at cell voltage of 0.62V

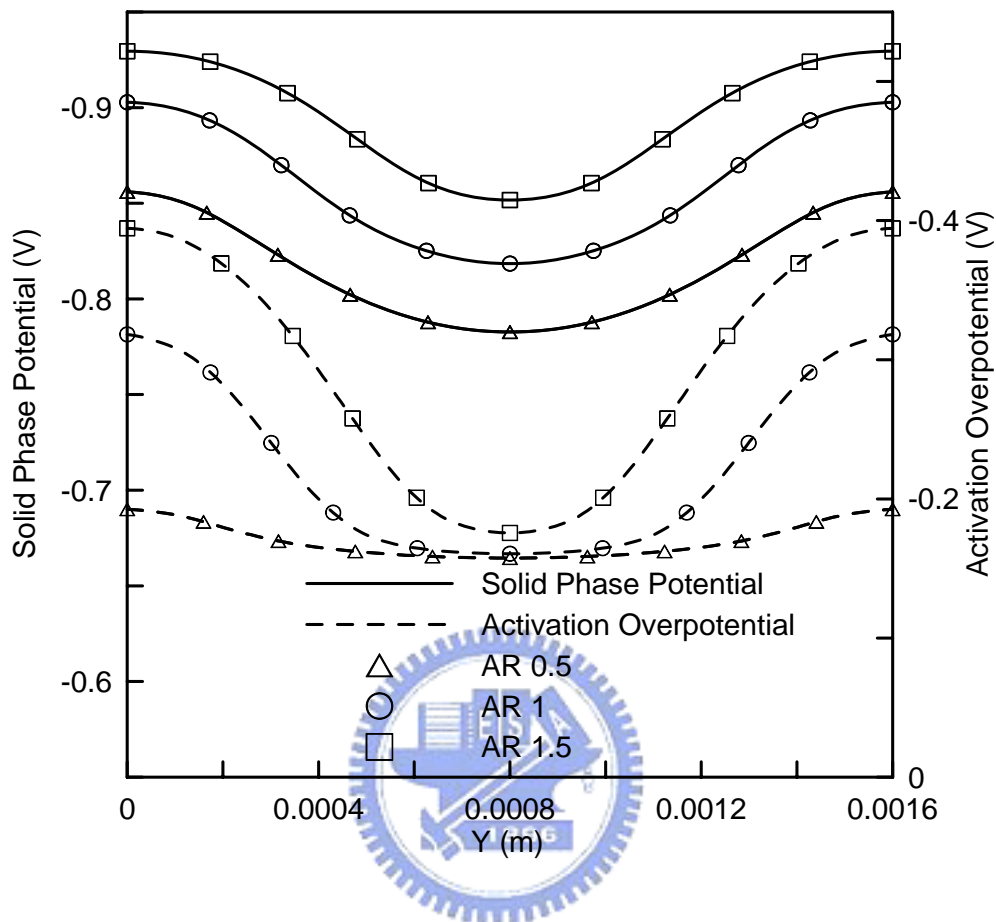


Fig. 4.5 (b). Transverse distributions of solid phase potential and activation overpotential at the interface between the cathode catalyst layer and the GDL for three values of AR at cell voltage of 0.14V

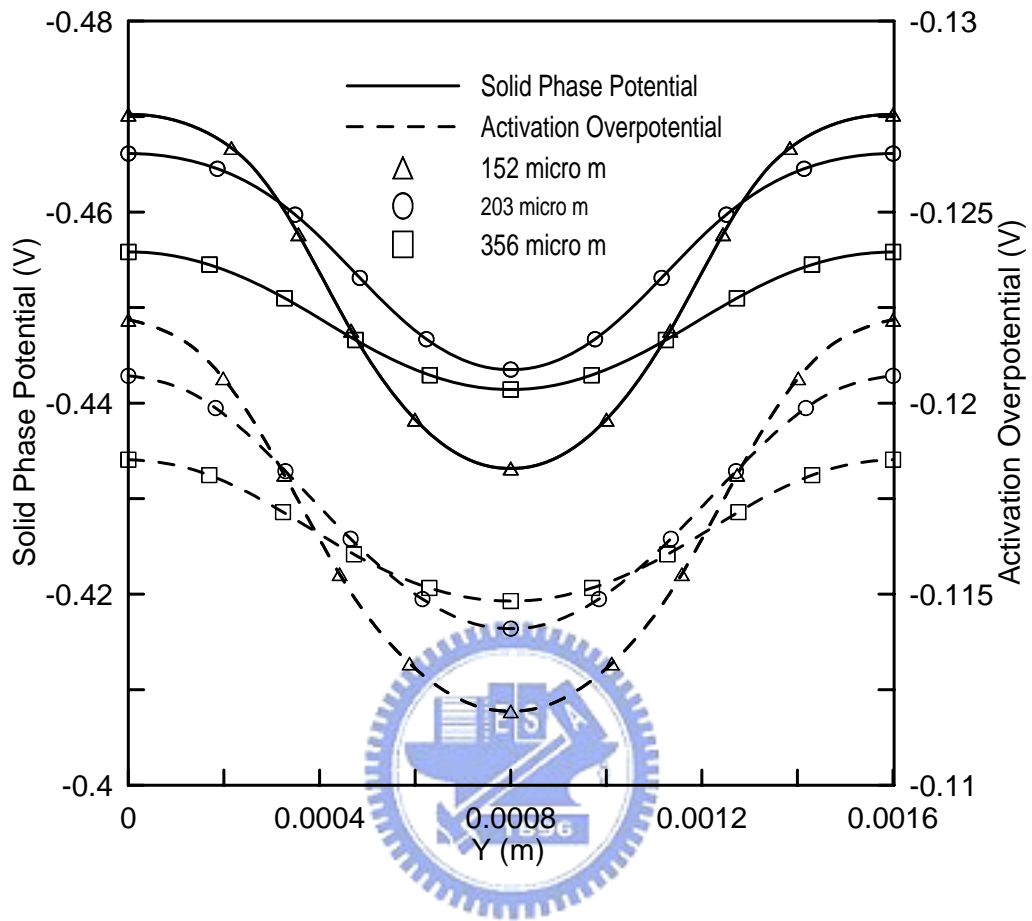


Fig. 4.6 (a). Transverse distributions of solid phase potential and activation overpotential at the interface between the cathode catalyst layer and the GDL for three GDL thicknesses at cell voltage of 0.62V

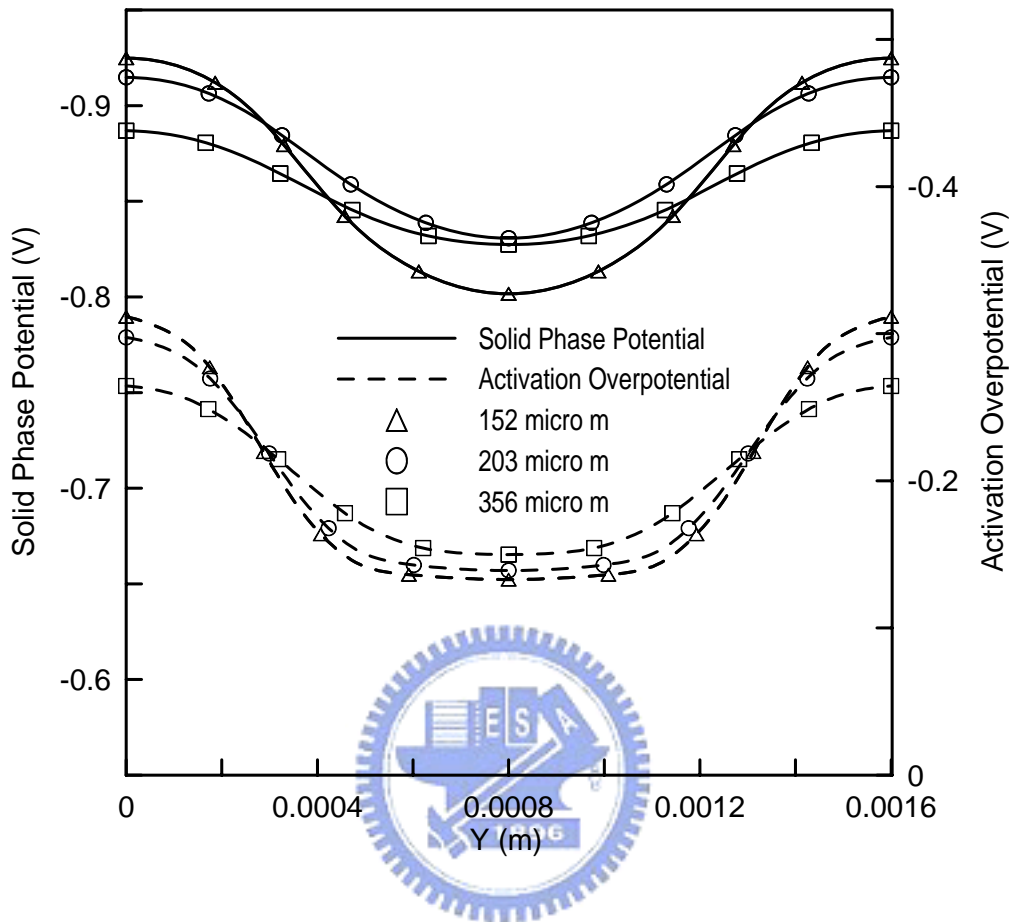


Fig. 4.6(b). Transverse distributions of solid phase potential and activation overpotential at the interface between the cathode catalyst layer and the GDL for three GDL thicknesses at cell voltage of 0.14V

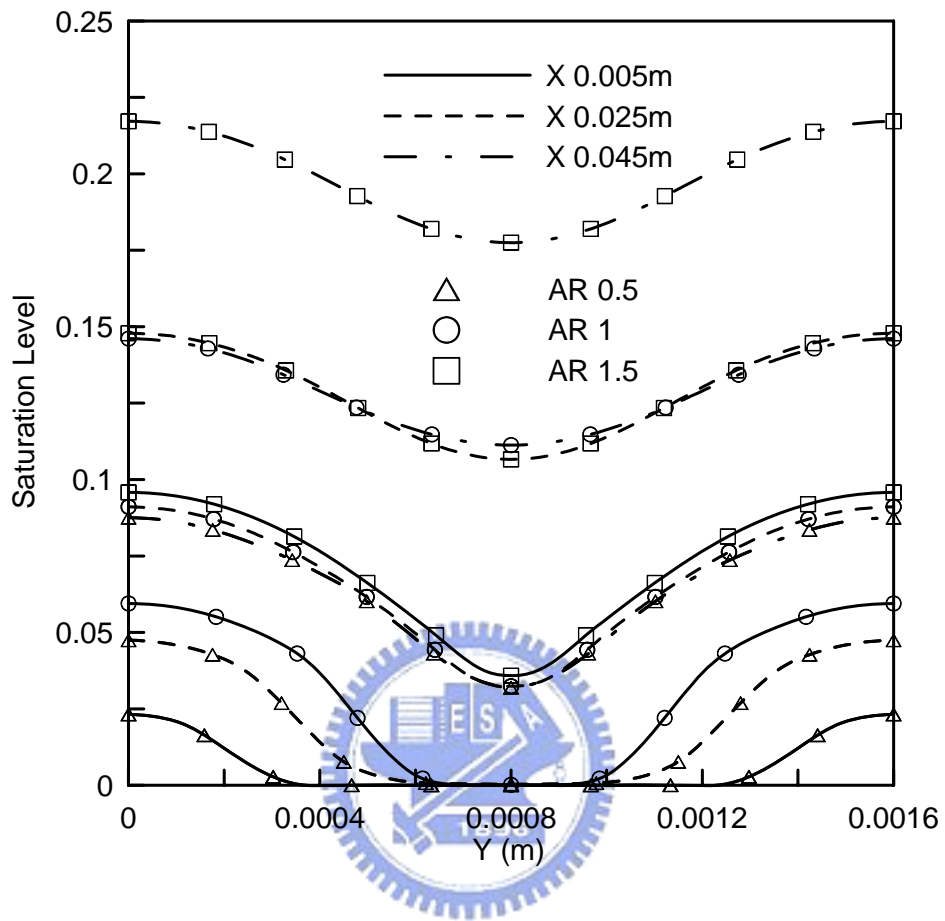


Fig. 4.7(a). Effect of channel aspect ratio on transverse water saturation of the cathode GDL along channel direction at cell voltage of 0.62V

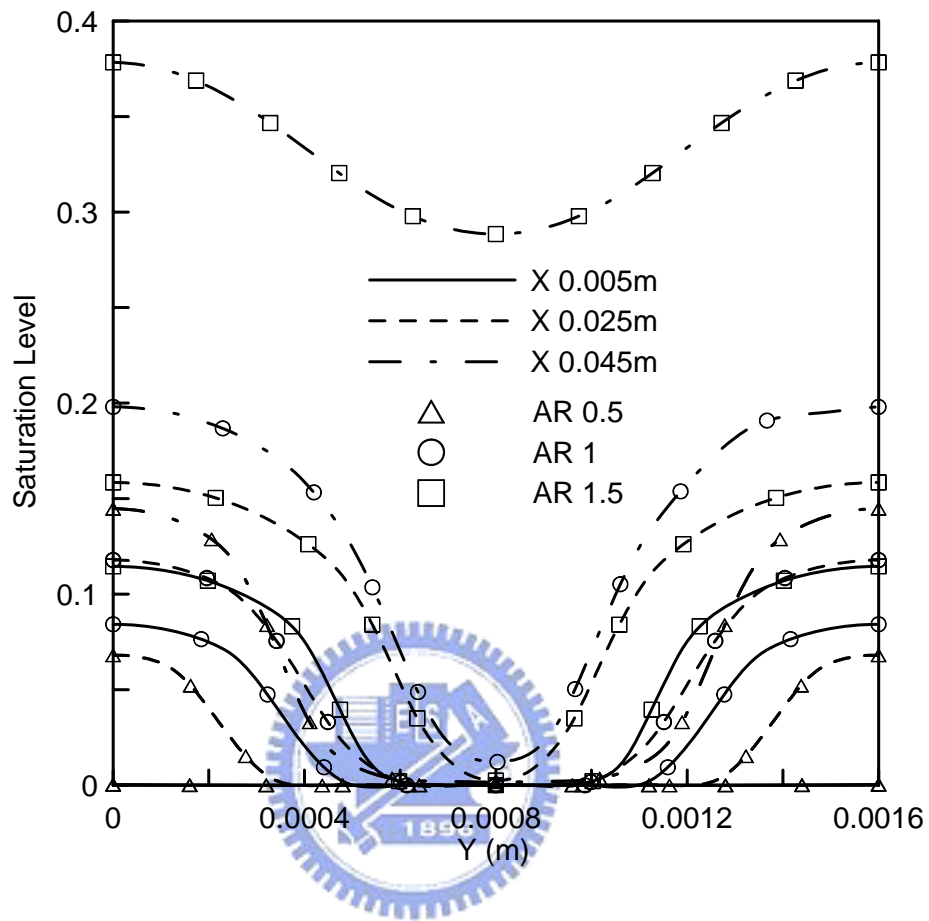


Fig. 4.7(b). Effect of channel aspect ratio on transverse water saturation of the cathode GDL along channel direction at cell voltage of 0.14V

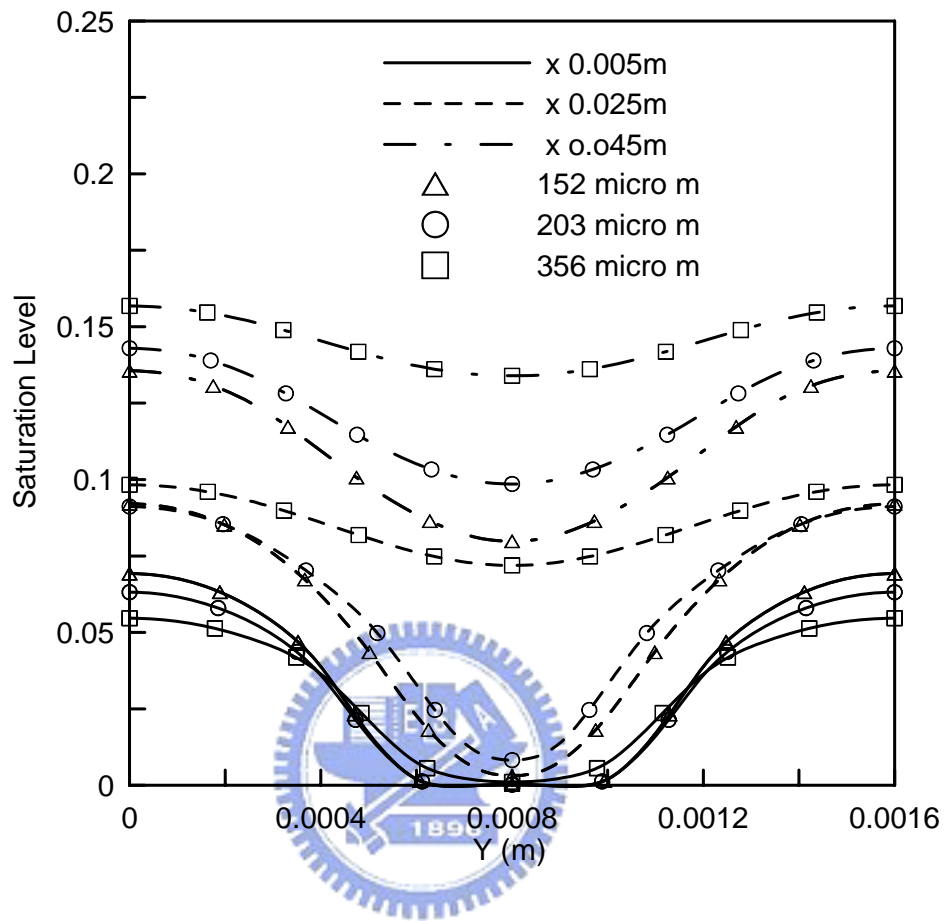


Fig. 4.8(a). Effect of GDL thickness on transverse water saturation of the cathode GDL along channel direction at cell voltage of 0.62V

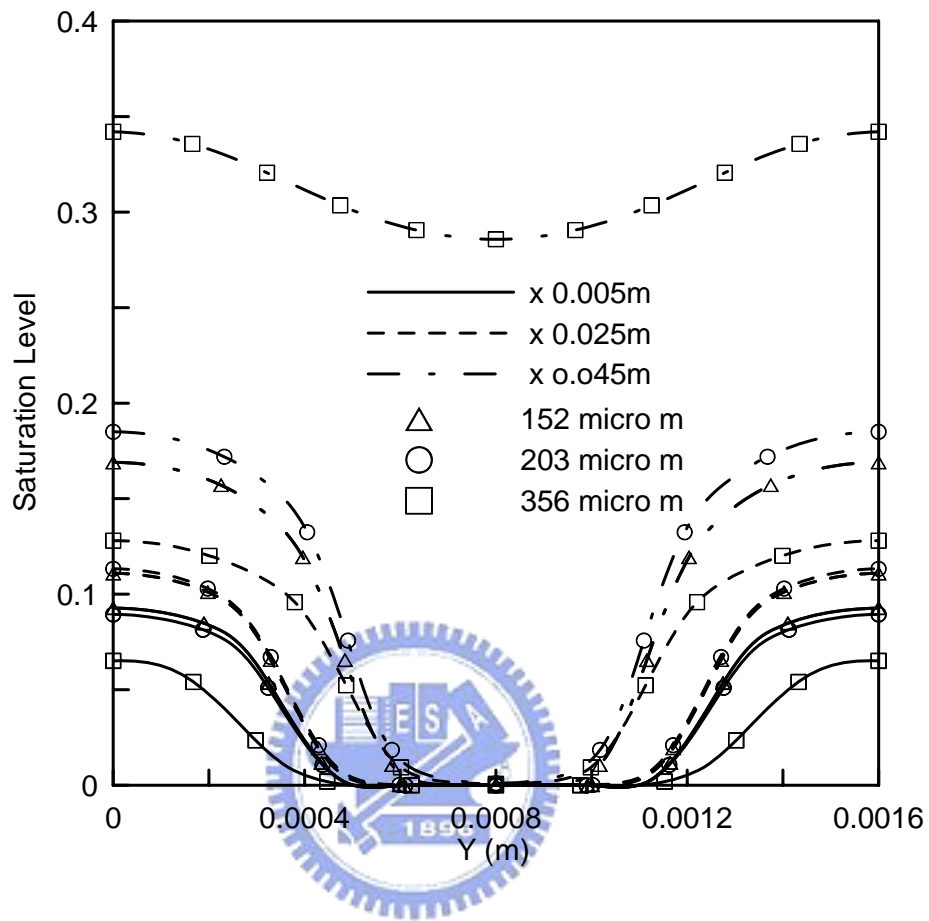


Fig. 4.8(b). Effect of GDL thickness on transverse water saturation of the cathode GDL along channel direction at cell voltage of 0.14V

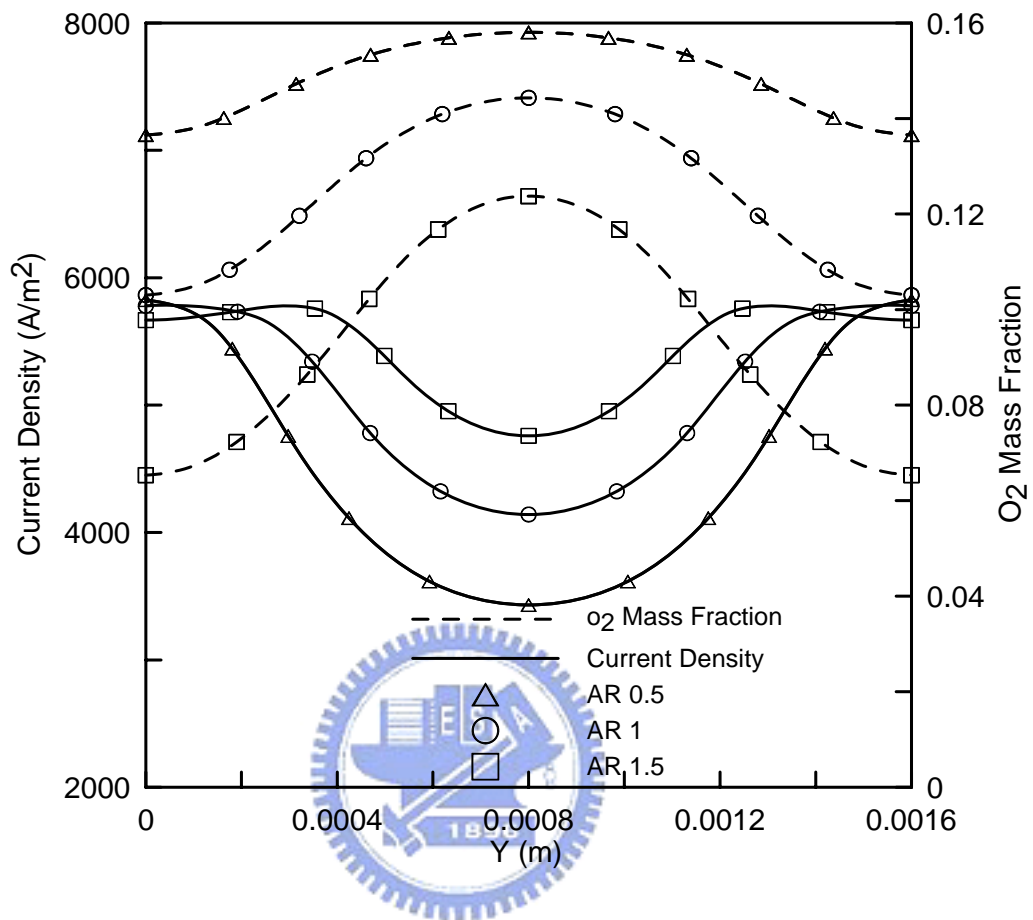


Fig. 4.9(a). Transverse distributions of oxygen mass fraction and local current density at the interface between the cathode catalyst layer and the GDL for three values of AR at cell voltage of 0.62V

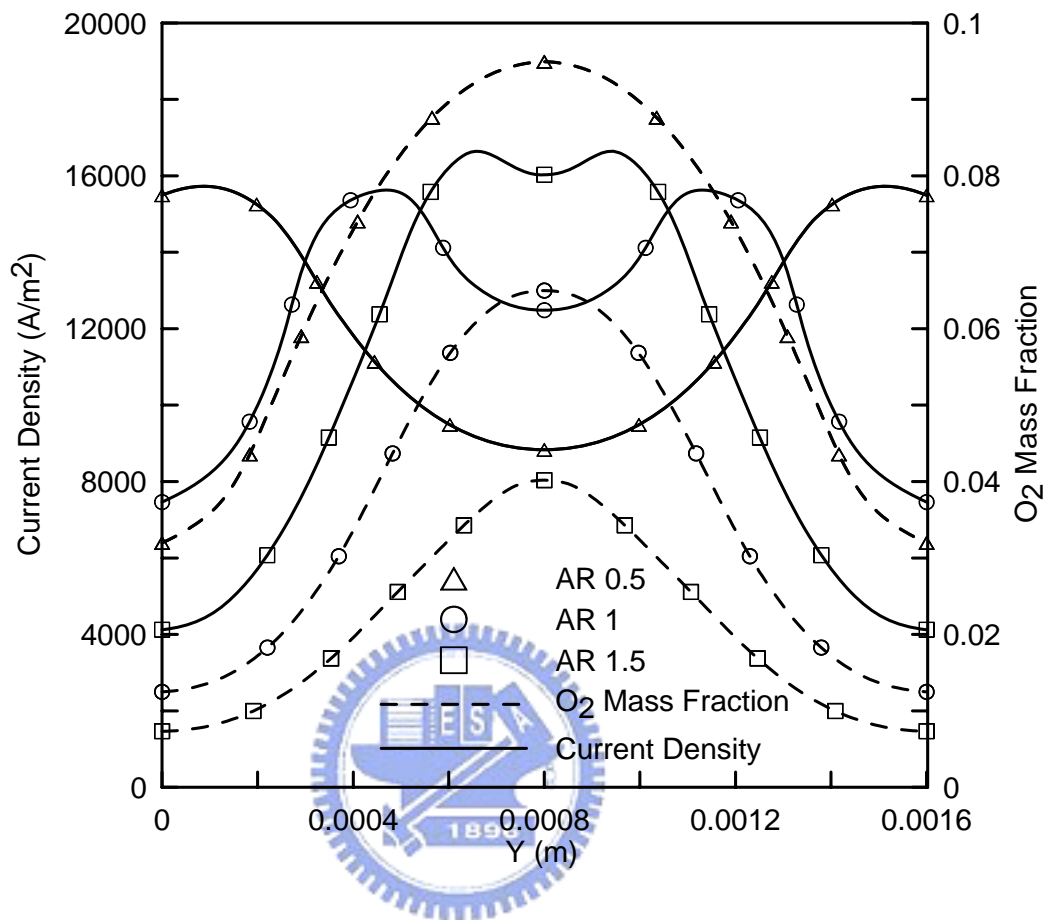


Fig. 4.9(b). Transverse distributions of oxygen mass fraction and local current density at the interface between the cathode catalyst layer and the GDL for three values of AR at cell voltage of 0.14V

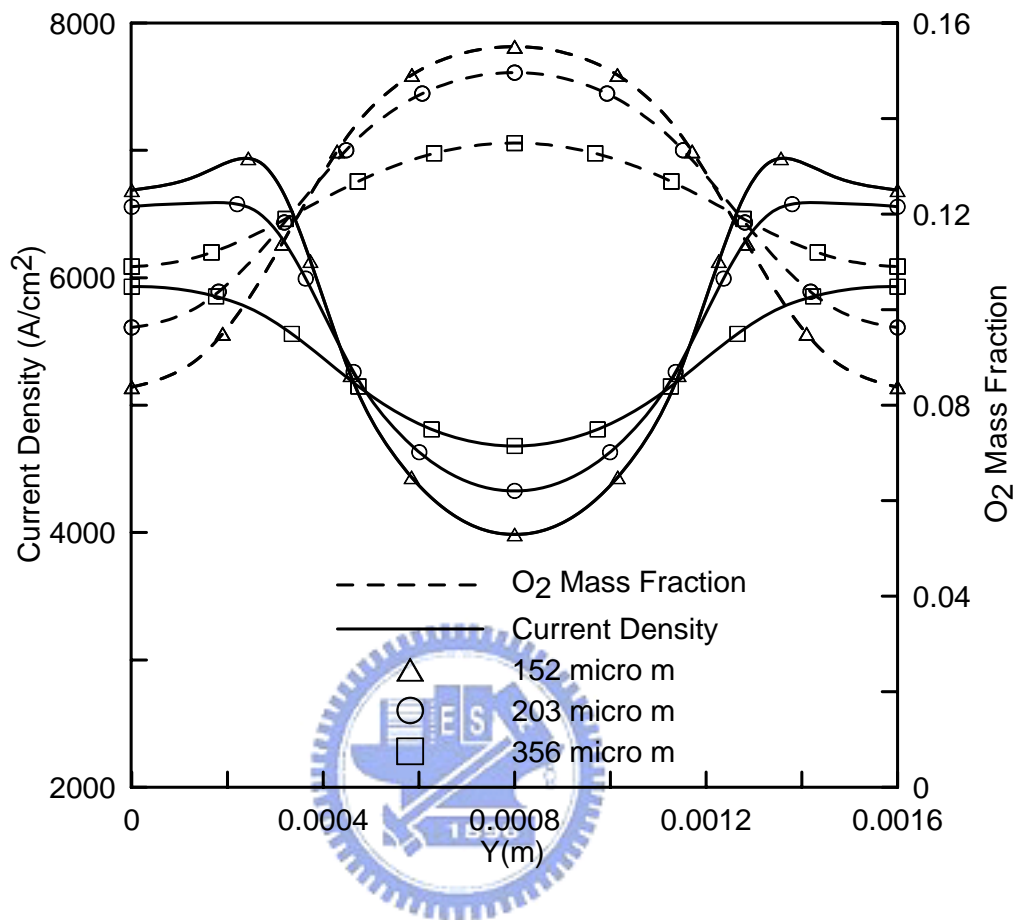


Fig. 4.10(a). Transverse distributions of oxygen mass fraction and current density at the interface between the cathode catalyst layer and the GDL for three GDL thicknesses at cell voltage of 0.62V

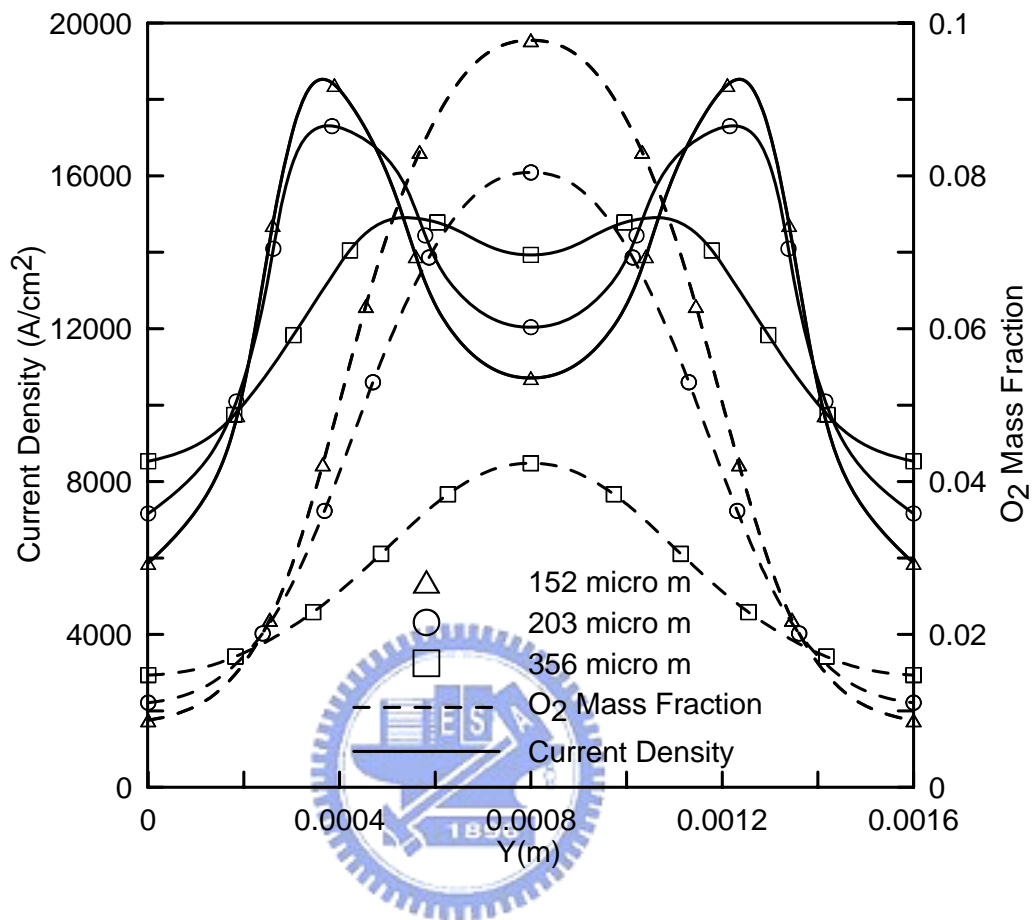


Fig. 4.10(b). Transverse distributions of oxygen mass fraction and current density at the interface between the cathode catalyst layer and the GDL for three GDL thicknesses at cell voltage of 0.14V

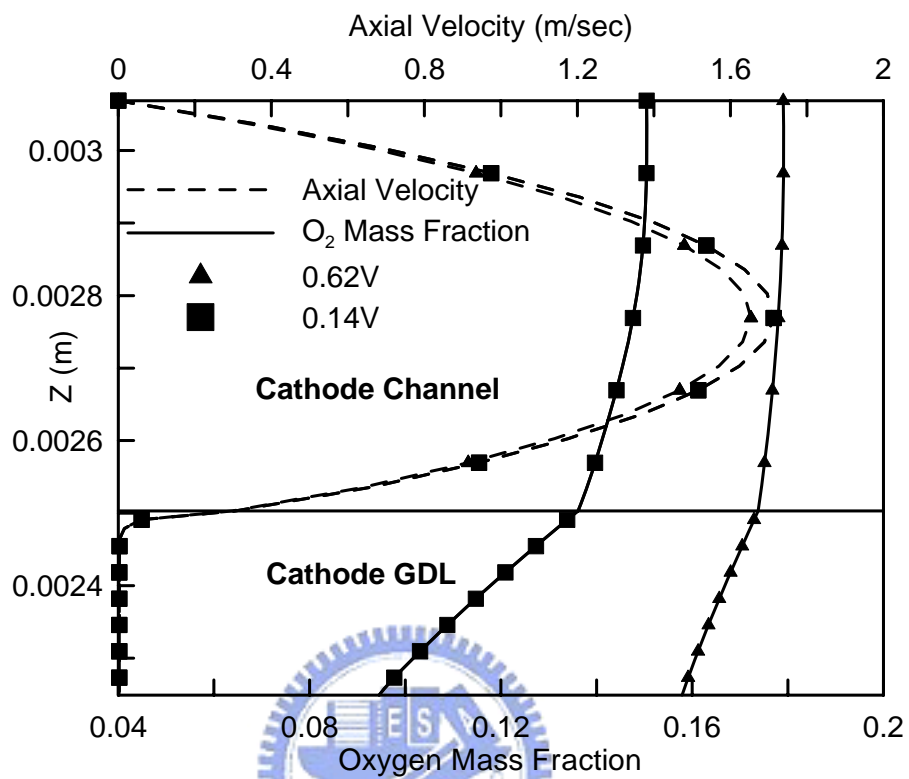


Fig. 4.11(a). Vertical distributions of fluid velocity and oxygen mass fraction in cathode channel and GDL for AR value of 0.5

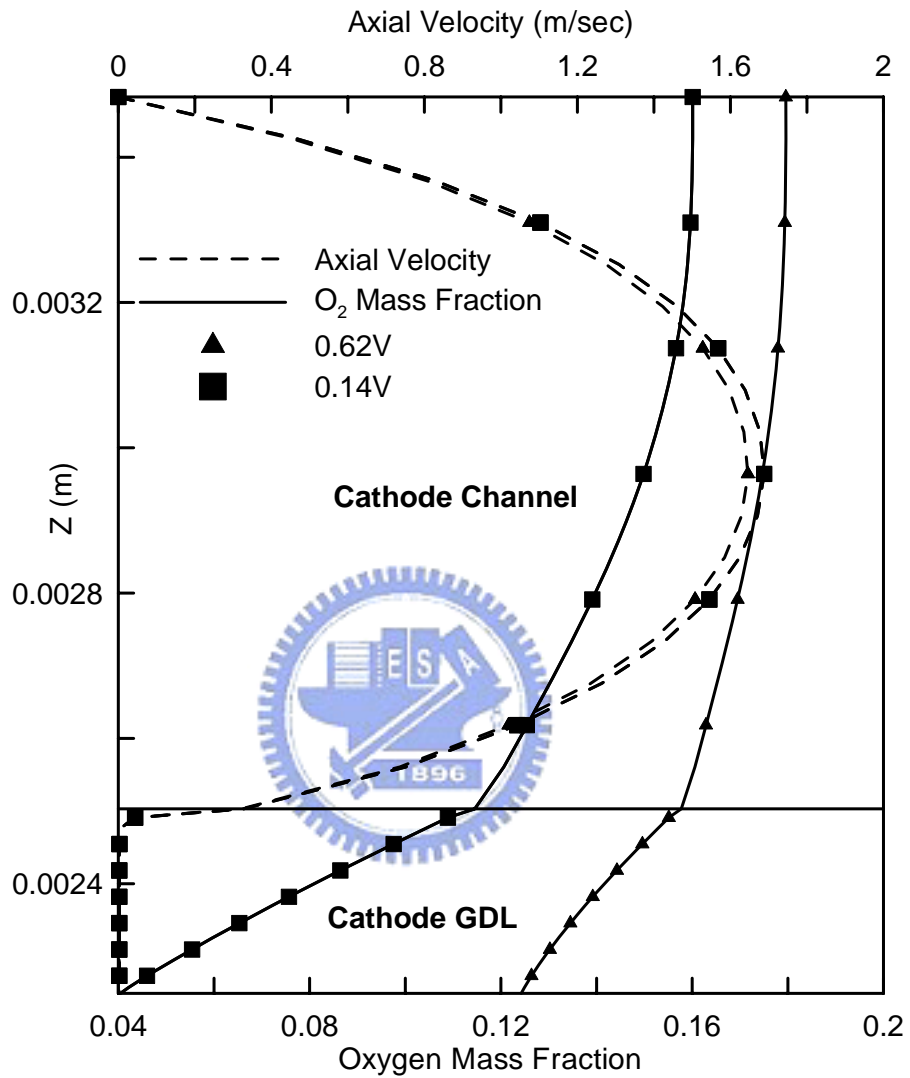


Fig. 4.11(b). Vertical distributions of fluid velocity and oxygen mass fraction in cathode channel and GDL for AR value of 1.5

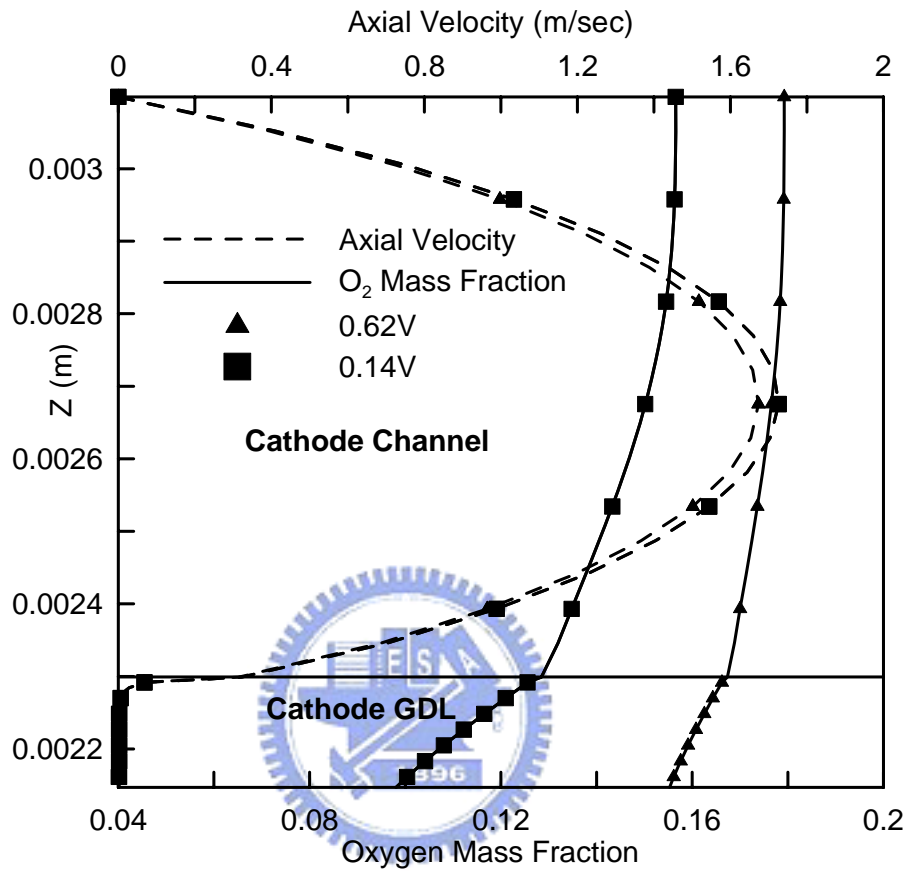


Fig. 4.12(a). Vertical distributions of fluid velocity and oxygen mass fraction in cathode channel and GDL for GDL thickness of 152 micrometers

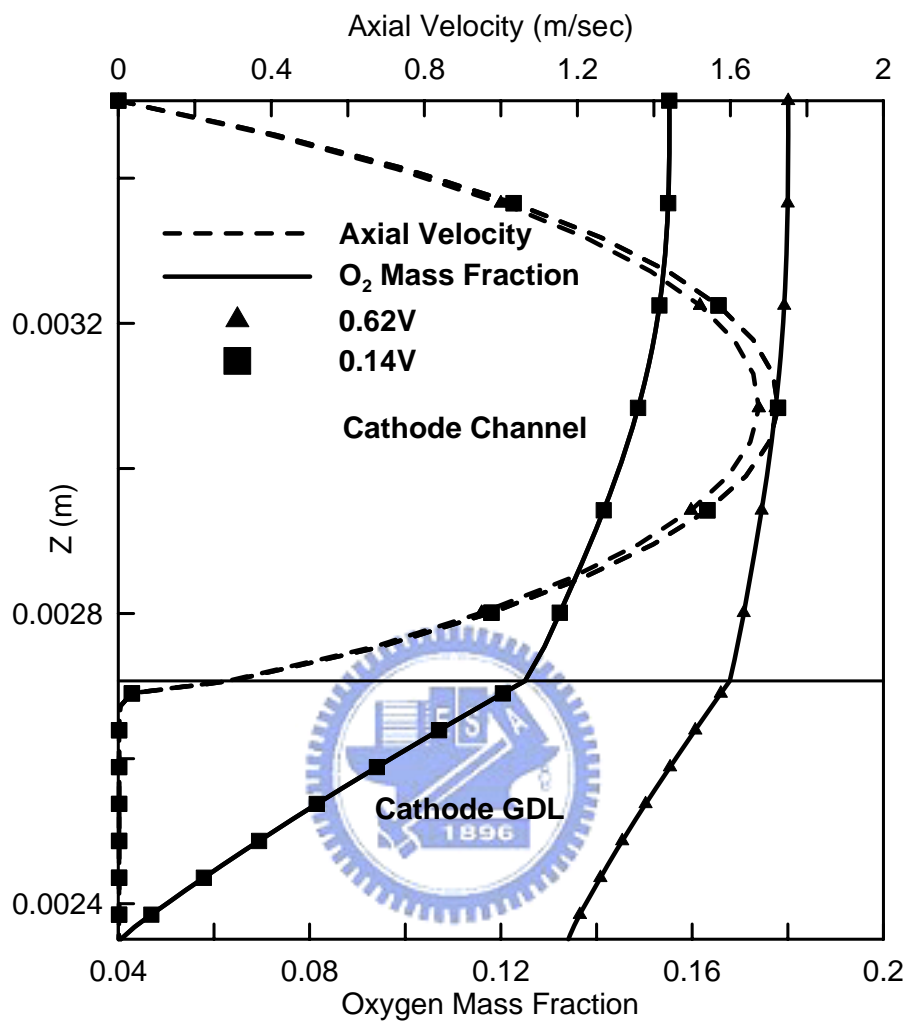


Fig. 4.12(b). Vertical distributions of fluid velocity and oxygen mass fraction in cathode channel and GDL for GDL thickness of 356 micro m

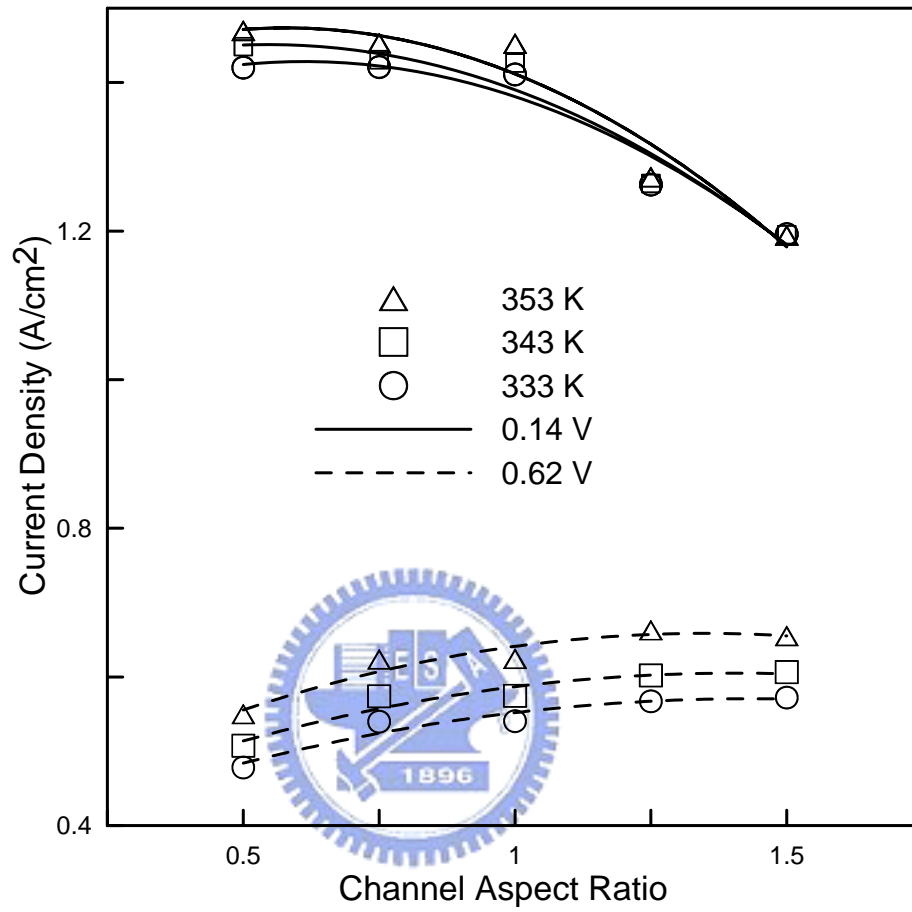


Fig. 4.13. Effects of operating temperature on cell performance at various values of AR

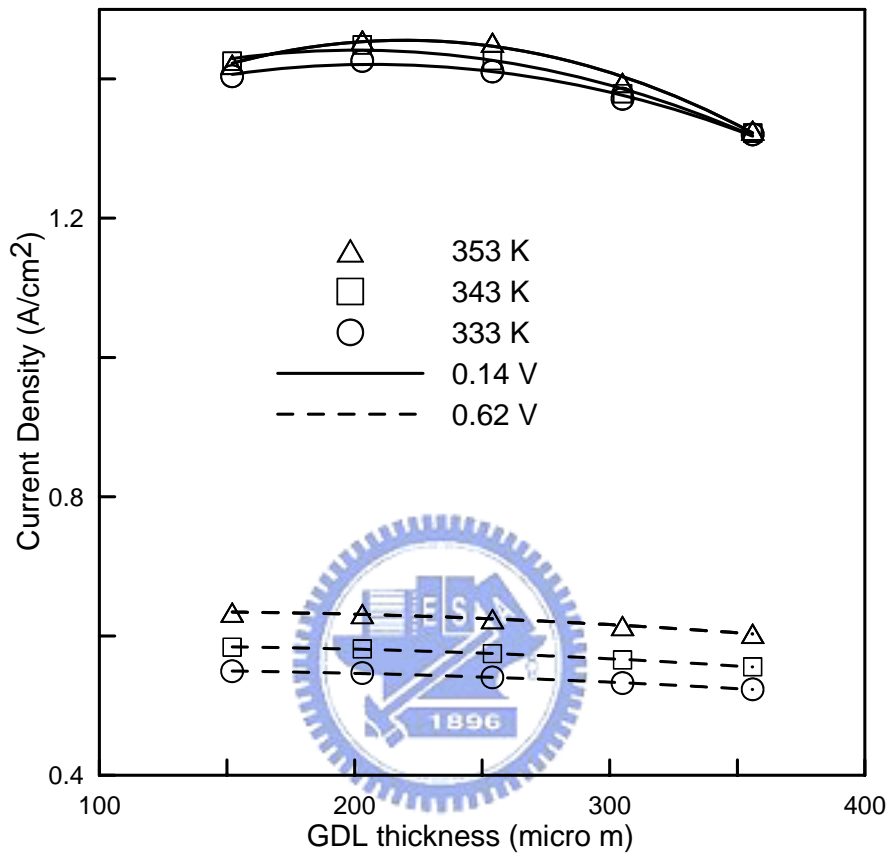


Fig. 4.14 Effects of operating temperature on cell performance at various values of GDL thickness

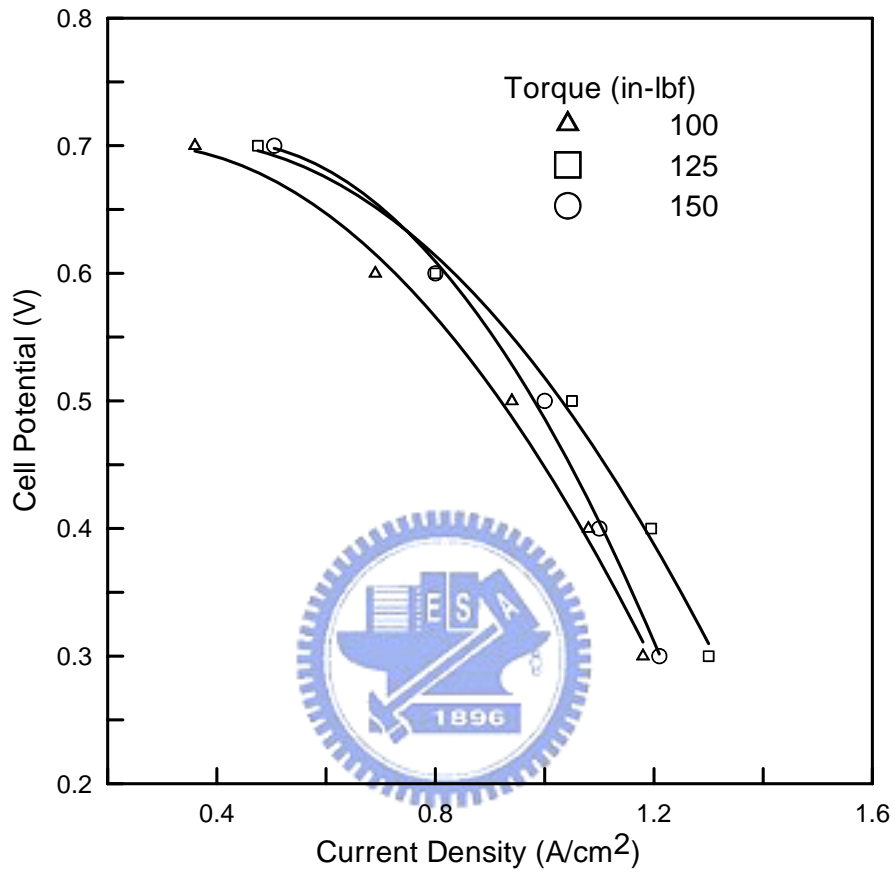


Fig. 4.15 Experimental results of Lee et. al. (1999a) on the effect of compression force on cell performance

CHAPTER 5

ELECTROCHEMICAL REACTION AND PERFORMANCE OF PROTON EXCHANGE MEMBRANE FUEL CELLS WITH NOVEL CATHODE FLOW CHANNEL SHAPE

5.1 *Introduction*

In previous chapter the roles of the transport component designs on the performance of PEMFCs are investigated in detail. Two factors, channel aspect ratio and GDL thickness are applied in the parametric modeling research to find the distributions of various transport variables such as local reactant concentration, water saturation and potential fields. Also the trends of cell performance variation are demonstrated and elucidated according to different operating voltages. The investigation indicates that the cell performance is dictated by the competition effect between electric current and reactant transport. According to the cell voltage, the electrochemical reaction is dominated by either electric conduction or reactant transport. That is, when the cell operates at medium reaction rate such as 0.62V, the role of reactant transport is not so important than electric conduction. Therefore, the transport component design which is beneficent to the electron transport delivers more current in such scenario. Consequently, a cell transport geometry with large channel

aspect ratio or a thin GDL thickness generate a relatively greater current in the reaction sites. However, with the increase of reaction rate, this trend is substituted by the reactant transport process as the requirement of high concentration reactant becomes more important, making the designs with small channel aspect ratio or large GDL thickness perform better at low cell voltage.

In this chapter, the investigation of the role of dominant mechanism in PEMFCs is extended to the quest of a novel channel geometry with variable shoulder/channel (S/C) ratio along the cathode channel. This channel configuration differs greatly from traditional channel design with a fixed S/C ratio throughout the cell domain. This is motivated from the result of previous investigation that the roles of electron and reactant transports dominate cell reaction at different situations. However, a straight channel design has no the flexibility of manipulating the local distributions of these two factors.

Figure 5.1 (a) illustrates the computational domain of current study. It consists of nine essential components of a single cell. A PEM is sandwiched by catalyst layers (CLs), gas diffusion layers (GDLs), flow channels and bipolar plates (BPs) on anode and cathode sides. As shown in Fig. 5.1 (b), one feature of this paper is that through the assignment of two parameters W_s and W_c at cathode outlet port, the widths of channel and shoulder are varied continuously along the main stream direction.

Employed data for various simulation cases are shown in Tab. 5.2. According to the S/C ratio parameter, the channel configuration can be cataloged into divergent (case A, B), straight (case C) and convergent (case E, F) channels.

5.2 Model Properties Distributions

5.2.1 Oxygen Concentration

The main purpose of the flow field in fuel cell is to deliver reactant throughout the cell domain. Furthermore, product from electrochemical reaction and non-reaction gas such as water and nitrogen should be carried out of the cell to provide space for fresh gas transport. Fig. 5.2 shows the oxygen mass fraction contour on middle horizontal plane of cathode catalyst layer at cell voltage of 0.62V and 0.22V for cathode channel configurations with S/C ratio of 0.67, 1 and 1.5. Note that the straight line drawn in the contour represents the boundary between channel and shoulder which indicates clearly what category the channel design is belong to. Vertical boundary lines in each contour represent the central region of shoulder (left) and channel (right) due to the adoption of the symmetric model domain. It is shown from Fig. 5.2 that the oxygen concentration distributions depend on cell operating conditions, positions as well as channel geometries. Clearly, the higher oxygen concentration locates close to the inlet port of channel and decreases gradually toward

the channel downstream and shoulder region because the cell reaction consumes oxygen. Also, this explains the reason that the oxygen concentration is larger at cell voltage of 0.62 V as the reaction is not so fast than that at 0.22V. Furthermore, these plots disclose the effect of channel geometry on the reactant transport for various operating conditions. At cell voltage of 0.62V, the divergent channel (case A) provides more even and higher reactant concentration than other designs due to its greater exposed area of catalyst layer under channel region. The same phenomenon is also found at 0.22V condition. From Fig. 5.2, the lowest oxygen concentration locates at shoulder region of channel downstream. Since the transverse transport of reactant is mainly due to diffusion, a larger S/C ratio at channel outlet port such as case E corresponds to a larger diffusion length, such that the oxygen is difficult to reach the shoulder central (left boundary of contour) region of the catalyst layer.

5.2.2 Water Saturation Level

Another important factor that influences the reactant transport in cathode is the liquid water saturation level. In Fig. 5.3, contours of liquid water saturation are shown at the same condition and location of Fig. 5.2. The influence of channel geometry on this factor is clearly seen. In general, the shoulder region of catalyst layer accumulates more liquid than channel region because the latter is close to the main stream of channel. The liquid water formed from cell reaction at this region is easy to transport

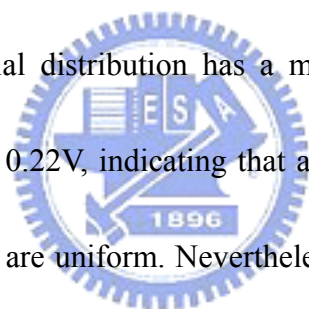
out of the cell. However, at shoulder central of convergent channel (case E) downstream, large amount of liquid water is accumulated due to its long transport path, especially at low cell voltage of 0.22V. Because the pore space available for reactant diffusion is clogged by liquid water, it manifests the result of relative lower oxygen concentration shown in Fig. 5.2.

5.2.3 Potential Fields and Activation Overpotential

Not only the mass transport variables are influenced by the design of channel geometry, the potential field distributions and electric currents are also affected. In fuel cell modeling investigation, the term overpotential is frequently mentioned in the literature. In general, it stands for the potential variation or loss in the cell region. As the electric conductivities of solid and membrane phase materials are finite, the electric resistances cause a certain degree of potential drop in two different positions when currents flow through them. Meanwhile, at a fix point in the CL, there exist two phase potentials and a local potential gap is built between solid and membrane phase materials. Such a potential gap represents another form of loss or irreversibility in a fuel cell. However, more importantly, it drives the process of electrochemical reaction.

Figure 5.4 presents the distribution of the two phase potential fields on middle plane of cathode catalyst layer for the model with straight channel geometry. Note that

in this study, a value of total cell overpotential is designated on the outer surface of cathode bipolar plate while that of anode bipolar plate is assigned as the reference potential level. From the fact that the negative charged species moves from lower potential to higher potential, also the positive charged species moves in the opposite direction, this figure discloses some interesting points which are worth further discussion. It is shown from the contour plots that the solid phase potential increases from shoulder region to channel region, meaning that the electrons at the cathode mainly move in this direction to participate the electrochemical reaction in CL. At cell voltage of 0.62V, the potential distribution has a more uniform distribution along channel direction than that at 0.22V, indicating that at this operating condition, local cell reaction and current flow are uniform. Nevertheless, at cell voltage of 0.22V, the reaction sites at upper stream shoulder region exhibit greater potential deviation from the designated cathode boundary potential, meaning that there are stronger cell reaction and solid phase current density than downstream shoulder region of catalyst layer. Also showed in Fig. 5.4, the membrane phase potential contours reveal a different variation trend. At cell voltage of 0.62V, upper stream catalyst layer beneath shoulder exhibits a stronger potential drop than that beneath channel. However, this position shifts to the channel region at cell voltage of 0.22V. This may reflect a fact that such a great membrane phase potential drop could be attributed to a stronger



electrochemical reaction at this location or smaller membrane conductivity due to low water content.

With the information of these two potential fields, the activation overpotential in CL can readily be obtained. Fig. 5.5 depicts the contours of this variable for three different channel designs at cell voltages of 0.62V and 0.22V. It is noted that in Eq. (17) the term of cathode activation overpotential appears in two exponential expressions. Therefore, the negative sign can be neglected when judging its strength of electrochemical driving force. It is found from this figure that in general, catalyst layer underneath shoulder region exhibits greater activation overpotential than that below channel region no matter what the cell voltage is. This is essentially due to smaller solid phase potential variation at shoulder region because the electrons migrate from shoulder to channel. Also, at channel down stream this value is larger than that at up stream. Considering the effect of channel geometry on this variable, it is found that a fuel cell with divergent channel produces more uniform distributions; meanwhile, a convergent channel design fuel cell generates higher activation overpotential at shoulder region of channel down stream. However, this additional driving force may not be able to generate corresponding higher current along because the oxygen concentration at this region should be taken into account.

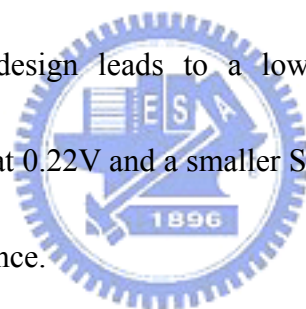
5.3 *Local Catalyst Reaction Rate*

According to the Butler-Volmer equation, the catalyst reactions in a fuel cell require two important factors – the reactant concentration and activation overpotential. According to the discussion in previous sections, it is evident that distributions of these two properties exhibit entirely different variation trends according to the operating condition and position. Therefore, the local cell reaction rate is expected to be non-uniform and requires further investigation.

Figure 5.6 illustrates the current density contours for the same channel configurations and operating conditions as previous figures. A manifest transition where higher local reaction takes place between medium and high reaction rates is clearly seen, no matter what channel geometry is. At cell voltage of 0.62V, the plot indicates that most current generated around shoulder region of catalyst layer. However, the higher reaction rate zone moves toward the interface between shoulder and channel regions as the cell voltage decreases to 0.22V. This is because that when cell operates at 0.62V, the electrochemical reaction is not so strong, therefore the high concentration reactant does not contribute completely to the cell reaction. On the contrary, the activation overpotential plays a more important role on the local current generation, making the position of higher cell reaction locates at shoulder central of channel upper stream. At 0.22V operating voltage, the catalyst reaction is increased

and high concentration reactant is needed for the reaction. This fact causes the high current density position moves toward the channel direction where perfect combination of concentration and activation exists. Therefore, despite the fact that channel central region has greater oxygen concentration than other place, it dose not generate corresponding high current because the activation overpotetnial is the lowest.

According to these discussions, the effects of channel outlet port S/C ratio for different operating conditions can also be found in Fig. 5.6. At high cell voltage, a larger S/C ratio design creates more region of high current density such as case E of Fig. 5.6(a). However, this design leads to a low current density zone around downstream shoulder central at 0.22V and a smaller S/C ratio design such as case A is found to have better performance.



In order to elucidate the local dominate mechanism of cell reaction, Fig. 5.7 depicts the transverse distributions of local oxygen mass fraction and local current density at 0.62 V cell voltage and S/C values of 0.67, 1.50. The position is on the same plane of previous figures at $x=0.012\text{m}$ and 0.048m . It is found from Fig. 5.7 (a) that around channel upper stream, although a divergent channel such as S/C equal to 0.67 provides higher reactant concentration, its reaction rate is smaller than the convergent channel design, meaning that at this operating condition, conduction overpotential dominates local cell reaction. That is, a channel design with wider

shoulder offers a less resistance passage for the transverse transport of electrons and the potential loss is smaller than that with narrower shoulder. Therefore, the convergent channel design has larger activation overpotential and higher local reaction rate. The plot in Fig. 5.7(b) exhibits a stronger variation of current density and oxygen concentration between divergent and convergent channel designs. Due to a wider shoulder, the design with 1.50 S/C value at outlet port results in a relatively lower level of oxygen concentration, especially at shoulder region. Consequently, the shoulder region of convergent channel is dominated by the concentration overpotential and the channel region is dominated by the conduction overpotential. On the contrary, because of the higher oxygen concentration level provided by the divergent channel, the transverse local current density exhibits the conduction overpotential dominated mechanism for cell reaction.

Comparison of local current density between convergent and divergent channel designs at high cell reaction rate is shown at Fig. 5.8. At position of $x=0.012$, the oxygen concentration distributions has a similar variation trend with that at 0.62V. Also, the channel regions of these two channel configuration still exhibit conduction dominate mechanism at 0.22V cell voltage. Nevertheless, a clear transition exists at domain central that change the relative magnitude of current densities at shoulder region for these two channel designs. This is attributed to the extremely low level of

oxygen concentrations around shoulder regions at 0.22 V cell voltage. However, at downstream region the convergent channel design is entirely dominated by concentration overpotential and the variation trends between local current density and oxygen concentration are consistent in Fig. 5.8 (b). This reflects a fact that a convergent channel configuration is unable to offer sufficient reactant concentration at channel downstream region when the cell reaction rate is high.

5.4 Cell performance for Channel Design with Various S/C Ratios

In order to provide a quantitative comparison of the novel flow channel design, the bar chart of average current density at various cell voltages is shown in Fig. 5.9 for five cathode outlet port S/C ratios. This figure indicates the transition of better cell channel design with operating voltage. At cell voltage of 0.22V, divergent channel with S/C ratio of 0.67 creates the greatest current density than other cases. This is because that at such a high reaction rate, more oxygen can be transported to the reaction sites under the channel region for this channel configuration. However, as the average reaction slows down and cell voltage increases, this characteristic gradually lost its importance. Contrarily, a smaller S/C design which offers wider shoulder region becomes more beneficial for the cell reaction because it facilitates the electrons transport to the catalyst layer and enhances the activation overpotential.

5.5 *Effect of Reactant Stoichiometry on Cell Performance*

As the reactant flow rates have significant impact on cell performance, it is instructive to examine the effect of reactant stoichiometry on reaction rate. Figure 5.10 shows the cell output current densities for three values of reactant stoichiometry at cell voltages of 0.22V and 0.62V. It is found that the influence of reactant stoichiometry is obvious at lower cell voltage such as 0.22V. When the reactant stoichiometry is low, less fuel and oxygen are supplied into the cell so the corresponding output current density is small. In such circumstance, the role of channel geometry on cell performance is vital. Fig. 5.10 reveals that when the stoichiometry is 2, larger variations of output current exist among the three different channel shapes. This is attributed to the fact that at 0.22V, more reactants are required to fulfill electrochemical reactions. Therefore, the reductions of stoichiometry and reactant flow rate enhance the important role of channel geometry design. However, such tendency decreases as the stoichiometry increases to 4 because the fertile reactant flow rate makes the role of channel geometry less important than that at stoichiometry of 2.

At a medium cell voltage, the reactant stoichiometry effect on current density is minor as the electrochemical reaction is dominated by conduction and activation overpotentials. However, a close inspection of Fig. 5.10 indicates that it presents a

relatively larger influence on current density for the convergent shape channel. Despite the greater shoulder region of such channel configuration facilitates electrons transport to reaction sites and enhances output current, the cell reaction rate is reduced at lower stoichiometry as the reactant concentration is relatively small. This phenomenon reflects the need of detail inspection of the impact for various operating parameters on such novel flow channel.

5.6 Summary

An investigation of the effects of novel flow channel with various outlet port S/C ratios in PEM fuel cell on the transport phenomena and catalyst reaction has been performed through a three-dimensional multi-component model. The influence of channel geometry on local oxygen, potential and current density distributions are examined in detail. According to the results and discussion, the following conclusions can be drawn.

1. The configuration of flow channel influences the distribution of various transport variables such as reactant concentration, saturation level, potential field and activation overpotential.
2. For a narrower channel with large S/C ratio at outlet port, the average passage for electron conduction to the reaction site is shorter, such that it can generate more

current at medium cell voltage where the activation overpotential dominates the catalyst reaction.

3. With the increase of cell reaction rate, the requirement of high reactant concentration becomes more important. Therefore, the best channel geometry shifts toward the design with small S/C outlet port ratio, which offers a shorter transport passage for oxygen around channel region.
4. The saturation level of liquid water also has an important effect on oxygen transport and cell reaction rate, especially at low cell voltage. Consequently, the divergent channel design creates higher current density at such operating condition as the liquid water is easy to transport out of the channel from the outlet port.
5. Transverse plots of local current density and oxygen concentration demonstrate the dominate mechanism of local cell reaction. When the variation trends between these two parameters are consistent, the cell reaction is dominated by concentration overpotential. Otherwise, it is controlled by conduction and activation overpotentials.
6. The reactant stoichiometry effect on cell performance is quite obvious at lower cell voltage where a great amount of fuel and oxygen are required to fulfill the



electrochemical reaction. Furthermore, it bears greater influence on output current among different channel geometries at a value of 2.



Table 5.1 Main cell parameters, properties and operating conditions

gas channel length, 6.0E-2 m	diffusion layer porosity, 0.4
gas channel thickness, 1.0E-3 m	catalyst layer porosity, 0.28
diffusion layer thickness, 2.54E-4 m	membrane porosity, 0.28
catalyst layer thickness, 1.0E-5 m	diffusion and catalyst layer permeability, 2.3E-11 m ²
membrane thickness, 1.75E-4 m	membrane permeability, 1.0E-18 m ²
gas channel half width (inlet port), 5.0E-4 m	reactant relative humidity, 100 %
shoulder width (inlet port), 5.0E-4 m	oxygen mass fraction at channel inlet port, 0.196
cathode inlet velocity, 0.84 m/sec	vapor mass fraction at cathode inlet port, 0.160
anode inlet velocity, 0.35 m/sec	vapor mass fraction at anode inlet port, 0.733
cell back pressure, 2 atm	hydrogen mass fraction at anode inlet port, 0.267
cell temperature, 80 °C	electrode conductivity, 114 S/m



Table 5.2 Simulation cases for various channel configurations used in this study

case	A	B	C	D	E
description	divergent channel	divergent channel	straight channel	convergent channel	convergent channel
$W_s(S)$	0.4mm	0.45mm	0.5mm	0.55mm	0.6mm
$W_c(C)$	0.6mm	0.55mm	0.5mm	0.45mm	0.4mm
S/C ratio (W_s/W_c)	0.67	0.82	1.00	1.22	1.5



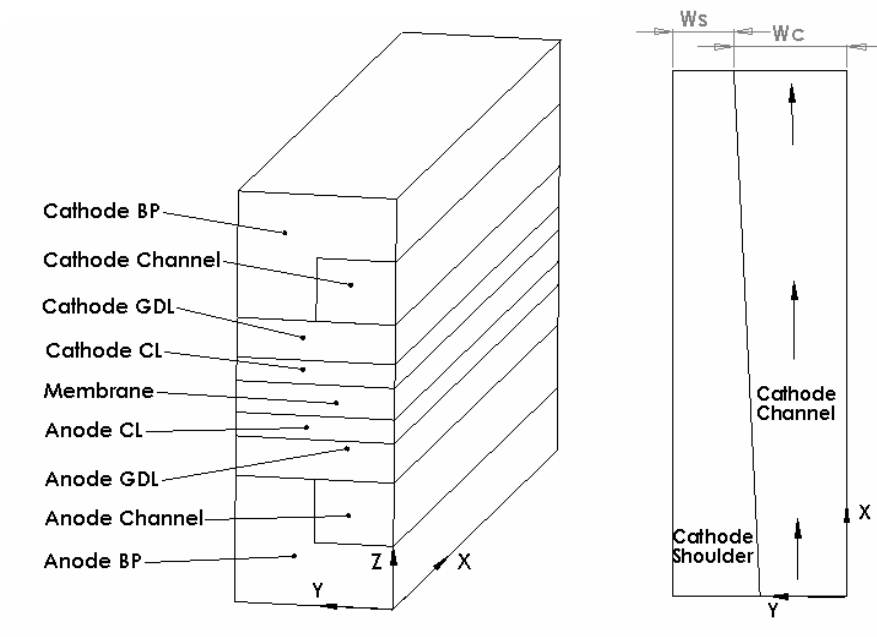
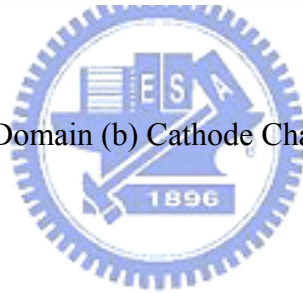


Figure 5.1 (a) Computational Domain (b) Cathode Channel Configuration



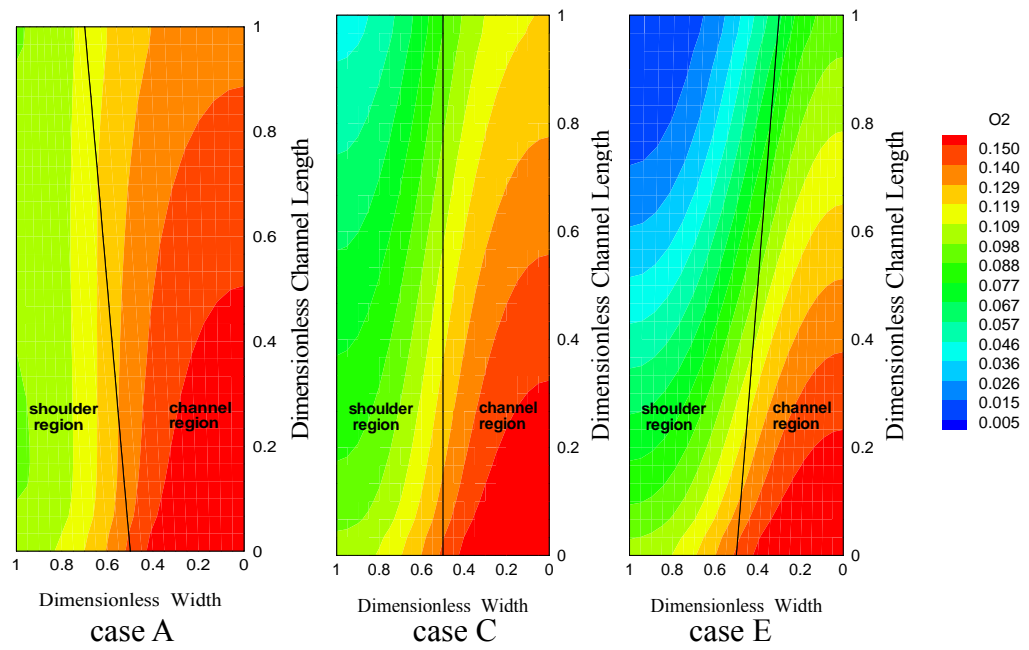


Figure 5.2 (a) Oxygen mass fraction contours at cell voltage of 0.62V for outlet port S/C values of 0.67, 1 and 1.5

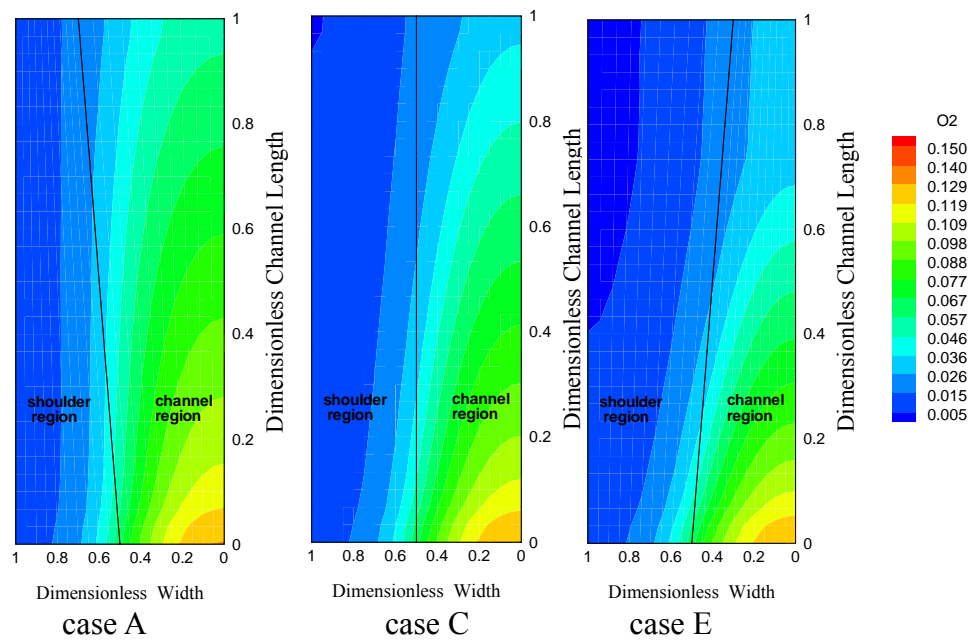


Figure 5.2 (b) Oxygen mass fraction contours at cell voltage of 0.22V for outlet port S/C values of 0.67, 1 and 1.5

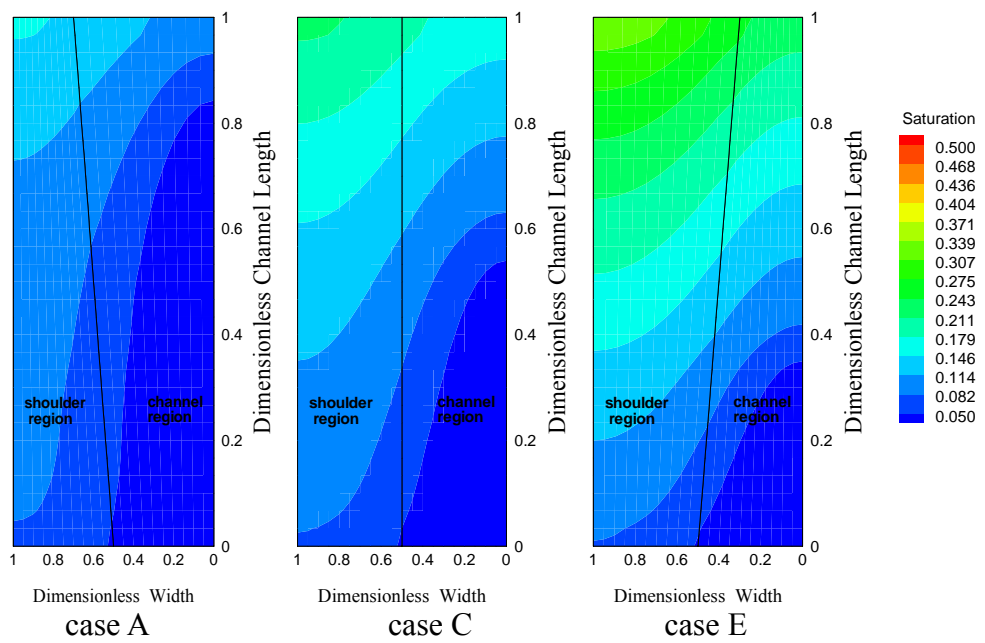


Figure 5.3 (a) Liquid water saturation contours at cell voltage of 0.62V for outlet port S/C values of 0.67, 1 and 1.5

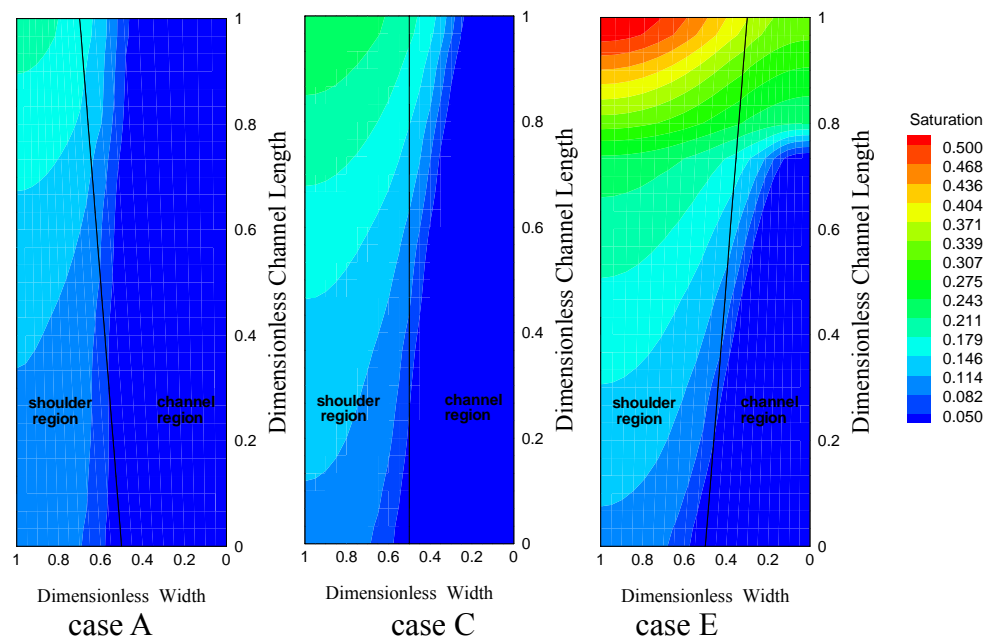


Figure 5.3 (b) Liquid water saturation contours at cell voltage of (a) 0.62V (b) 0.22V for outlet S/C values of 0.67, 1 and 1.5

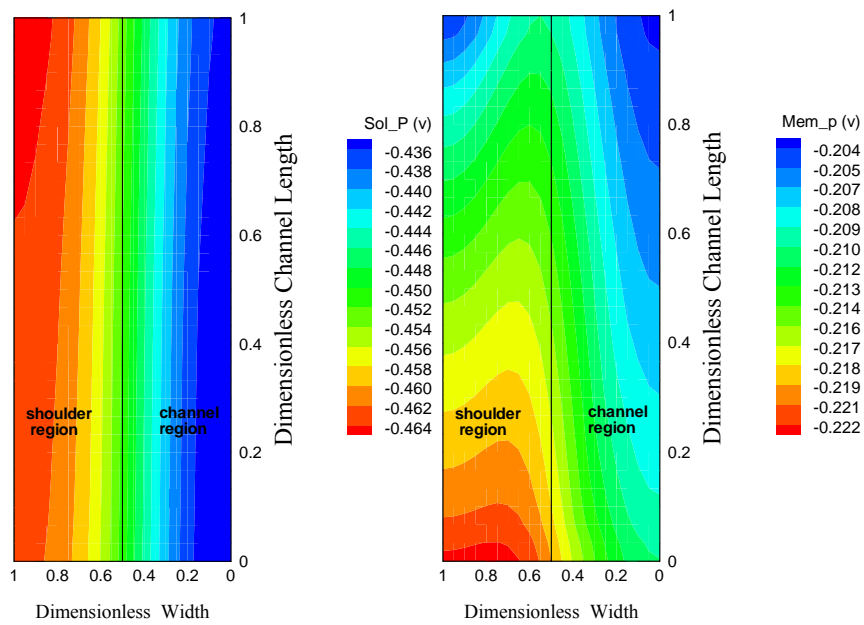


Figure 5.4 (a) Solid and membrane phase potential contours at cell voltage of 0.62V for straight channel

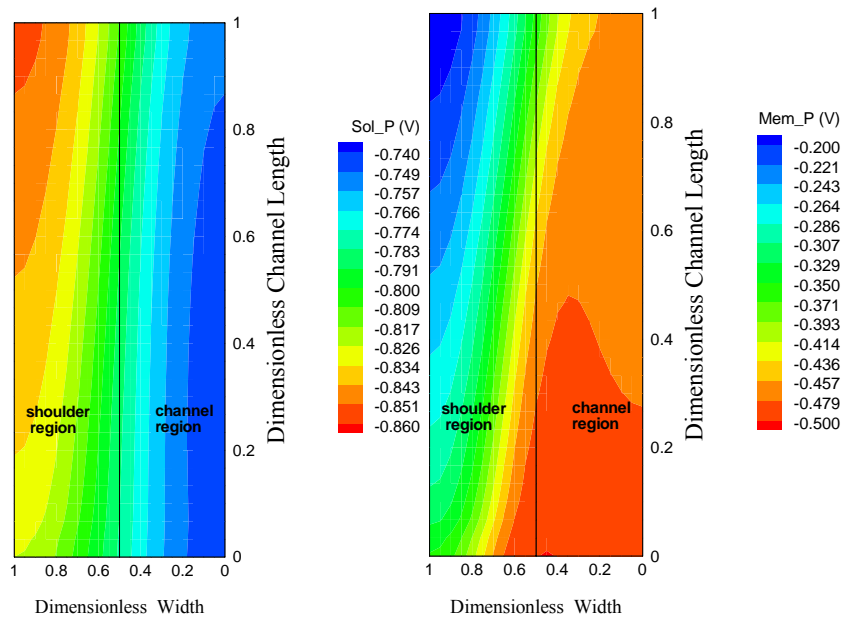


Figure 5.4 (b) Solid and membrane phase potential contours at cell voltage of 0.22V for straight channel

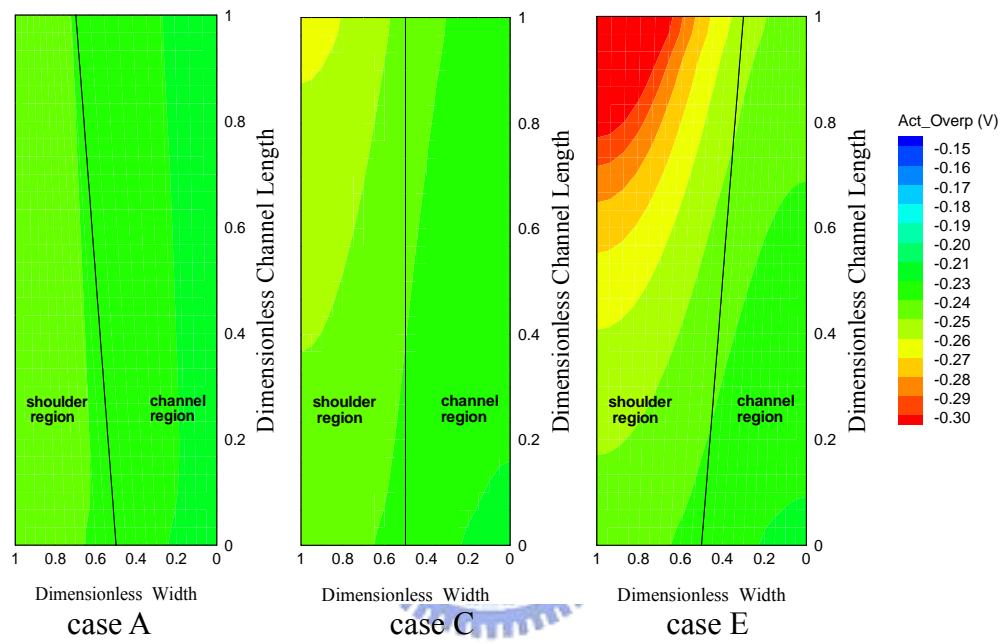


Figure 5.5 (a) Activation overpotential contours at cell voltage of 0.62V for outlet port S/C values of 0.67, 1 and 1.5

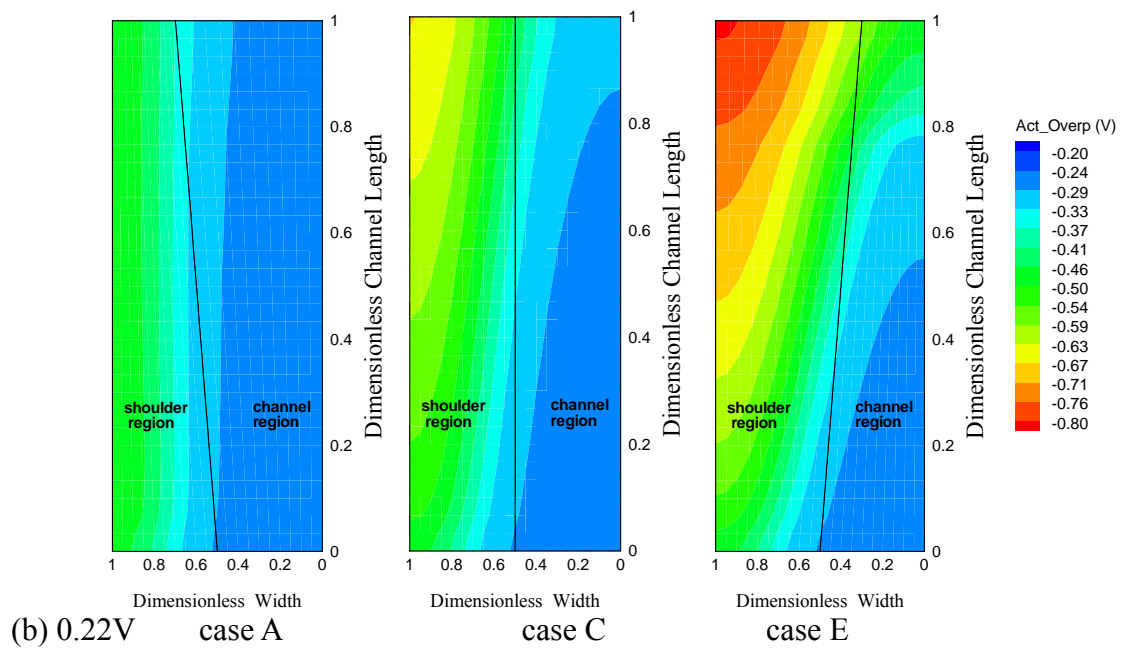


Figure 5.5 (b) Activation overpotential contours at cell voltage of 0.22V for outlet port S/C values of 0.67, 1 and 1.5

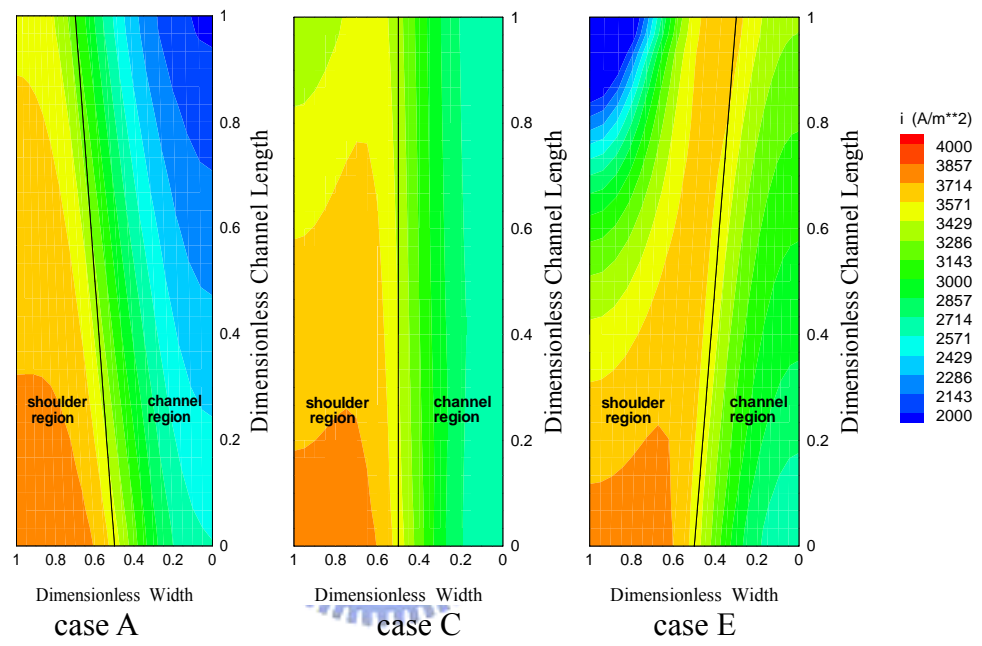


Figure 5.6 (a) Current density contours at cell voltage of 0.62V for outlet port S/C values of 0.67, 1 and 1.5

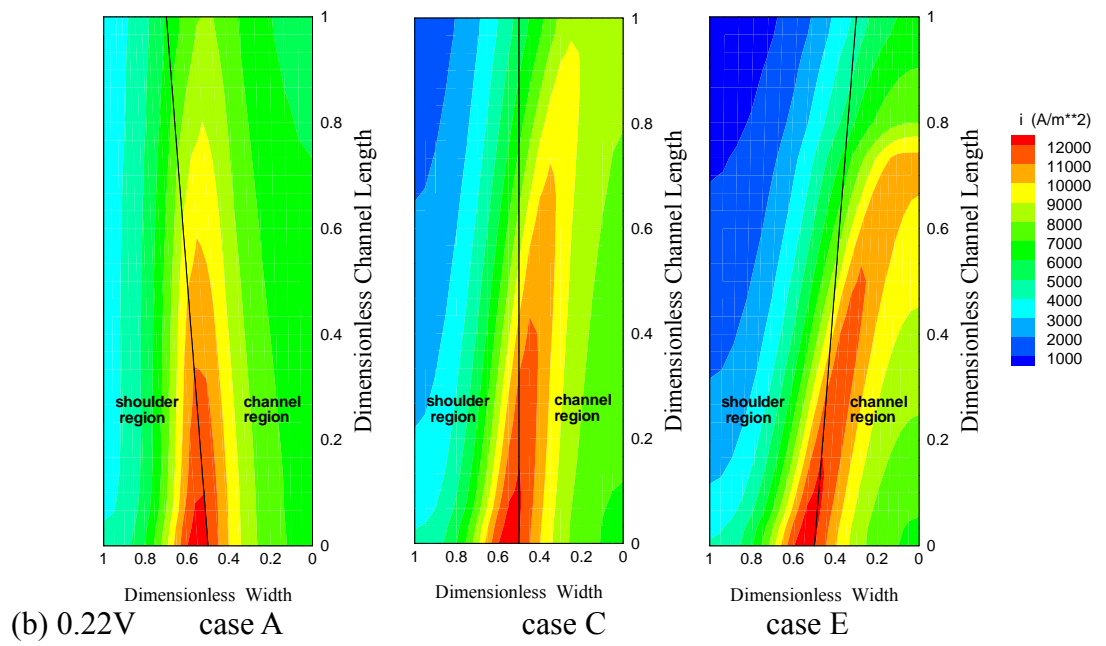


Figure 5.6 (b) Current density contours at cell voltage of 0.22V for outlet port S/C values of 0.67, 1 and 1.5

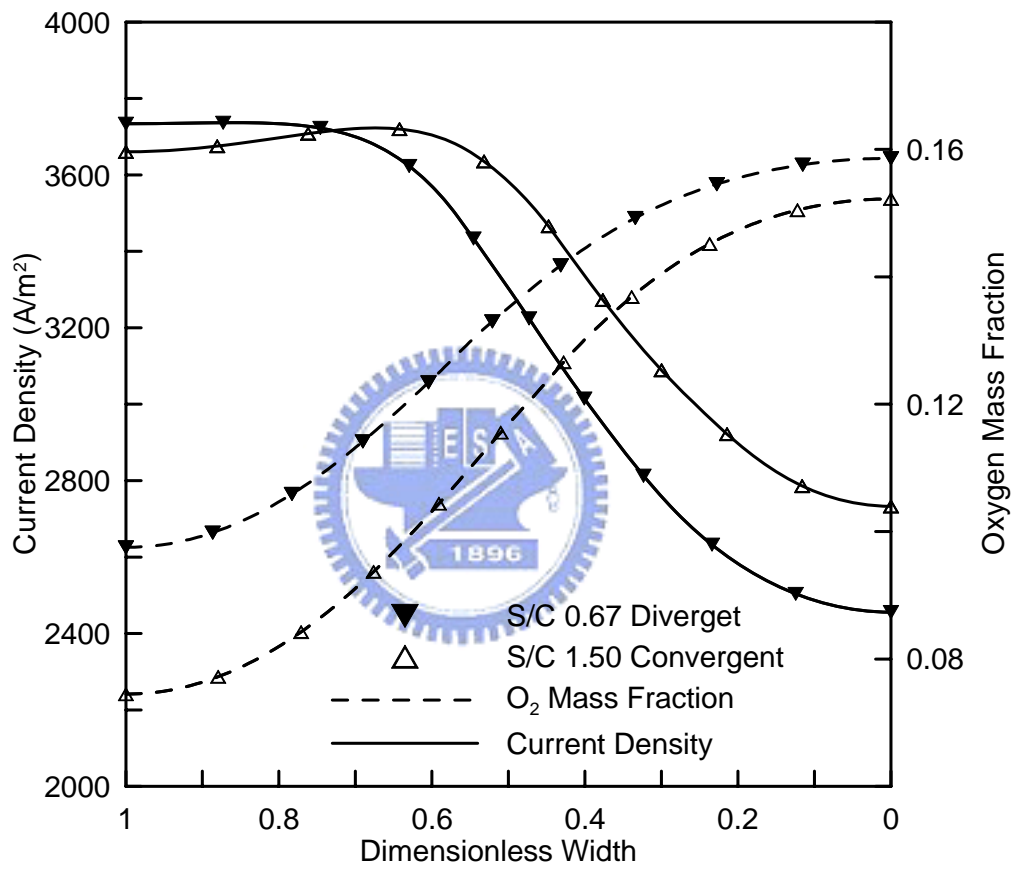


Figure 5.7 (a) Transverse oxygen mass fraction and current density at $x=0.012\text{m}$ of CL middle plane with cell voltage of 0.62V and S/C values of $0.67, 1.50$

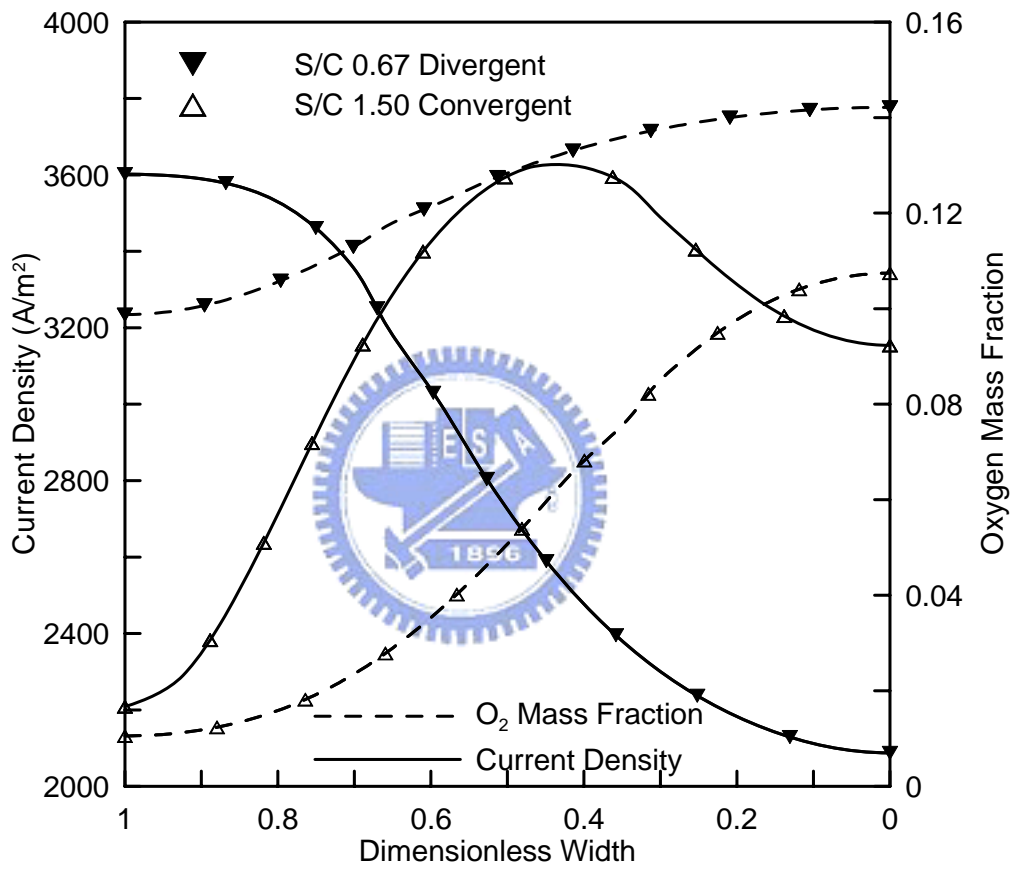


Figure 5.7 (b) Transverse oxygen mass fraction and current density at $x=0.048\text{m}$ of CL middle plane with cell voltage of 0.62V and S/C values of $0.67, 1.50$

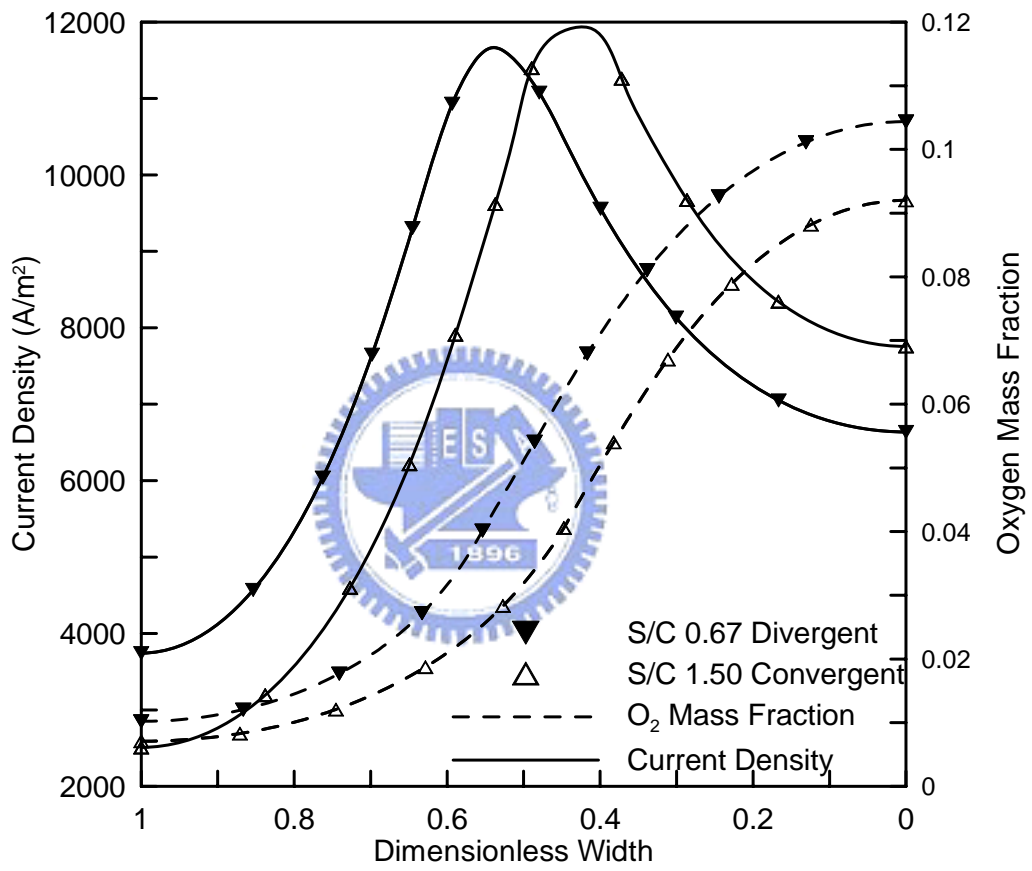


Figure 5.8 (a) Transverse oxygen mass fraction and current density at $x=0.012\text{m}$ of CL middle plane with cell voltage of 0.22V and S/C values of $0.67, 1.50$

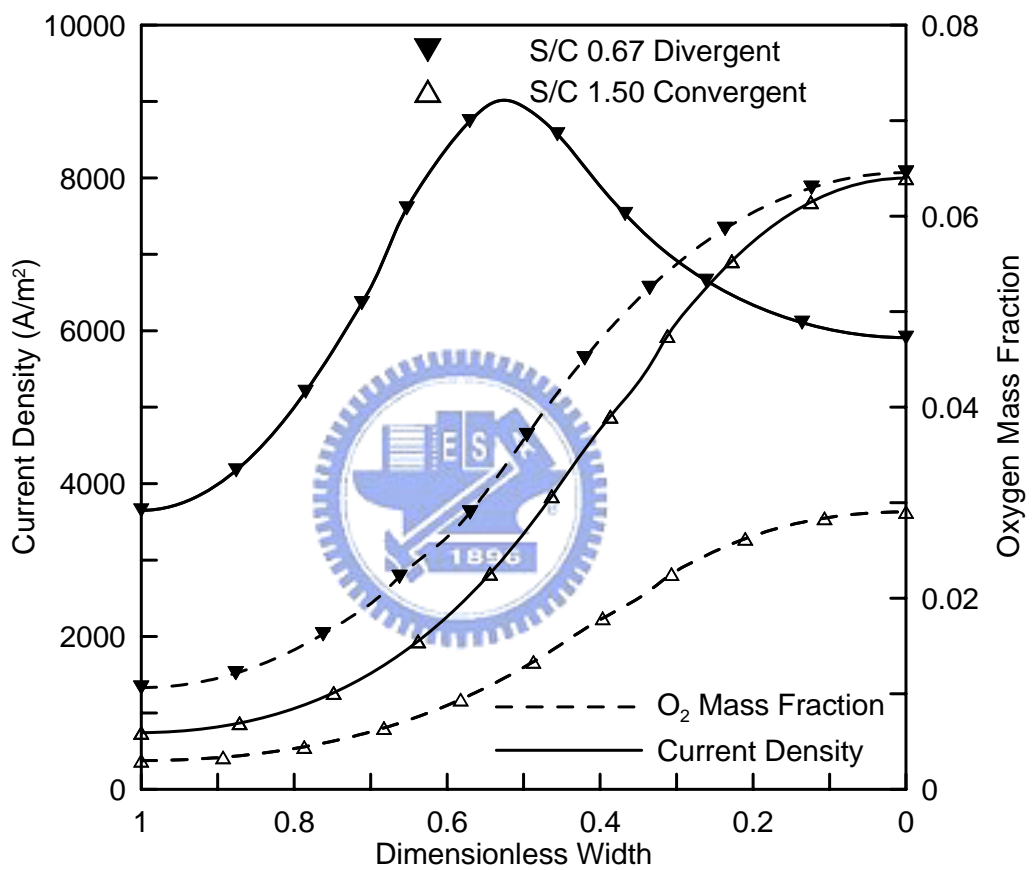


Figure 5.8 (b) Transverse oxygen mass fraction and current density at $x=0.048\text{m}$ of CL middle plane with cell voltage of 0.22V and S/C values of $0.67, 1.50$

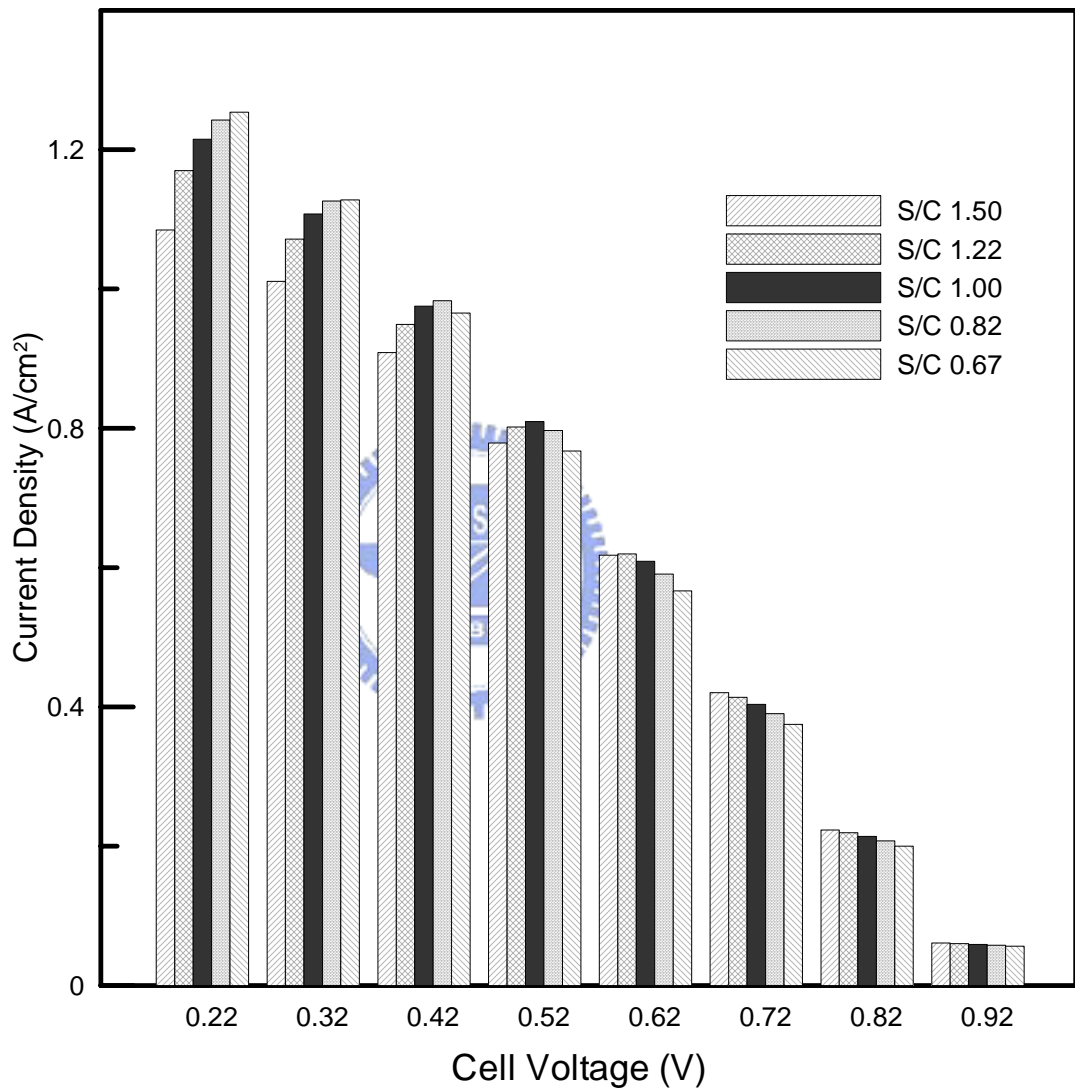


Figure 5.9 Comparison of cell performance for various cathode channel geometry designs

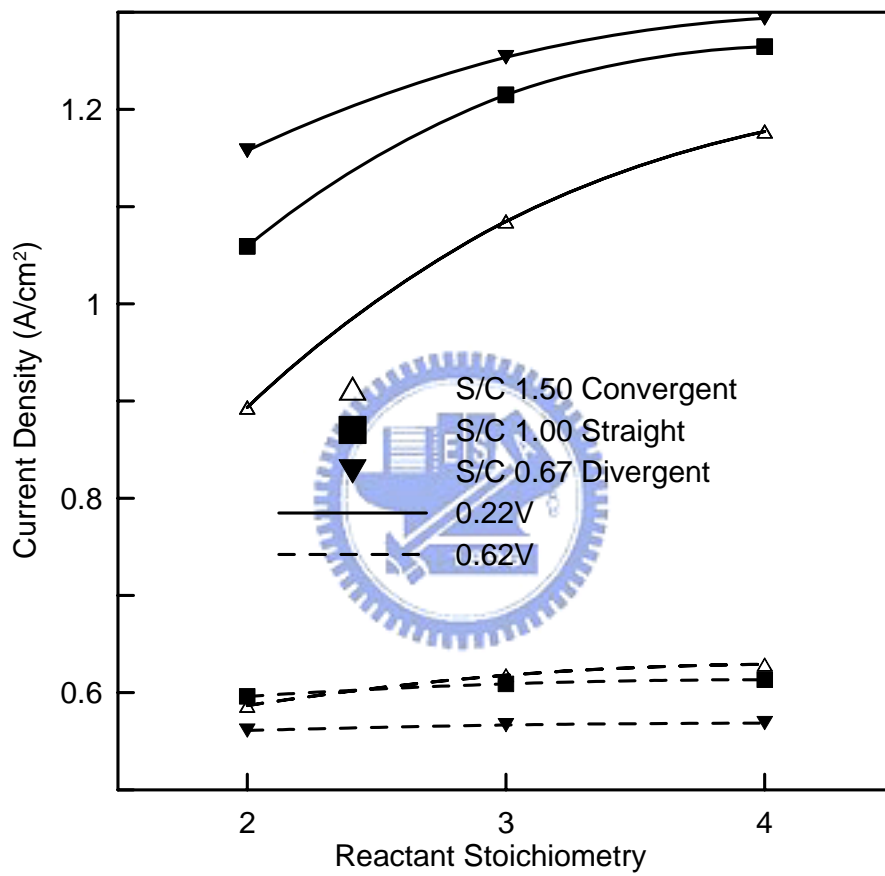


Figure 5.10 Effect of reactant stoichiometry on cell current density at operating voltages of 0.22V and 0.62V for three cathode channel configurations

CHAPTER 6

CONCLUSIONS AND FUTURE PERSPECTIVES

6.1 *Concluding Remarks*

In this dissertation, comprehensive descriptions on the multi-component, multi-phase transport phenomena as well as the processes of electrochemical kinetics, local current transfer and thermal flow have been presented. A multi-physics model with computational fluid dynamics technique is successfully employed to investigate complex behaviors in the PEMFCs. The model is able to resolve local activation overpotential which is the actual driving force of the cell reaction. In addition, it is validated through comparison with several previous works including numerical and experimental ones and considerable consistency of the trends of performance variations is achieved.

In the analysis of the effects of temperature and humidification level, a series of numerical predictions of cell performance subjected to various gradients of temperature or humidification level have been conducted. It is found that cell performance can be enhanced by the scheme of cathode reduced humidification because the reason of mass transport passage is unlikely to be plugged at high reaction rate. However, cell output current decays at higher or lower anode humidification

levels with the reasons of mass transport overpotential or poor membrane conductivity respectively. The analysis also reveals that larger temperature gradient is harmful to cell performance at high current density for a larger temperature gradient. Despite of this result, at medium reaction rate and low anode temperature, cell temperature gradient imposes positive effect on its output current. Furthermore, local physical properties distributions are also presented in the analysis. It exposes a close relation between these distribution and cell performance.

Subsequently, the developed model is used to investigate the impacts of cell transport component designs on the performance and various transport properties. The effects of channel aspect ratio on local oxygen and potential distributions are demonstrated. Furthermore, the relationships of these properties with cell polarization curves are well discussed. It is found that the higher the current density, the slender the optimal channel aspect ratio is. Also, position of highest activation overpotential shifts toward shoulder central at various AR designs. However, the largest current density location is subjected to the competition effect between reactants and electrons transport. In this content, its values exhibits different trend for medium and high reaction rates. As a result, optimal AR can be drawn depending on the operating voltage.

Following the previous works, the influence of GDL thickness on various parameters and cell performance is examined. It is demonstrated that there exists different variation tendencies between membrane conductivity and phase potential at low reaction rate. However, at high reaction rate they coincide with each other. Furthermore, this factor imposes limitation on the transport of electrons and fluids in either transverse or vertical directions of model domain. For a thinner thickness, these species are easy to deliver in vertical direction but difficult in transverse direction. So that thinner value of GDL thickness is beneficial at medium cell voltage. On the contrary, at high cell reaction rate, the requirement of high concentration reactants results in the increase of GDL thickness which draws the largest cell current. However, this trend of maximum output current thickness reverses its direction with the reasons of low oxygen concentration and mass transport clogging at higher reaction rate.

In the final part of this dissertation, the developed model is employed to quest the electrochemical reaction and performance of PEMFCs with a novel cathode flow channel. Through the assignment of S/C ratio at cathode outlet port with various values, the configurations of this novel channel can be cataloged into divergent, straight and convergent ones. Contour plots of the essential model variables such as reactant concentration, potential fields, activation overpotential as well as local reaction rate are presented and discussed.

Numerical results show that flow channel configuration influences the local distribution of the aforementioned model variables as well as the cell performance. For a convergent shape channel, the electrons transport passages are enhanced and the cell performance increases at medium cell voltage where activation overpotential dominated the cell reaction. However, when the reaction rate increases, the divergent channel is able to provide sufficient oxygen to the reaction sites and the output current increases accordingly. Furthermore, the water saturation level in this channel configuration is smaller than that of other channel configurations. This is also beneficial to the performance at low cell voltage.

The transverse plots of local current density and oxygen concentration provide a further insight to the dominant mechanism of cell reaction. When these two plots have consistent variation trends, the cell reaction is controlled by the mass overpotential. This is usually seen at scenarios when cell reaction rate is higher or where the oxygen concentration is low especially at shoulder region of channel downstream. Moreover, the discussion of the reactant stoichiometry effect shows that at a value of 2, it bears greater influence on output current among the various channel configurations. With the knowledge of the well comprehended determining reasons of global performance variation, these results can further offer the explanations, which are of great important to the researchers and engineers, of the different dominant

mechanisms resulting from the characteristic differentials of transport phenomena for the various species inside the fuel cell.

6.2 *Future Perspectives*

The investigations and findings in previous chapters offer an essential knowledge base for the subsequent study. The transport component design effects study in chapter 4 focus on the discussion at a representative position and a constant AR along channel direction. In an actual cell the species concentrations vary continuously along channel direction. At upper region of channels, oxygen and hydrogen have higher mass fraction and the cell reaction rate is faster than downstream location. As a result, there exists an extreme un-uniform electrochemical reaction and current density, especially at low cell voltage. This phenomenon is harmful for the durability of a fuel cell. It is possible that overall cell performance could be degenerated due to local fatigue from long term operation at higher current density. To ensure the reaction uniformity and enlarge the cell life time, special efforts should be addressed on this problem. A novel configuration of cell channel geometry is investigated in chapter 5. However, the model for these works contains only one single cell and unit channel. In actual situation, the cell system could be made from several unit cells stacked together to obtain a higher voltage output. The phenomenon of non-uniformity of reactant concentration as well as cell reaction could be more

serious in this situation. Therefore, it is necessary to quest this issue in the future by expanding previously developed model into multi-cell stack.

Another recommendation of alleviating previous problem would be focused on a new reactant delivery system that has several layered channels stacked together in channel height direction with a common inlet port and different lengths. The lowest channel has the shortest length for the reactant delivery. In such a way, only limited amount of reactant can participate the cell reaction of the upper channel region and the remaining high concentration reactant is transported to the downstream region.

With this design, the objective of uniform cell reaction can be achieved by way of adjusting the ratio of sub channel length to the total length as well as the number of sub channels. The prediction of cell performance for these novel designs is feasible from the previous developed model. Only a small modification is required for the implementation of numerical calculation of domain properties and cell polarization curve.

REFERENCES

Barbir, F., PEM Fuel Cells: Theory and Practice, Elsevier Academic Press, San Diego, 2005.

Baschuk, J.J. and Li, X., "Modeling of polymer electrolyte membrane fuel cells with variable degree of water flooding," J. Power Sources, vol. 86, pp. 181-196, 2000.

Bernardi, D.M., "Water-balance calculation for solid-polymer-electrolyte fuel cells," J. Electrochem. Soc., vol. 137, no. 11, pp. 3344-3350, 1990.

Bernardi, D.M. and Verbrugge, M.V., "Mathematical model of a gas diffusion electrode bounded to a polymer electrolyte," AIChE Journal, vol. 37, no. 8, pp. 1151-1163, 1991.

Bernardi, D.M. and Verbrugge, M.V., "A mathematical model of the solid-polymer-electrolyte fuel cell," J. Electrochem. Soc., vol. 139, no. 9, 2477-2491, 1992.

Berning, T., Lu, D.M. and Djilali, N., "Three-dimensional computational analysis of transport phenomena in a PEM fuel cell," J. Power Sources, vol. 106, pp. 284-294, 2002.

Berning, T. and Djilali, N., "Three-dimensional computational analysis of transport phenomena in a PEM fuel cell – a parametric study," J. Power Sources, vol. 124, pp. 440-452, 2003.

CFD-ACE(U) TM User Manual, CFD Research Corp., Huntsville, AL, 2004.

Cussler, E.L. Diffusion Mass Transfer in Fluid System, second ed., Cambridge, 1997.

Djilali, N and Lu, D., "Influence of heat transfer on gas and water transport in fuel cells," Int. J. Therm. Sci., vol. 41, pp. 29-40, 2000.

Dutta, S., Shimpalee, S. and Van Zee, J.V., "Three-dimensional numerical simulation

of straight channel PEM fuel cells,” J. Applied Electrochem., vol. 30, pp. 135-146, 2000.

Dutta, S., Shimpalee, S. and Van Zee, J.V., “ Numerical prediction of mass-exchange between cathode and anode channels in a PEM fuel cell,” Int. J. Heat and Mass Trans., vol. 44 pp. 2029-2042, 2001.

Fuller, T.F. and Neuman, J., “Water and thermal management in solid-polymer-electrolyte fuel cells,” J. Electrochem. Soc., vol. 140, no. 5, pp. 1218-1225, 1993.

Gurau, V., Liu, H.T. and Kakac, S., “Two-dimensional model for proton exchange membrane fuel cells,” AIChE Journal, vol.44, pp.2410-2422, 1998.

Giorgi, L., Antolini, E., Pozio, A. and Passalacqua, E., “Influence of the PTFE content in the diffusion layer of low-Pt loading electrodes for polymer electrolyte fuel cell,” Electrochimica Acta, vol. 43, pp. 3675-3680, 1998.

He, W., Yi, J.S. and Nguyen, T.V., “Two-phase flow model of the cathode PEM fuel cell using interdigitated flow fields,” AIChE Journal, vol. 46, pp. 2053-2064, 2000.

Hum, B. and Li, X., “Two-dimensional analysis of PEM fuel cells,” J. Applied Electrochem., vol. 34, pp. 205-215, 2004.

<http://www.etek-inc.com/home.php>.

Jeng, K.T., Lee, S.F., Tsai, G.F. and Wang, C.H., “Oxygen mass transfer in PEM fuel cell gas diffusion layers,” J. Power Sources, vol. 138, pp. 41-50, 2004.

Jordan, L.R., Shukla, A.K., Behrsing, T., Avery, N.R., Muddle, B.C. and Forsyth, M., “Diffusion layer parameters influencing optimal fuel cell performance,” J. Power Sources, vol. 86, pp. 250-254, 2000.

Ju, H., Meng, H. and Wang, C.Y., “A Single-phase, non-isothermal model for PEM

fuel cells,” *Int. J. Heat and Mass Trans.*, vol. 48, pp. 1303-1315, 2005.

Kulikovsky, A.A., Divisek, J. and Kornyshev, A.A., “Modeling the cathode compartment of PEMFC dead and active reaction zones,” *J. Electrochem. Soc.*, vol. 146, pp. 3981-3991, 1999.

Lee, W.K., Ho, C.H., Van Zee, J.W. and Murthy, M., “The effects of compression and gas diffusion layers on the performance of a PEM fuel cell,” *J. Power Sources*, vol. 84, pp. 45-51, 1999a.

Lee, W.K., Van Zee, J.W., Shimpalee and Dutta, S., “Effect of humidity on PEM fuel cell performance Part 1 – experiments,” 1999 International Mechanical Engineering Congress & Exposition, Nashville, TN, 1999b.

Liu, H.C., Yan, Y.M., Soong, C.Y. and Chen, Falin, “Effects of baffle-blocked flow channel on reactant transport and cell performance of a proton exchange membrane fuel cell,” *J. Power Sources*, vol. 142, pp. 125-133, 2005.

Liu, H.C., Yan, Y.M., Soong, C.Y., Chen, Falin and Chu, H.S., “Reactant gas transport and cell performance of proton exchange membrane fuel cells with tapered flow field design,” *J. Power Sources*, vol. 158, pp.78-87, 2006.

Marr, C. and Li, X., “Composition and performance modeling of catalyst layer in a proton exchange membrane fuel cell,” *J. Power Sources*, vol. 77, pp. 17-27, 1999.

Mazumder, S. and Cole, J.S., “Rigorous 3-D mathematical modeling of PEM fuel cells I. Model prediction without liquid water transport,” *J. Electrochem. Soc.*, vol. 150, pp. A1503-A1509, 2003.

Meng. H. and Wang. Chao-Yang, “Electron Transport in PEFCs,” *J. Electrochem. Soc.*, vol 151, pp. A358-A367, 2004.

Natarajan, D. and Nguyen, T.V., “ A two-dimensional two-phase multicomponent transient model for the cathode of a proton exchange membrane fuel cell using

conventional gas distributors,” J. Electrochem. Soc., vol. 148, pp. A1342-A1335, 2001.

Nguyen, T. and White, R.E., “A water and heat management model for proton-exchange-membrane fuel cells,” J. Electrochem. Soc., vol. 140, no. 8, pp. 2178-2186, 1993.

Nguyen, P.T., Berning, T. and Djilali, N., “Computational model of a PEM fuel cell with serpentine gas flow channels,” J. Power Sources, vol. 130, pp. 149-157, 2004.

Parthasarathy, A., Srinivasan, S. and Appleby, A.J., “Temperature dependence of the electro kinetics of oxygen reduction at the platinum/nafion interface- a microelectrode investigation,” J. Electrochem. Soc., vol. 139, pp. 2530-2537, 1992.

Patankar, S.V., Numerical Heat Transfer and Fluid Flow, Hemisphere, New York, 1980.

Rowe, A. and Li, X., “Mathematical modeling of proton exchange membrane fuel cells,” J. Power Sources, vol. 102, pp. 82-96, 2001.

Sammes, N. M., Fuel Cell technology: reaching towards commercialization, Springer-Verlag London Limited, 2006.

Simpalee, S. and Dutta, S., “Numerical prediction of temperature distribution in PEM fuel cells,” Numerical Heat Transfer, Part A, vol. 38, pp.111-128, 2000.

Sivertsen, B.R. and Djilali, N., “CFD-based modeling of proton exchange membrane fuel cells,” J. Power Sources, vol. 141, pp. 65-78, 2005.

Soong, C.Y., Yan, Y.M., Tseng, C.Y., Liu, H.C., Chen, Falin and Chu, H.S., “Analysis of reactant gas transport in a PEM fuel cell with partially blocked flow channels, “ J. Power Sources, vol. 143, pp. 36-47, 2005.

Spiegel, R.J., Gilchrist, T. and House, D.E.,” Fuel cell bus operation at high altitude,”

Proc. Instn Mech. Engrs Part A: J. Power and Energy, vol. 213, pp. 57-68, 1999.

Springer, T.E., Zawodzinski, T.A. and Gottesfeld, S., "Polymer electrolyte fuel cell model," J. Electrochem. Soc., vol. 138, no.8, pp. 2334-2342, 1991.

Sun, W., Peppley, B.A. and Karan, K., "Modeling the Influence of GDL and flow-field plate parameters on the reaction distribution in the PEMFC cathode catalyst layer," J. Power Sources, vol. 144, pp. 42-53, 2005a.

Sun, W., Peppley, B.A. and Karan, K., "An improved two-dimensional agglomerate cathode model to study the influence of catalyst layer structural parameters," Electrochimica Acta, vol. 50, pp. 3359-3374, 2005b.

Um, S., Wang, C.Y. and Chen, K.S., "Computational fluid dynamic modeling of proton exchange membrane fuel cells," J. Electrochem. Soc., vol. 147, pp. 4485-4493, 2000.

Um, S. and Wang, C.Y., "Three-dimensional analysis of transport and electrochemical reactions in polymer electrolyte fuel cells," J. Power Sources, vol. 125, pp. 40-51, 2004.

Wang, C.Y. and Beckermann, C., "A two-phase mixture model of liquid-gas flow and heat transfer in capillary porous media – I. formulation," Int. J. Heat Mass Transfer, vol. 36, pp. 2747-2758, 1993.

Wang, C.Y. and Cheng, P., Advance in heat transfer, Academic Press, San Diego, 1997.

Wang, Z.H., Wang, C.Y. and Chen, K.S., "Two-phase flow and transport in the air cathode of proton exchange membrane fuel cells," J. Power Sources, vol. 94, pp. 40-50, 2001.

Wang, L., Husar, A., Zhou, T. and Liu, H., "A parametric study of PEM fuel cell performances," Int. J. Hydro. Energy, vol. 28, pp. 1263-1272, 2003.

Wang, Y., Wang, C.Y., “A Nonisothermal, two-phase model for polymer electrolyte fuel cells,” *J. Electrochem. Soc.*, vol.153, pp.1193-1200, 2006.

Wangard, W., III, Dandy, D.S. and Miller, B.J., A “Numerical stable method for integration of the multicomponent species diffusion equations,” *J. Comp. Phys.* vol. 174, pp.460-472, 2001.

Weng, F.B., Su, A., Jung, G.B., Chiu, Y.C. and Chan, S.H., “Modeling the Influence of GDL and flow-field plate parameters on the reaction distribution in the PEMFC cathode catalyst layer,” *J. Power Sources*, vol. 145, pp. 546-554, 2005.

West, A.C. and Fuller, T.F., “Influence of rib spacing in PEM electrode assemblies,” *J. Appl. Electrochim.*, vol. 26, pp. 557-565, 1996.

Yan, W.M., Soong, C.Y., Chen, Falin, Chu, H.S., “Effects of flow distributor geometry and diffusion layer porosity on reactant gas transport and performance of proton exchange membrane fuel cells,” *J. Power Sources*, vol. 124, pp.27-39, 2004.

Yan, W.M., Soong, C.Y., Chen, Falin, Chu, H.S., “Transient behaviors of reactant transport and performance of PEM fuel cells,” *J. Power Sources*, vol. 143, pp.48-56, 2005.

Yi, J.S. and Nguyen, T.V., “An along-the-channel model for proton exchange membrane fuel cells,” *J. Electrochem. Soc.*, vol. 145, no. 4, pp. 1149-1159, 1998.

You, L. and Liu, H.T., “A two-phase flow and transport model for the cathode of PEM fuel cell,” *Int. J. Heat Mass Transfer*, vol. 45, pp. 2277-2287, 2002.

APPENDIX A. Expansion Form of Energy Equation

$$\begin{aligned}
 & \frac{\partial(\boldsymbol{\varepsilon}^{\text{eff}} \rho \mathbf{h} \mathbf{u}_x)}{\partial x} + \frac{\partial(\boldsymbol{\varepsilon}^{\text{eff}} \rho \mathbf{h} \mathbf{u}_y)}{\partial y} + \frac{\partial(\boldsymbol{\varepsilon}^{\text{eff}} \rho \mathbf{h} \mathbf{u}_z)}{\partial z} \\
 &= \frac{\partial}{\partial x} \left(\boldsymbol{\kappa}^{\text{eff}} \frac{\partial T}{\partial x} \right) + \frac{\partial}{\partial y} \left(\boldsymbol{\kappa}^{\text{eff}} \frac{\partial T}{\partial y} \right) + \frac{\partial}{\partial z} \left(\boldsymbol{\kappa}^{\text{eff}} \frac{\partial T}{\partial z} \right) \\
 &+ \frac{\partial}{\partial x} \left(\sum_{\alpha=1}^n \sum_{\beta=1}^{n-1} \rho D_{\alpha\beta}^{\text{eff}} \frac{\partial w_{\beta}}{\partial x} \mathbf{h}_{\beta} \right) + \frac{\partial}{\partial y} \left(\sum_{\alpha=1}^n \sum_{\beta=1}^{n-1} \rho D_{\alpha\beta}^{\text{eff}} \frac{\partial w_{\beta}}{\partial y} \mathbf{h}_{\beta} \right) + \frac{\partial}{\partial z} \left(\sum_{\alpha=1}^n \sum_{\beta=1}^{n-1} \rho D_{\alpha\beta}^{\text{eff}} \frac{\partial w_{\beta}}{\partial z} \mathbf{h}_{\beta} \right) \\
 &+ \frac{\partial(\boldsymbol{\varepsilon}^{\text{eff}} \mathbf{u}_x \tau_{xx})}{\partial x} + \frac{\partial(\boldsymbol{\varepsilon}^{\text{eff}} \mathbf{u}_x \tau_{xy})}{\partial y} + \frac{\partial(\boldsymbol{\varepsilon}^{\text{eff}} \mathbf{u}_x \tau_{xz})}{\partial z} + \frac{\partial(\boldsymbol{\varepsilon}^{\text{eff}} \mathbf{u}_y \tau_{xy})}{\partial x} + \frac{\partial(\boldsymbol{\varepsilon}^{\text{eff}} \mathbf{u}_y \tau_{yy})}{\partial y} \\
 &+ \frac{\partial(\boldsymbol{\varepsilon}^{\text{eff}} \mathbf{u}_y \tau_{zy})}{\partial z} + \frac{\partial(\boldsymbol{\varepsilon}^{\text{eff}} \mathbf{u}_z \tau_{xz})}{\partial x} + \frac{\partial(\boldsymbol{\varepsilon}^{\text{eff}} \mathbf{u}_z \tau_{yz})}{\partial y} + \frac{\partial(\boldsymbol{\varepsilon}^{\text{eff}} \mathbf{u}_z \tau_{zz})}{\partial z} + \frac{i_x^2 + i_y^2 + i_z^2}{\sigma} - S_j \eta + S_h
 \end{aligned}$$

